EFFECT OF ELECTROLYTES ON ROOM-TEMPERATURE SODIUM-SULFUR BATTERY PERFORMANCE

by

Daniel Reed

A Thesis

Submitted to the Faculty of Purdue University

In Partial Fulfillment of the Requirements for the degree of

Master of Science in Mechanical Engineering

School of Mechanical Engineering

West Lafayette, Indiana

May 2022

THE PURDUE UNIVERSITY GRADUATE SCHOOL
STATEMENT OF COMMITTEE APPROVAL

Dr. Partha P. Mukherjee, Chair

School of Mechanical Engineering

Dr. Corey Love

United States Naval Research Laboratory

Dr. Jason Ostanek

School of Engineering Technology

Approved by:

Dr. Nicole L. Key

Dedicated to Mom and Dad

ACKNOWLEDGMENTS

TABLE OF CONTENTS

LIST OF TABLES

LIST OF FIGURES

ABSTRACT

Room-temperature sodium-sulfur (RT Na-S) batteries are an emergent new technology that are highly attractive due to their low raw materials cost and large theoretical specific energy. However, many fundamental problems still plague RT Na-S batteries that prevent their progression from the research and development phase to the commercial phase. Sulfur and its final discharge product are insulators, and intermediate polysulfide discharge products are soluble in commonly used liquid electrolytes. As a result, RT Na-S cells exhibit large capacity defects, low coulombic efficiencies, and rapid capacity fading. Additionally, the reactive sodium metal anode can form dendrites during cycling, which reduces capacity and shortens cell life. One way to combat these issues is the judicious selection of electrolyte components. In this study, the effects of monoglyme (G1), diglyme (G2), and tetraglyme (G4) glyme ether electrolyte solvents on RT Na-S cell performance are investigated. Galvanostatic cycling of Na/Na symmetric coin cells reveals that the G2 solvent enable stable cycling at low overpotentials over a wide range of current densities. In contrast, the G1-based cells show evidence of dendritic plating, and G4-based cells are not suitable for use at high current densities. Electrochemical impedance spectroscopy during cycling confirms that the G2 solvent facilitates the formation of a strong, stable SEI on the Na electrode surface. Results from galvanostatic cycling of RT Na-S full coin cells demonstrates that G1-based cells deliver the highest initial specific discharge capacities among the three cell types, but G4-based cells are the most reversible. Infinite charging, the indefinite accrual of charge capacity at the high charge voltage plateau, affects all cell types at different cycle numbers and to different extents. This behavior is linked to the strength of the polysulfide shuttle during charge. Optical microscopy experiments show that G2 and G4 facilitate the formation of the $S_3^{\bullet-}$ sulfur radical, which reduces capacity. G1 minimizes the radical formation and thus delivers higher initial specific discharge capacity. In order to fully optimize the electrolyte for RT Na-S cells, future work should study glyme solvent blends, additives, and concentrated salts.

1. INTRODUCTION

1.1 Energy Storage Systems

Since the Industrial Revolution began in the mid-eighteenth century, fossil fuel combustion has increased the concentration of CO_2 in the atmosphere by 47% [1]. CO_2 and other greenhouse gases like methane trap radiant heat in the atmosphere, warming the Earth. With no corrective action, the global average surface temperature could increase between 3.7°C to 4.8°C by the end of the 21st century compared to that prior to the Industrial Revolution [2]. Climate change towards a warmer planet will cause sea levels to rise and increase the frequency and intensity of droughts, heat waves, and hurricanes. In order to reverse or partially reverse the effects of climate change, society must re-examine the ways in which it consumes and produces energy, and take every available action to utilize renewable resources.

Despite the severe consequences of a warmer planet, humans consume fossil fuels for the vast majority of their energy needs. In 2018, 85% of the 599 quadrillion BTU of energy consumed globally came from coal, natural gas, and petroleum [3]. In that same year, the United States consumed 101 quadrillion BTU by itself, with 82% coming from fossil fuels and only 10% coming from renewable, non-nuclear sources. In 2020, 79% of the 93 quadrillion BTU consumed by the United States came from fossil fuels, while renewable energy (non-nuclear) consumption increased to 12%, an all-time high [4]. Of the renewable energy consumption in the United States in 2020, 37% came from solar and wind. This data shows that while renewable energy made gains in this short time span, there is still an opportunity for renewables to supplant traditional fossil fuels in overall energy consumption. One way this can be achieved is through pairing intermittent renewable energy sources like wind and solar with stationary, grid-scale electrical energy storage systems (EES). Wind speed and solar irradiance at a given point are not necessarily reliable or constant, so an energy storage method like batteries must be used in conjunction with these primary sources to deliver electricity during periods of high demand or low wind speed/solar irradiance. Another way that fossil fuels can be supplanted by renewable sources is by widespread adoption of electric vehicles (EVs) or hybrid electric vehicles (HEVs) that use batteries as an energy source. In 2020, 35% of the energy consumed in the U.S. was used for transportation, and 90% of that

energy came from petroleum [4]. Furthermore, 29% of the greenhouse gas emissions in the U.S. were from the transportation sector [5]. Switching to EVs and HEVs could mitigate fossil fuel use worldwide, but only if the electricity used by EVs comes from clean sources [6]. In 2008, Armand and Tarascon found that with a lithium-ion (Li-ion) battery carbon footprint of 70 kg CO_2 kWh^{-1}, the environmental benefits of using electric vehicles powered by Li-ion batteries only begin to pay off after 120 discharge-charge cycles [7]. This analysis assumed that the electricity used to charge the vehicles came from a coal-powered power plant with an efficiency of 35%. It is crucial to pair EV use with less polluting electricity sources like renewables or natural gas in order to maximize their benefits in the short term as well as the long term. In 2019, Emilsson and Dahllöf of the IVL Swedish Environmental Research Institute conducted a life-cycle analysis of greenhouse gas emissions from Li-ion battery production and found that raw materials acquisition, cell assembly, and pack assembly produces 61-106 kg CO_2 kWh^{-1}, not including recycling emissions [8]. Although these values appear to be the same as or worse than the value used by Armand and Tarascon, this range is a drastic improvement from the one determined by the 2017 IVL Swedish Environmental Research Institute report of 135-185 kg CO_2 kWh^{-1}, not including recycling emissions [9]. Thus, renewably sourced electricity must be adopted and paired with electrical energy storage devices, such as batteries, to limit harmful greenhouse gas emissions from the manufacturing process of the battery itself.

Supplementing renewable primary sources or supplanting fossil fuel use in transportation for climate purposes are not the only uses for energy storage systems. Batteries, and in particular, Li-ion batteries, were crucial in enabling portable consumer electronics like cell phones and laptop computers to become ubiquitous. Additionally, energy storage systems are employed in mobile aerospace and defense applications, like unmanned aerial vehicles (UAVs) or unmanned undersea vehicles (UUVs). Grid storage, electric vehicles, consumer electronics, and mobile defense craft all require energy storage systems, and batteries are widely used in all of these applications.

1.2 Battery Electrochemical Energy Storage

With energy densities greater than those of supercapacitors and power densities greater than those of fuel cells, batteries have the performance characteristics to be used in a wide array of applications [10]. A battery is a closed system device that is comprised of one or more individual

electrochemical cells. In this work, the terms "battery" and "cell" are used interchangeably. Batteries release electrical energy through redox reactions that occur at the cell electrodes. Batteries in which the redox reactions are irreversible and cannot be recharged after the initial discharge are known as primary batteries. Batteries in which the redox reactions are reversible and can be recharged for further use are known as secondary batteries. In general, batteries consist of a cathode where the reduction reaction takes place during discharge, an anode where the oxidation reaction takes place during discharge, an ion-shuttling electrolyte, and a separator that is electrically insulating but ionically permeable.

1.2.1 Lithium-Ion Batteries

Beginning in the 1990s, Li-ion batteries have dominated as the energy storage method for mobile electronics and vehicles. The Li-ion battery was first commercialized by Sony in 1991 and again by Asahi Kasei/Toshiba in 1992 after research and development efforts that date back to the 1970s [11]. This new technology boasted a specific energy and an energy density that are twice as high as the existing Ni-Cd and Ni-MH cells [11] [12]. Today, commercial Li-ion cells have attained specific energies and energy densities of as high as 256 Wh kg^{-1} and 697 Wh L^{-1}, respectively [13]. Typically, Li-ion cells have specific energies between 150 and 200 Wh kg^{-1} [14]. Other advantages of Li-ion cells include a nominal voltage of around 4 V, which enables them to power more complex devices with higher power demands, a long cycle life, and a low self-discharge rate [11] [12]. Prior to the development of the Li-ion battery, secondary batteries with layered transition metal cathodes like Li_xCoO_2 or Li_xTiS_2 and Li metal anodes showed promise with large theoretical energy densities, but they were limited by an unstable solid electrolyte interphase (SEI) that forms spontaneously in organic electrolytes and causes irreversible capacity loss and low coulombic efficiency during cycling [15] [16]. Furthermore, Li metal anodes in organic electrolytes have a tendency to produce a needle-like or mossy dendrite structure on the electrode surface during cycling, that can also pierce the cell separator, electrically short the cell, and potentially lead to a fire or explosion due to thermal runaway [17] [18] [19]. However, Li-ion cells circumvent this issue in normal operation through an intercalation reaction mechanism. Instead of plating or stripping Li ions from a metal surface, Li-ion cells shuttle Li ions inserted, or intercalated, between transition metal oxide layers in the cathode and graphite layers in the anode during cell operation [20] [21].

Today, Li-ion batteries are the energy storage device of choice for smart phones, compact electric vehicles, and high performance electric sedans [22] [23] [24]. Improvements in technology have also decreased the price of Li-ion cells. Between 2010 and 2020, pack-level costs for lithium-ion batteries fell from between \$500-700/kWh to \$143/kWh [25] [26]. Falling Li-ion costs have enabled utility companies to use the technology for grid-scale electrical energy storage projects across the world. The Hornsdale Power Reserve in South Australia utilizes Li-ion battery units from Tesla and began grid support operation in 2017 with 100MW/129MWh power/energy capacity [27]. In 2020, this facility added 50MW and 64.5 MWh of power and energy capacity, respectively. In the U.S., 77% of electrochemical energy storage systems for grid support utilize Li-ion batteries, mostly for maintaining grid frequency at 60 Hz [28]. Certainly, Li-ion batteries have ushered in a new era of sustainable technology.

Despite being an integral component of modern technology, Li-ion cells have limitations. Improvements of the power density of Li-ion cells comes at a cost of reduced energy density, and improvements in the capacity of Li-ion cells has stalled in recent years [29]. Although Li-ion cells do not form metallic dendrites on the anode surface during operation under normal conditions, various thermal, electrical, electrochemical, and mechanical conditions will induce thermal runaway in Li-ion cells. High ambient temperatures of 90°C or greater, short circuiting, overcharge past the typical 4.2 V upper cutoff voltage, and puncturing/mechanical abuse will lead to thermal runaway in a Li-ion cell [30] [31]. Additionally, charging at low ambient temperatures or at high rates will cause Li plating and dendrite formation in a Li-ion cell [32]. The safety issues of Li-ion cells have led to a number of high-profile incidents, including fatal airplane crashes.

A limiting factor to the continued growth and development of HEV/EV, grid EESs, and portable electronic technology powered by (Li-ion) batteries is the scarcity of necessary raw materials, notably lithium, nickel, and cobalt. These materials are heavily used in popular Li-ion cathode materials, including LCO, $LiNi_{1-x-y}Mn_xCo_yO_2$ (NMC), and $LiNi_{1-x-y}Co_xAl_yO_2$ (NCA). Li, Ni, and Co are all rare elements in the Earth's crust, with concentrations ranging from just under 100 ppm for Ni to 20 ppm for Li [33]. The consequence of this rarity is that these metals are expensive. For example, the lithium raw material price was \$17000 per ton at the beginning of

2020 [34]. Indeed, the high costs of cathode materials and battery materials in general contribute 49% and 70% of the total cost of a cell, respectively [25]. In addition to being rare and expensive, Li and Co have uneven distributions within the Earth's crust. Most of the world's Li mining occurs in South America, and 60% of the world's Co is produced exclusively in the Democratic Republic of the Congo [33] [35]. Safety issues, stagnant capacities, and raw material scarcity have left opportunities open for new types of battery chemistries to improve upon system cost and specific energy and eventually replace conventional Li-ion batteries.

1.3   Sodium-Sulfur: A Next Generation Battery Chemistry

Cheap and powerful energy storage devices are needed to stop and reverse the effects of human-caused climate change. Sodium-sulfur (Na-S) batteries combine two readily available and low-cost materials into an energy dense package, and they are attractive candidates for next generation batteries that can improve on Li-ion technology. The sulfur cathode provides a high theoretical capacity of 1672 mAh g^{-1} owing to the two electron transfer of the redox reaction and a potential of -0.407 V vs. the standard hydrogen electrode (SHE), and the sodium metal anode provides a theoretical capacity of 1166 mAh g^{-1} and low potential of -2.71 V vs. the SHE [36]. The full cell provides a theoretical capacity of 687 mAh g^{-1} and a specific energy of 1271 Wh kg^{-1} at an average voltage of 1.85 V at room temperature. The lithium-sulfur (Li-S) cell is another type of next generation battery with a high theoretical specific energy that also uses a sulfur cathode, but Li-S cells use metallic Li as the anode. The key strength of Na-S batteries over other systems is the high natural abundance of its constituent active materials. Na is the 6th most abundant element in the earth's crust with a concentration of 25670 ppm, while S also has a high concentration in the earth's crust of 953 ppm [34] [36]. On a cost per unit-energy basis, Na-S cells outperform both Li-ion and Li-S cells. Both Na-S and Li-S batteries are an order of magnitude less expensive than traditional Li-ion batteries, and Na-S has a competitive edge over Li-S in cost ($1.40 kWh^{-1} vs. $9.90 kWh^{-1}) [34]. While a difference in cost of $8.50 kWh^{-1} is not very significant for small batteries, it is significant in large batteries being used for grid support EES, which is why Na-S batteries are desirable over Li-S for this application. For a 195 MWh battery like the one being used by the Hornsdale Power Reserve, one would save $1.66 million by choosing to use Na-S over Li-S. Figure 1.1 gives a graphical representation between the

differences in cost and specific energy between commercially used Li-ion cells and the next generation chemistries of Na-S and Li-S.
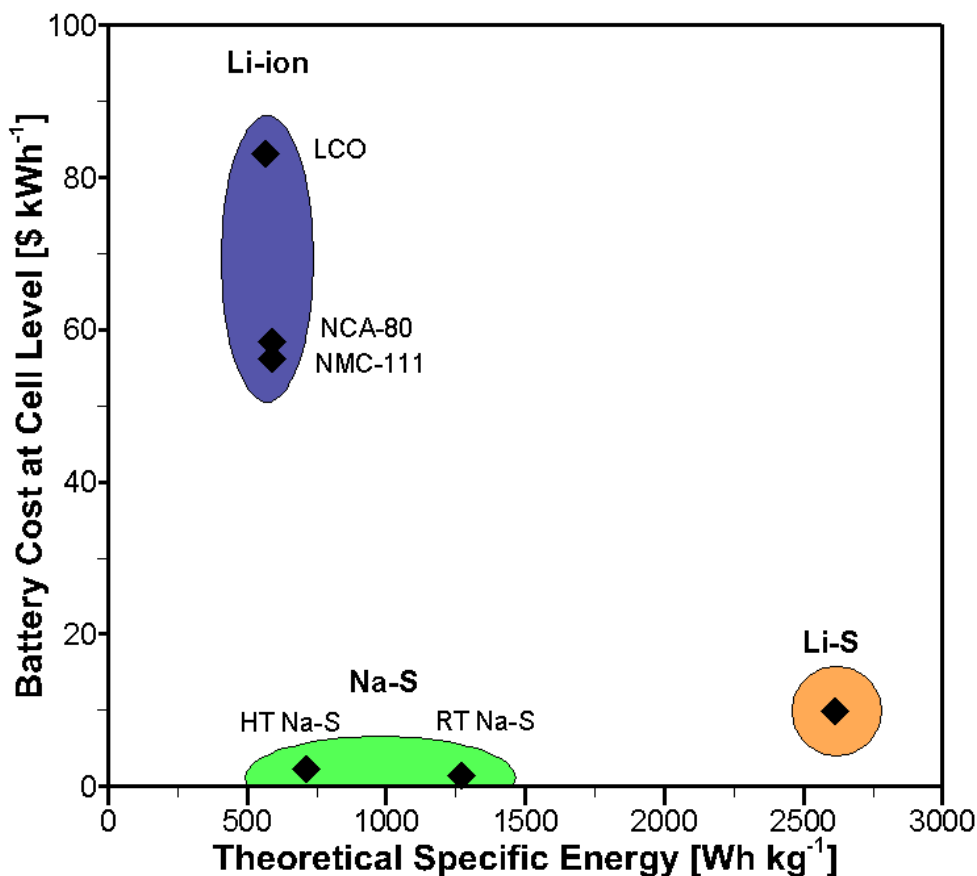
Figure 1.1. Cost and specific energy analysis of three common Li-ion cell types, high-temperature and room-temperature Na-S cells, and Li-S cells. Research and development efforts will enable the reduction in energy cost and an increase in specific energy as current-generation (Li-ion) systems are abandoned in favor of next-generation (Na-S and Li-S, among others) systems. Cost data derived from [34] and [37]. References [38], [37], [39], [40], [41], [42], [43], and [36] were used to calculate theoretical specific energies, which are detailed below.

Li-ion, Li-S, and most other battery chemistries like Ni-MH or Zn-MnO$_2$ are designed to operate around room temperature; however, the only commercially used Na-S batteries are operated in molten liquid form at high temperatures of around 300°C. These high-temperature (HT) Na-S cells were first commercialized in Japan for large scale energy storage in the early 2000s [36]. The ZEBRA battery is also a commercialized HT molten sodium battery, but it uses a metal chloride in the positive electrode instead of sulfur [44]. In contrast, room-temperature (RT) and

intermediate temperature (IT) Na-S batteries are still in the early stages of research and development.

The general operating principles in all Na-S batteries are similar, but there are important differences between HT, IT, and RT Na-S batteries. In RT Na-S cells, solid phase sulfur, conductive carbon, and a binder solution are combined in the cathode. Just as in Li-S batteries, the sulfur in the cathode of RT Na-S batteries needs to be combined with an electronically conductive matrix of carbon in order to supplement the low electric conductivity of solid sulfur and polysulfide discharge products. The mass loading of sulfur in RT Na-S electrodes can be as low as 27%, and sulfur usually accounts for only 50-70% of the total cathode mass [39]. RT Na-S cells are usually assembled in the fully charged state, with sulfur and not sodium sulfide as the active material added to the electrode slurry during fabrication. The anodes in RT Na-S batteries are composed of solid Na metal. The electrolyte in RT Na-S batteries is typically composed of a Na salt in an organic liquid solvent of the ether or carbonate families, but liquid inorganic electrolytes, gel polymer electrolytes, and solid electrolytes are also used. The electrolyte must be carefully chosen to prevent adverse side reactions with the Na anode and form a stable SEI on the anode surface. The separator in a RT Na-S battery must be permeable to Na ions as well as impermeable to electrons. Typically, a glass fiber separator is used, but a solid electrolyte may be used to mitigate the polysulfide shuttle effect. The design and operating characteristics of a typical RT Na-S cell are shown below in Figure 1.2. Li-ion batteries operate through intercalation reactions in which Li ions are shuttled between layers of the electrode active materials, but Na-S batteries operate by a conversion reaction in which the sulfur in the cathode is converted to another state. During discharge, the sulfur in the cathode reduces to sodium sulfide through a series of intermediate reductions to long- and short-chain sodium polysulfides. During charge, sodium sulfide is oxidized back to sulfur. The higher-order polysulfide intermediate compounds are soluble in the battery electrolyte, so they are shown away from the cathode in Figure 1.2. The low-order products Na_2S_3, Na_2S_2, and Na_2S are insoluble in electrolytes and consequently precipitate out of solution [45] [46]. This solubility phenomenon is the cause of one the several fundamental problems preventing widespread adoption of RT Na-S batteries: the polysulfide shuttle effect. Long- and medium-chain polysulfide intermediates can diffuse into the electrolyte and migrate from the cathode to the anode, where they are reduced and corrode the anode surface. The reduction of polysulfide species on the

anode represents a loss in capacity of the battery, which results in rapid capacity fading between cycles. Another fundamental issue with RT Na-S batteries is non-uniform sodium plating/stripping and dendrite formation, which occurs when concentration gradient profiles in the liquid electrolyte becomes uneven and when impurities or roughness are present on the anode surface [47]. As with Li-ion batteries, dendrite formation is a safety concern as well as a source of capacity loss in the RT Na-S cell.
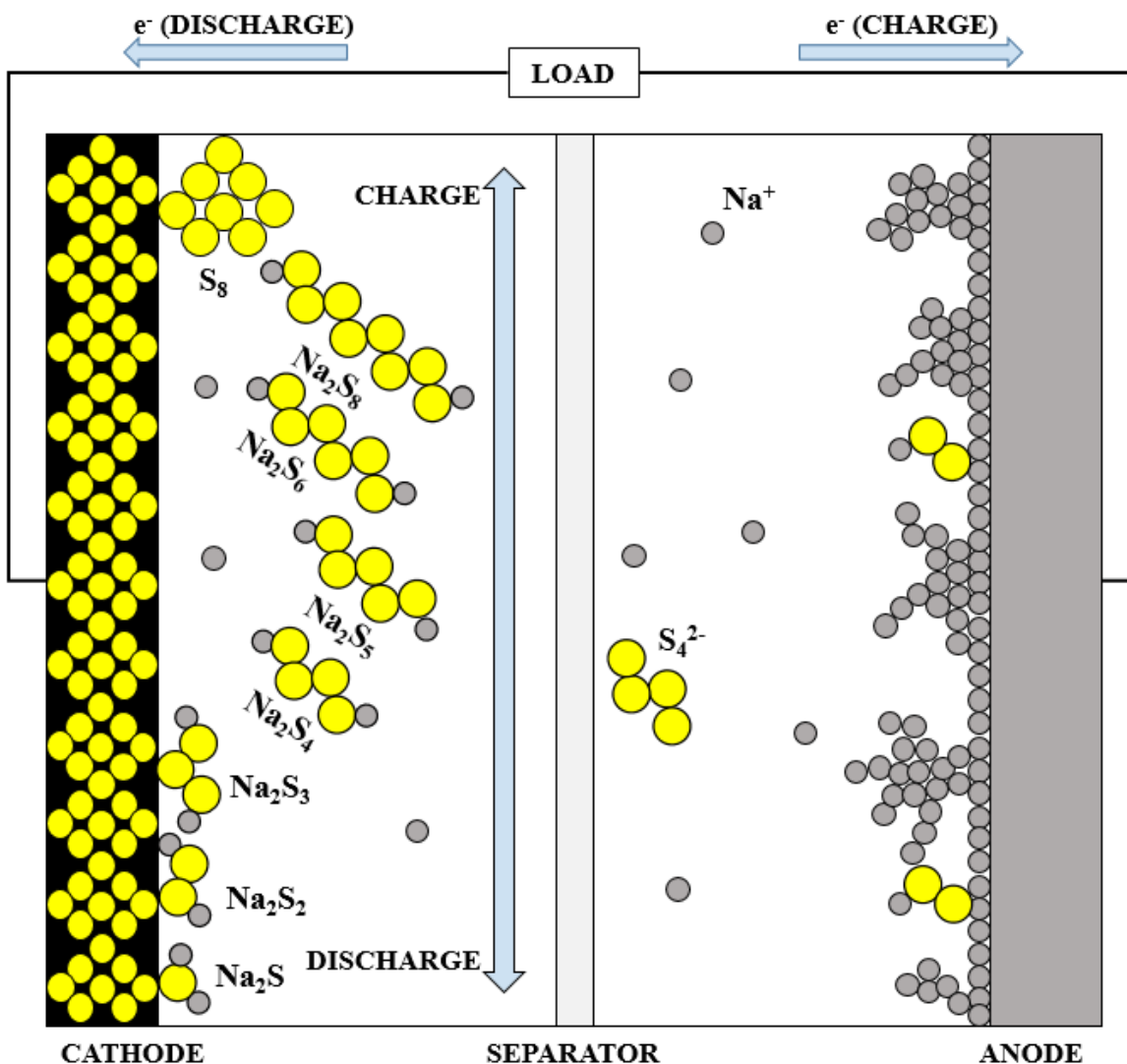
Figure 1.2. Overview of a RT Na-S cell during operation. During discharge, sulfur is reduced into soluble long-chain polysulfides, then insoluble short-chain polysulfides, and finally sodium sulfide. During charge, this process is reversed. The separator is electrically insulating but permeable to Na cations and soluble polysulfide anions. Through the shuttle effect, the soluble polysulfides can be reduced on the surface of the anode, representing a loss of capacity. Plating and stripping of Na in the anode can lead to dendrite formation.

19

While very similar to their Li-S counterparts, there are important differences between Li-S and RT Na-S cells that arise when Li is replaced by Na as the cell anode. Sodium atoms are larger than lithium atoms on both a mass and a volume basis, so sodium-based cells have lower specific energies and energy densities than lithium-based cells. The theoretical specific capacity (q_{th}) in mAh g^{-1} for a given active material or electrochemical reaction is calculated as a function of the number of electrons exchanged per mole of reaction product (n), the Faraday constant (F), and the molecular weight of the reaction product (M_W), as seen in Equation 1.1 [45].

$$q_{th} = \frac{nF}{3.6M_W}$$

(1.1)

Theoretical specific energy for a given cell chemistry can be calculated by multiplying the theoretical specific capacity by the standard full cell potential of the overall cell reaction. This result can be multiplied by the density of the final reaction product in g L^{-1} to obtain the theoretical energy density of the cell chemistry. Using this method, the theoretical specific capacity, theoretical specific energy, and theoretical energy density for the Li-S and Na-S cell chemistries are shown below in Table 1.1.

Table 1.1. Comparison of theoretical specific capacities, specific energies, and energy densities of the Li-ion (three different cathode materials), Na-S (RT and HT), and Li-S battery chemistries. Specific capacity values shown here were calculated from Equation 1.1 for the full cell reaction in each case. Full cell potential values were obtained from [38], [37], and [39], and material densities were obtained from [42], [41], [37], [43], [40], and [36]. The active material density used for the calculation of the Li-ion theoretical energy densities were the average densities of the specific cathode material and graphite.

Cell Type	Theoretical Specific Capacity [mAh g^{-1}]	Standard Full Cell Potential [V]	Theoretical Specific Energy [Wh kg^{-1}]	Theoretical Energy Density [Wh L^{-1}]
Li-ion (LCO)	158	3.6	569	2001
Li-ion (NMC-111)	159	3.7	589	2057
Li-ion (NCA-80)	159	3.7	590	2067
RT Na-S	687	1.85	1271	2364
HT Na-S	377	1.9	716	1339
Li-S	1168	2.24	2616	4343

Table 1.1 shows that replacing the lithium metal anode with sodium metal across from a sulfur cathode causes a 51% reduction in the theoretical specific energy of the cell. This is substantial, but the theoretical specific energy of the Na-S cell is still 2-3 times larger than that of the Li-ion cell chemistry. In addition to larger atom size and lower charge density, replacing lithium with sodium can create safety issues due to the lower melting point of sodium ($T_M = 98°C$ for Na vs. $T_M = 181°C$ for Li), make processing and manufacturing more difficult due to sodium being a softer and stickier metal than lithium, slow cell kinetics due to thermodynamically stable solid sodium polysulfide phases and larger ion size, and lead to faster cell degradation due to the increased volume expansion during cycling [39] [48]. It has also been reported that the polysulfide

shuttle is more detrimental to the performance of RT Na-S batteries than it is to that of Li-S batteries due to greater solubility of intermediate polysulfide species [48] [49]. The Na anode is more likely to grow dendrites and forms a more unstable SEI layer than the Li anode [48]. Not all of the consequences are negative. Sodium is cheaper than lithium ($0.149 kg^{-1} for Na vs. $17 kg^{-1} for Li) and more abundant than lithium (25670 ppm in Earth's crust for Na vs. 22 ppm in Earth's crust for Li) [34]. Unlike lithium, sodium does not form alloys with aluminum which enables it to be used as the anode current collector material in Na-S cells whereas more expensive copper current collectors must be used in lithium-based cells [39]. Additionally, solid electrolytes are commercially available for sodium-based cells but not for lithium-based cells, which makes it easier to test Na-S batteries in a solid state configuration.

The HT Na-S system operates at 300-350°C; therefore, the sulfur in the cathode (T_M = 118°C) and the sodium in the anode (T_M = 98°C) are in liquid phase [34]. In the cathode, a porous carbon material is used as the current collector to supplement the low electronic conductivity of sulfur, similar to the carbon in the cathode of a RT Na-S cell. A beta-alumina solid electrolyte is used to conduct sodium ions to and from the cathode. Since Na_2S_2 forms as a solid at the operating temperatures of HT Na-S batteries and is an electronically insulating material, the final discharge product of HT Na-S cells is Na_2S_3 [36]. Thus, HT Na-S cells achieve lower specific energies than their RT counterparts. Additionally, HT Na-S cells are prone to severe safety issues due to their operating temperatures, including corrosion of active materials, flammability of sulfur, and the potential release of toxic sulfur dioxide gas [36] [34]. In IT Na-S cells, the operating temperature is 120-300°C. At these temperatures, the sodium anode is also in a molten liquid state, but the active material in the cathode is present in both the solid and the molten liquid states. In the IT configuration, a beta-alumina solid electrolyte can also be used. While the IT configuration exhibits improvements in cost and safety over HT Na-S cells, sulfur utilization in the cathode is suboptimal. This problems stems from the direct relationship between conductivity and solubility of sodium polysulfides with temperature, higher internal resistance from lower beta-alumina solid electrolyte Na wettability, and limited specific energy due to the final polysulfide discharge product [36] [34]. This work will focus on the RT configuration over the IT and HT counterparts. In Chapter 1.3.1, a history of all Na-S batteries is given, with a look into the rapid emergence of RT Na-S in the literature within the past two decades. In Chapter 1.3.2, the complex redox

mechanism of RT Na-S batteries is introduced. In Chapter 1.3.3, the obstacles to the widespread use of RT Na-S batteries are discussed in detail. In Chapter 1.3.4 the use of electrolytes to improve RT Na-S battery performance is briefly introduced. In Chapter 2, electrolytes for RT Na-S batteries and how they influence cell behavior and performance are discussed.

1.3.1 History of Sodium-Sulfur Batteries

The genesis of Na-S batteries dates back to the mid-1960s, when J.T. Kummer and N. Weber of the Ford Motor Company filed for a patent for a HT Na-S cell with molten electrodes and a beta-alumina solid electrolyte for electric vehicle applications [50] [51]. In the late 1980s and early 1990s, NASA was interested in HT Na-S cells for satellite and spaceflight applications [52] [53]. However, the most groundbreaking work with HT Na-S occurred in Japan in 2003, when NGK Insulators, Ltd. and the Tokyo Electric Power Company (TEPCO) began commercial production of HT Na-S cells for grid-scale load leveling applications following development efforts dating to the mid-1980s [54] [55]. Since then, there have been 174 HT Na-S energy storage installations built in six different countries, with a power capability of 305,000 kW [56]. In 2011, the safety concerns of HT Na-S batteries were realized when the HT Na-S battery at the Tsukuba Plant in Joso City, Ibaraki Prefecture, Japan, exploded and caught fire [34].

In 2006, Cheol-Wan Park and colleagues reported the first RT Na-S battery, in the hopes of resolving the safety issues of HT Na-S batteries by reducing the operating temperature [57]. This cell had a solid Na metal anode, a solid composite sulfur cathode, and a polyvinylidene-fluoride-hexafluoropropene (PVDF) gel polymer electrolyte, and it exhibited a first discharge specific capacity of 489 mAh g^{-1} with rapid capacity fading on subsequent cycles. Since this seminal work, the number of academic proceedings which relate to RT Na-S batteries has grown exponentially between 2006 and 2021. This trend is shown below in Figure 1.3.
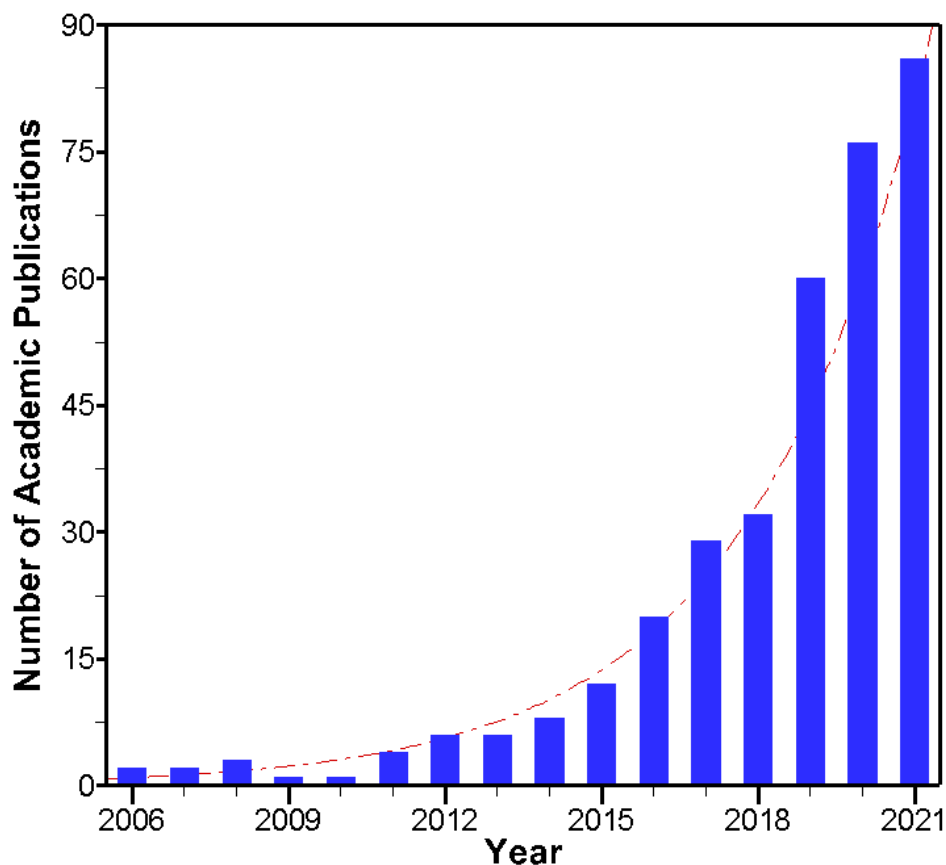
Figure 1.3. Number of journal articles, conference abstracts, theses/dissertations, and book chapters relating to RT Na-S batteries that appeared in the literature each year between 2006 and 2021. The search phrase used was "room temperature sodium sulfur" on Google Scholar.

Research on RT Na-S especially began to increase in the mid-2010s, after the Tsukuba Plant fire incident. Despite the rapid growth of this field, more research into the fundamental understanding of RT Na-S batteries is needed so that their advantages in specific energy and cost can be realized on a practical level.

1.3.2   Room-Temperature Sodium-Sulfur Electrochemistry

In RT Na-S cells, elemental sulfur in the form of cyclo-S_8 in the cathode is reduced by the sodium metal anode during discharge to form the final discharge product of sodium sulfide (Na_2S).

Typically, RT Na-S cells are assembled fully charged, with cyclo-S_8 in the electrode rather than the Na_2S discharge product. The half reaction at the cathode is:

$$\frac{1}{8}S_{8(s)} + 2e^- \rightleftharpoons S^{2-} \tag{1.2}$$

During charge, the S^{2-} anion is oxidized to form sulfur. At the anode, sodium metal is oxidized during discharge to form one sodium cation and one electron per sodium atom. The sodium cations diffuse the separator to the cathode in the electrolyte, and the electrons flow through an external circuit to the cathode. The half reaction at the anode is:

$$Na_{(s)} \rightleftharpoons Na^+ + e^- \tag{1.3}$$

During charge, the sodium ions in Na_2S are reduced to form metallic sodium. The full cell reaction is:

$$\frac{1}{8}S_{8(s)} + 2Na_{(s)} \rightleftharpoons Na_2S_{(s)} \tag{1.4}$$

This is the ideal electrochemical reaction in RT Na-S cells. However, unlike Li-ion cells in which the redox reactions occur in one direct step, the redox reaction in Equation 1.4 occurs indirectly through a series of intermediate steps. The exact reaction mechanism of the reduction of sulfur to sodium sulfide during discharge and the oxidation of sodium sulfide to sulfur during charge is complex, and it is still an active research area. Additionally, the redox reaction mechanism of the sulfur cathode is strongly dependent on the electrolyte used in the cell, so it is difficult to generalize the redox reactions across all electrolyte classes [39] [58] [59]. Broadly, reduction begins by the breaking of the cyclo-S_8 ring to form soluble long-chain sodium polysulfides of the form Na_2S_x $\left(4 \leq x \leq 8\right)$, with the chain length decreasing as reduction continues [45] [46]. Thermodynamically, this step should occur at 2.03 V [60]. In the next step, the long-chain polysulfides are further reduced to short-chain polysulfides of the form Na_2S_x $\left(1 \leq x < 4\right)$, with x = 1 being the final discharge product, sodium sulfide [45] [46]. According to thermodynamics, the reduction of Na_2S_2 to Na_2S should occur at 1.68 V [60]. During charge, this process is reversed. The redox reaction mechanisms of the RT Na-S have been discussed often in the literature, and they will be discussed in more detail in Chapter 2.2.3.

1.3.3 Degradation Mechanisms of Room Temperature Sodium-Sulfur Batteries

There are four fundamental issues inherent within RT Na-S batteries that negatively affect overall performance [61]:

1) Low Electronic Conductivity of Sulfur

2) Volume Expansion

3) Polysulfide Solubility

4) Sodium Anode Instability

As a result of these four issues, RT Na-S cells exhibit low initial discharge capacity that is only a fraction of the theoretical value, rapid capacity fading after the first cycle, and low coulombic efficiency. These issues can be categorized by their source, as issues 1-3 originate at the S cathode, and issue 4 originates from the anode properties.

Of RT Na-S cells reported in the literature, the S content of the cathode (excluding the current collector) is typically between 30 and 70 wt%, which can be seen in Figure 2.3 of Chapter 2.2.5. In contrast, the active material content in Li-ion cathodes is rarely lower than 95 wt% [39]. This difference in active material content is attributed to the fact that sulfur and short-chain sodium polysulfide discharge products like Na_2S are electrical insulators (issue 1). Specifically, the electrical conductivity of sulfur is 10^{-15} S m^{-1} [62]. For comparison, the electrical conductivity of graphite, a conductor, is 10^5 S m^{-1} [63]. As a consequence, RT Na-S cathodes require a redox-inactive, conductive support material that lowers the overall specific energy and energy density of the cell. The conductive support material of choice is some form of carbon. Sulfur's electrically insulating nature and low reactivity with sodium harms cell performance by preventing electrons from quickly reaching the sulfur particles to complete the redox reactions and results in low sulfur utilization [64]. Moreover, insulating short-chain sodium polysulfides can encapsulate S particles during cell operation and prevent full utilization of sulfur even further [46]. In fact, slow redox kinetics of these insulating short-chain sodium polysulfide species have been shown to be a cause

of capacity fading during cycling [65]. Volume expansion (issue 2) in the sulfur cathode during discharge is another key degradation mechanism of RT Na-S batteries. The conversion of S into Na_2S during discharge results in a volume increase of 170% to 260% due to differences in molar volume and density, respectively [39] [61]. A volume increase of this magnitude during discharge and subsequent contraction during charge puts a great deal of stress on the cathode. Over time, the cathode material will crack and pulverize, which leads to loss of cycle life [66]. Polysulfide solubility and the associated polysulfide shuttle (issue 3) have been discussed earlier and are perhaps the most notorious of the degradation mechanisms associated with RT Na-S and Li-S batteries. Since the long-chain sodium polysulfides can dissolve into the electrolyte, they shuttle in the electrolyte through the separator from the cathode to the anode due to both concentration gradients and potential differences in the electrolyte [67]. Since this phenomenon occurs without interactions from external electrons, it is a chemical process. Once at the anode, the polysulfide species get reduced by the Na metal and corrode the anode, which represents irreversible capacity loss. The polysulfide shuttle affects the cell during electrochemical operation, and since it is a chemical process, causes a high self-discharge rate at rest [68].

At the anode, the high reactivity of Na in the liquid organic electrolytes facilitates the spontaneous formation of a SEI layer on the anode surface. The SEI is composed of different phases arranged together, and its composition varies along its thickness [69]. The SEI must be ionically conductive and electronically insulating like a separator or solid electrolyte, and it must also be strong and flexible to accommodate Na plating and stripping during electrochemical operation. When a weak and brittle SEI forms on the anode, it can crack from the stresses applied during plating [70]. In addition to exposing fresh Na metal to the electrolyte for further decomposition, cracks and other surface protrusions or roughness can concentration electric field lines and promote inhomogeneous Na deposition [48]. When this happens, dendrites will begin to grow from the anode. Just like in Li metal cells, Na dendrites can present a safety concern if they grow large enough to pierce the separator and induce thermal runaway. Moreover, Na stripping at the anode during discharge can separate dendrite structures from the bulk of the anode and render this dead sodium electrochemically inactive, which results in capacity fading. Thus, the instability of the Na anode (issue 4) is both a degradation mechanism and a safety risk.

A variety of strategies have emerged to combat these four issues. Carboxyl binders have been studied in RT Na-S cathodes to both hold together the cathode structure during volume change and control polysulfide dissolution [66]. In order to increase the electrical conductivity of the traditional S-C composite cathode, researchers have added selenium as an active material [71], used metal sulfides like iron sulfide (pyrite) or titanium sulfide as the active materials [72] [73], and used carbon nanotubes as the conductive matrix [59]. Porous carbon architectures have been used to both increase cathode conductivity and prevent polysulfide dissolution. These efforts include microporous carbon spheres [74], polyhedral microporous carbon [48], and carbon nanotube/microporous carbon cables [64]. Researchers have also covalently bonded sulfur to carbon atoms in a polymer framework [75]. Recently, electrocatalysis using transition metals like cobalt has emerged as way to speed up the sulfur redox reactions [76]. The polysulfide shuttle has been mitigated through the use of a carbon interlayer in between the cathode and separator [45] and through the replacement of a traditional separator with a solid electrolyte disk [60]. While the aforementioned strategies focus on developing advanced cathode architectures or adding/modifying the separator structure, carefully selecting the electrolyte composition is an effective strategy to mitigate the polysulfide shuttle and ensure anode stability.

1.3.4   Electrolyte Design for Improved RT Na-S Performance

The most important determinant of Na metal anode performance in RT Na-S cells with liquid electrolytes is the SEI formed on the anode surface. A strong, flexible SEI composed of inorganic species can accommodate the volume change during cycling and promote homogeneous Na plating and stripping, thus avoiding dendritic growth [69]. Meanwhile, a weak and brittle SEI composed primarily of inorganic species will crack during cycling and promote dendritic growth. In addition to artificial SEI formation and solid electrolyte use, carefully selecting the composition of the liquid electrolyte is a common strategy used to create a stable SEI [69]. It has been shown previously that a stable SEI composed primarily of inorganic species could be formed in a glyme ether-based electrolyte with sodium hexafluorophosphate ($NaPF_6$) salt [77]. However, a detailed comparison of the sodium plating and stripping performance in the different glyme solvents was not given in this study.

The electrolyte of an RT Na-S cell is an important determinant of the degree of polysulfide dissolution in the cell as well as the redox pathways of the cathodic reaction. Glyme ether solvents have been shown to dissolve polysulfides well, which can improve reaction kinetics as well as enhance the polysulfide shuttle effect [39]. Additionally, the electrolyte solvent can promote polysulfide disproportionation or dissociation reactions during cell operation that can alter the redox pathway and decrease capacity [58] [78]. Solvent choice plays a key role in RT Na-S cell design, but the specific effects of the different glyme ether solvents on cathodic phenomena is not yet fully understood.

2. ELECTROLYTES IN ROOM-TEMPERATURE SODIUM-SULFUR BATTERIES

2.1 Overview of RT Na-S Electrolytes

The electrolyte in a RT Na-S battery is the medium through which Na ions travel between the electrodes. It must have a high ionic conductivity and electrochemical stability within the voltage window of RT Na-S cells (~1-3 V), and it must be non-reactive with sulfur and intermediate polysulfide species [79]. The three base categories of electrolyte used in RT Na-S are solid, gel polymer, and liquid [80]. Solid electrolytes for RT Na-S batteries are typically a type of glass ceramic, but they also can be a solid polymer [81]. Liquid electrolytes are composed of a solid salt and possibly additional additives dissolved into a liquid solvent. In liquid electrolytes for RT Na-S cells, the solvent must be able to solvate sodium salts. Gel polymer electrolytes are fabricating using a liquid electrolyte salt and solvent, but polymers are added to the solution to form a semi-solid, flexible material. There are many different types of liquid electrolytes, and they can be further divided into aqueous liquid electrolytes and non-aqueous liquid electrolytes. In an aqueous liquid electrolyte, water is the solvent. A RT Na-S cell with an aqueous catholyte has been reported in the literature, but this cell used a solid electrolyte with a non-aqueous electrolyte on the anode side [82]. Na metal reacts explosively with water, so aqueous electrolytes cannot be used under normal circumstances in RT Na-S cells. Thus, non-aqueous liquid electrolytes are the preferred option. Non-aqueous electrolytes can be either organic or inorganic, and organic liquid electrolytes are by far the most common liquid electrolytes reported in the literature. Among liquid organic electrolytes, ethers (specifically, glyme ethers) and carbonates are the two most commonly used types. An organizational chart for the electrolytes used in RT Na-S batteries is given below as Figure 2.1.
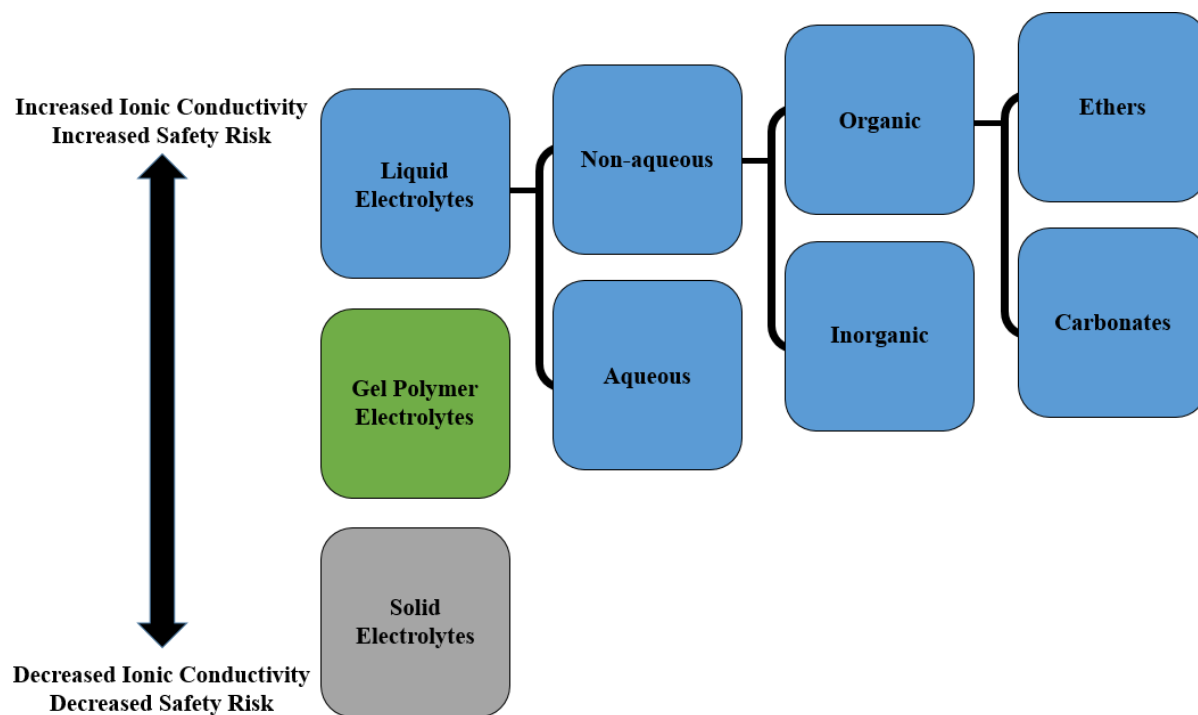
Figure 2.1. Classification of electrolytes for RT Na-S batteries.

As shown in Figure 2.1, ionic conductivity in electrolytes generally increases from solid to liquid, with solid electrolytes < gel polymer electrolytes < liquid electrolytes. Specifically, NASICON and other solid electrolytes have ionic conductivities on the order of 10^{-5} to 10^{-3} S cm^{-1} at room temperature [83] [84] [85]. Gel polymer electrolytes have ionic conductivities on the order of 10^{-4} to 10^{-3} S cm^{-1} at room temperature [57] [86]. Liquid electrolytes have ionic conductivities on the order of 10^{-3} to 10^{-2} S cm^{-1} at room temperature [87] [88]. In addition to having lower ionic conductivity at room temperature than gel polymer and liquid electrolytes, solid electrolytes make poor interfacial contact with solid electrodes, which hampers ion transport [85]. However, solid glass ceramic electrolytes do have a safety advantage over commonly used liquid electrolytes (glyme ethers and carbonates) since they are non-flammable. Pairing a highly reactive sodium metal anode with a flammable liquid presents a safety risk. Notably, not all organic liquid electrolytes are flammable. Triglyme (G3) and tetraglyme (G4) are both non-flammable solvents [89] [80].

The glyme ether solvents monoglyme (G1), diglyme (G2), G3, and G4 are organic chain molecules with methyl groups at each end [90]. The chain length and molecular weight increases

from G1 to G4, with G4 being the longest and heaviest molecule. G1, G2, G3, and G4 are all liquids at room temperature. They do not irreversibly react with solvated polysulfides and have also been shown to facilitate stable SEI formation on the Na anode surface [59] [77]. Thus, they are good candidates for RT Na-S electrolyte solvents. Figure 2.2 compares selected thermophysical and cost properties of G1, G2, and G4. G3-based electrolyte use in RT Na-S cells has been reported in the literature, but only in two publications [89] [60].
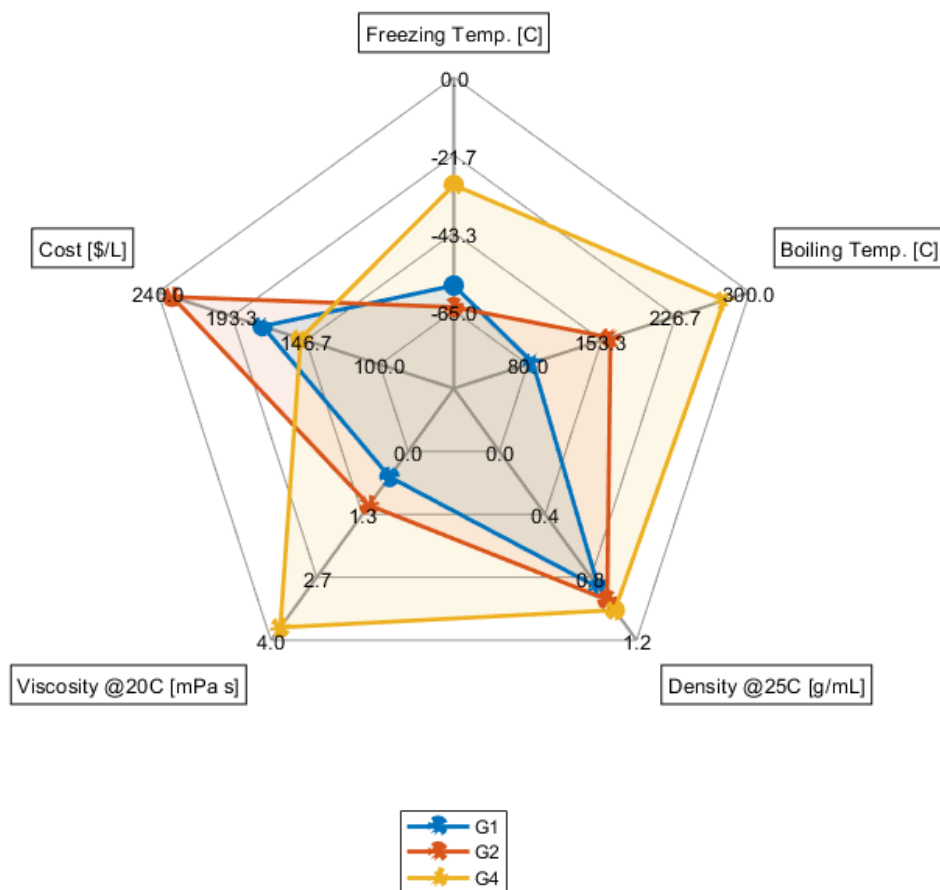
Figure 2.2. Selected thermophysical and cost properties of G1, G2, and G4. Data derived from [90], [91], [92], and [93]. MATLAB code for spider plot function found at [94].

Ionic conductivity is not shown in Figure 2.2 because it is also dependent on the dissolved salt as well as the solvent in a liquid electrolyte. However, for a given salt anion and concentration,

ionic conductivity increases from G4 to G1, with G1 having the highest ionic conductivity at room temperature among G1, G2, and G4 [88]. Figure 2.2 shows that as glyme chain length increases, boiling point, density, and viscosity all increase. Interestingly, G1 has a higher freezing temperature than G2. G1 has a much lower boiling temperature than G2 or G4, which indicates that it not as thermally stable as G2 or G4 [95]. G4 has a much higher freezing temperature than either G1 or G2, which shows that it is not suitable for low temperature applications. It is also important to note that G2 is more expensive than G4 by around $100 L^{-1}, which could be a significant consideration for the commercial production of RT Na-S batteries.

2.2   Literature Review: Electrolytes in RT Na-S Batteries

Although RT Na-S battery research is a relatively new field, there is a wealth of literature that probes how electrolytes influence RT Na-S operation and performance. As the bridge that connects the electrodes, electrolytes strongly influence the method in which Na is plated on and stripped from the anode, the degree to which polysulfides can dissolve and migrate away from the cathode, how the cell redox reactions proceed, and the overall cell performance. Here, the previous work studying electrolytes in RT Na-S batteries will be discussed and summarized.

2.2.1   *Effect of Electrolyte on Anode Stability and SEI*

In 2015, Zhi Wei Seh and colleagues published the first paper on liquid phase electrolytes for Na metal anode stability in RT Na-S batteries [77]. In this article, the authors reported long-term, stable cycling of sodium metal symmetric cells in an electrolyte composed of sodium hexafluorophosphate ($NaPF_6$) in glyme solvents. The authors postulated that the biggest barrier to stable plating and stripping of sodium metal anodes is unstable SEI formation, which breaks and reforms during dendritic plating. Symmetric cells constructed with G2 and $NaPF_6$ achieved coulombic efficiencies of 99.9% over 300 cycles. The authors stated that the reason for this long term stability is the uniformity, compactness, and composition of the SEI formed in this electrolyte. The $NaPF_6$/G2 electrolyte formed an SEI primarily composed of inorganic compounds like Na_2O and NaF, while the SEI formed in carbonate-based electrolytes contained organic compounds. A RT Na-S full cell was constructed with G2 and $NaPF_6$ that had a first cycle discharge capacity of 776 mAh g^{-1}, and a discharge capacity of just under 600 mAh g^{-1} at 20 cycles.

Working concurrently but published just after the work by Z.W. Seh *et al.* in 2015, J. Song *et al.* reported on the effect of an inorganic 5.3M $NaAlCl_4$ in SO_2 electrolyte on sodium metal anode performance [96]. The performance of this novel electrolyte was directly compared to an organic 1M $NaPF_6$ in EC:PC electrolyte. To evaluate the effect of the two electrolytes on electrochemical performance and SEI stability, the authors used electrochemical cycling of Na/Ni and Na/Na coin cells, electrochemical impedance spectroscopy (EIS), scanning electron microscopy (SEM), and x-ray photoelectron spectroscopy (XPS). Coin cells with the inorganic electrolyte exhibited much higher coulombic efficiency and cycle life than the coin cells with the organic electrolyte, which the authors attributed to non-dendritic plating/stripping and good solid/liquid interfacial stability in the inorganic electrolyte and dendritic plating/stripping and reactivity of the solvent with the Na electrodes in the organic electrolyte. EIS and SEM analysis revealed that the Na electrode surface in inorganic electrolyte was smooth, compact, and composed of cubic crystals, while the Na electrode surface in organic electrolyte was rugged, dendritic, and continued to grow and react with the electrolyte over the course of a week. XPS analysis showed that the SEI layer on the Na electrode in the inorganic electrolyte was primarily composed of inorganic NaCl, while the SEI on the Na electrode in the organic electrolyte was composed primarily of organic compounds and NaF. The 5.3M $NaAlCl_4$ in SO_2 electrolyte formed a compact and stable SEI on the surface of the Na electrode, and plating and stripping of Na during cycling was non-dendritic; however, it is unclear whether these results were due to the extremely concentrated electrolyte or the composition of the electrolyte itself.

In 2016, S. Wei *et al.* published a report on a RT Na-S cell containing a 1M $NaClO_4$ in EC:PC electrolyte with SiO_2-IL-ClO_4 additive (IL = ionic liquid) and sulfur-metal-organic framework microporous carbon composite cathode [48]. Galvanostatic cycling of the cell without the additive resulted in an excellent first discharge capacity of 1614 mAh g^{-1} at C/10 rate, which decreased to 800 mAh g^{-1} after 50 cycles. However, unstable cycling at high cycle numbers and at high rates in the carbonate electrolyte without the additive was attributed to reactivity of the Na anode with the electrolyte as well as unstable Na stripping/plating. Adding just 5 vol% SiO_2-IL-ClO_4 additive to the carbonate electrolyte enabled stable cycling with a discharge capacity of 600 mAh g^{-1} at C/2 (after a first discharge at C/10). The authors attributed this success to stable SEI

formation from the ionic liquid as well as the ability of the SiO_2 in the additive to reduce the concentrated electric fields that form dendrites on Na metal anodes by tethering the salt anions to the SiO_2 nanoparticles.

S. Choudhury *et al.* reported on an artificial coating of NaBr as the SEI on a sodium metal anode for homogenous, non-dendritic Na plating/stripping [97]. This study was computational as well as experimental, with joint density-functional theory calculations used to find that NaBr in a liquid electrolyte of acetonitrile had a surface diffusion energy barrier as low as that of Mg metal in a vacuum, which does not form dendrites during plating and stripping. SEM and XPS analysis confirmed the existence of a flat and compact layer of NaBr on a Na electrode treated with 1-bromopropane. EIS and theoretical analysis on symmetric Na/Na cells in 1M $NaPF_6$ in EC:PC revealed that at any temperature and at any current density, Na ion transport is faster in an SEI composed of NaBr or NaCl than in the naturally formed SEI. Optical cell microscopy experiments revealed the formation of dendrites on the untreated Na electrode, but plating on the NaBr treated electrode was homogenous. Galvanostatic cycling of Na/Na symmetric coin cells revealed low and constant overpotentials over time in the cells with NaBr treated electrodes, but the untreated cells showed high resistance during cycling. RT Na-S cells with a NaBr treated Na metal anode showed high coulombic efficiency and low capacity fade over 250 cycles. This work provided further evidence of the ability of inorganic sodium halide compounds to form stable and homogenous SEIs on Na metal anodes.

Other authors have investigated the beneficial effects of artificial SEI formation on Na metal anodes. G. Wang *et al.* found that an artificial SEI composed of NaF could enable dendrite-free sodium stripping and plating [98]. V. Kumar *et al.* found that an artificial SEI composed of NaOH and $NaNH_3$ provided a both strength and flexibility and enabled high-rate cycling in Na/Na symmetric cells [99].

H. Wang *et al.* found that an electrolyte additive of 0.033M Na_2S_6 polysulfide in 1M $NaPF_6$/G2 created a stable SEI that prevented dendrite growth, and enabled stable, long-term plating and stripping for over 400 cycles [100]. Conversely, an electrolyte additive of 0.033M and 1 wt% $NaNO_3$ in a cell with the same base electrolyte exhibited large overpotentials and failed at

around 150 cycles. In this cell, an organic SEI was formed that does not adequately protect against dendrite growth. The cell with no additives failed after the 78th cycle. These tests used a current density of 2 mA cm^{-2} and an areal capacity of 1 mAh cm^{-2}. The authors varied the concentration of the polysulfide additive, and found that 0.067M was the optimal concentration due to its decisive performance over the 0.033M additive at a current density of 5 mA cm^{-2}. Pre-treating Na anodes before plating/stripping also yielded favorable results, as full Na-S cells with pre-treatment at 0.067M polysulfide discharge to 621 mAh g^{-1} on first cycle (508 mAh g^{-1} after 30 cycles), while Na-S cells with no pre-treatment discharged to 252 mAh g^{-1} on first cycle (159 mAh g^{-1} after 30 cycles). To conclude, employing the Na_2S_6 polysulfide as an electrolyte additive or anode pre-treatment at the right concentration can form a stable SEI on the anode surface.

The electrolyte additive fluoroethylene carbonate (FEC) has been shown to create a stable and robust SEI that can enable dendrite-free plating and stripping in RT Na-S cells. J Wu *et al.* studied a RT Na-S cell with 2M NaTFSI in trimethyl phosphate (TMP):FEC (7:3 v:v) [101] and found that the FEC solvent enabled the formation of an inorganic SEI composed primarily of NaF, which improved anode performance. Moreover, the TMP-based electrolyte could not be ignited with an applied flame and extinguished an existing flame, showing that it has superior safety properties over carbonate electrolytes.

2.2.2   *Effect of Electrolyte on Polysulfide Shuttle*

The effects of different electrolyte compositions on the SEI of pre-sodiated hard carbon anodes were studied by M. Kohl *et al.* [102]. In particular, they tested how the SEIs formed in these electrolytes and electrolyte additives would affect the polysulfide shuttle mechanism. Polysulfide shuttle was quantified by the discharge capacity and coulombic efficiency of the full cell, as well as the current measured by cyclic voltammetry (CV) between 2.3 and 2.5 V during the charge. In the article, the authors posited that polysulfide shuttle can be mitigated through the use of an optimal electrolyte that prohibits the transfer of electrons from the anode to the electrode-electrolyte interface. They claimed that the formation of a stable SEI is very difficult in sodium metal anodes, so they employed sodiated hard carbon anodes instead to improve performance. It is well known that $LiNO_3$ as an electrolyte additive improves cycling stability in Li-S cells; however, because of the increased reactivity of Na metal over Li metal, it is not as effective in RT

Na-S cells. The authors showed that hard carbon anodes sodiated in a 1M NaPF$_6$ in DEC:EC electrolyte with 1% volume FEC as an additive and then used in full RT Na-S cells with hard carbon anodes and a 1M NaClO$_4$, 0.2M Na$_2$S/P$_2$S$_5$ (additive) in G4 effectively mitigated polysulfide shuttle through improved discharge capacity, longer cycle life, improved coulombic efficiency, and lower CV shuttle currents. Hard carbon anodes were also sodiated in a 1M NaCF$_3$SO$_3$ in G4 electrolyte, and the full cells were cycled without the Na$_2$S/P$_2$S$_5$ additive, but these cases resulted in poorer performance. The better performance in the 1M NaPF$_6$ in DEC:EC:FEC sodiation electrolyte and 1M NaClO$_4$, 0.2M Na$_2$S/P$_2$S$_5$ in G4 full cell electrolyte was due to the thick, stable SEI that forms on the anode that prevents reduction of soluble polysulfides on the anode as well as the interactions between soluble polysulfides and the P$_2$S$_5$ additive that promoted reduction. Their tailored electrolytes enabled a first discharge capacity of 1000 mAh g^{-1} that decreased to 200 mAh g^{-1} after 1000 cycles.

X. Xu *et al.* studied a RT Na-S cell with a complex electrolyte consisting of 2M NaTFSI in PC:FEC electrolyte with 10 mM InI$_3$ additive [87]. They believed that the concentrated NaTFSI salt and FEC solvent inhibited the polysulfide shuttle mechanism by decreasing the solubility of polysulfides and providing a weak binding energy for polysulfides, respectively. In addition, the InI$_3$ additive mitigated the harmful effects of the polysulfide shuttle by forming a protective barrier on the anode surface that prevented polysulfide corrosion on the surface. The InI$_3$ additive also improved the naturally slow kinetics of Na$_2$S oxidation to higher order polysulfides during the charge [103]. XPS analysis of Na anodes cycled in this electrolyte revealed an SEI filled with fluorine from the salt and FEC that stopped dendrites from growing during plating. It also showed that peaks associated with sulfur anions disappeared in the presence of I and In, suggesting that the additive prevented polysulfide corrosion. This electrolyte also enabled superb electrochemical performance, as a first discharge capacity of 1635 mAh g^{-1} was achieved, showing remarkable sulfur utilization. The average coulombic efficiency as well as the cell resistances were lower as compared to a cell without concentrated salt, FEC or InI$_3$ additive. The practical specific energy achieved by this electrolyte was greater than those of Li-ion batteries, based on its ability to mitigate the polysulfide shuttle.

Because gel polymer electrolytes can mitigate the speed of polysulfide dissolution as well as safety concerns in RT Na-S cells, D. Zhou *et al.* investigated a RT Na-S cell with polymer-based sulfur cathode and a gel polymer electrolyte [86]. The gel polymer electrolyte was fabricated by subjecting a solution of monomers, a photo-initiator, and 1M NaTFSI in PC:FEC. At room temperature, the gel polymer electrolyte possessed the same ionic conductivity as the non-polymeric liquid electrolyte. Symmetric Na/Na cells cycled for 300 hours exhibited a stable voltage profile, which indicated stable, non-dendritic Na plating/stripping. The gel polymer electrolyte also exhibited a strong binding energy with long-chain soluble sodium polysulfides, which prevented polysulfide dissolution and mitigated the polysulfide shuttle. Galvanostatic cycling of Na/gel polymer electrolyte/polymerized S-C cells at room temperature yielded high discharge capacities and stable cycling even up to rates of 2C, showing an inhibited shuttle effect. Additionally, the Na metal anode in this cell had a sulfur content of <1 wt%, providing further evidence for a successfully mitigated polysulfide shuttle.

Ceramic solid state electrolytes can also be useful in preventing the polysulfide shuttle effect. X. Yu and A. Manthiram reported that a $Na_3Zr_2Si_2PO_{12}$ ceramic solid electrolyte coated with a thin nanoporous polymer on the anode side in RT Na-S cell prohibited polysulfides from leaving the cathode [83]. The thin polymer layer on the anode side was necessary to improve the interfacial ionic conductivity. Electrochemical cycling of RT Na-S cells with the ceramic solid electrolyte-polymer coating showed better capacity retention and discharge capacities than those without, and X-ray diffraction (XRD), EDS, and simple optical experiments showed that the solid electrolyte with polymer layer successfully prevented migration of polysulfides to the anode.

Most SEI research regarding RT Na-S batteries focuses on the SEI on the Na metal anode. However, H. Lee *et al.* took a different approach and studied the *in-situ* development of a cathode SEI using a FEC electrolyte additive [104]. The combined effect of adding 8 wt% FEC as an additive to a 1.5M $NaClO_4$ in PC electrolyte along with an electrochemical pre-treatment of cell discharge to 0.6 V formed an SEI primarily composed of NaF and organic compounds on the S-C composite cathode that could effectively mitigate the polysulfide shuttle. The combination of the treatment and additive allowed for better discharge capacities and capacity retention than cells with only one treatment or no treatment at all during galvanostatic cycling. This cell also showed

impressive capacity retention even at high currents. The authors credited this performance to the cathode SEI that prevented polysulfides from migrating away from the cathode through the electrolyte. X. Zhao *et al.* also found that a 5 wt% FEC electrolyte additive enabled the formation of an SEI primarily composed of inorganic compounds that improved cell performance [105].

2.2.3   Redox Mechanisms in Different Electrolytes

C.-W. Park *et al.* investigated the discharge mechanism of the RT Na-S cell in PVDF gel polymer electrolyte in their pioneering 2006 paper [57]. Based on XRD scans of the fully charged and fully discharged cathodes, the authors concluded that Na_2S_3 and Na_2S_2 were the final discharge products in their voltage window of 3.0 - 1.0 V. They also observed two voltage plateaus during the discharge that occurred at 2.28 V and 1.73 V, which were verified from CV. From theory, the authors determined that the upper voltage plateau at 2.28 V could not have come from the reduction of sulfur to Na_2S_3 or Na_2S_2, and instead must have been due to the reduction of sulfur to long-chain polysulfides. They attributed the lower discharge plateau at 1.73 V to the formation of Na_2S_3 and Na_2S_2. Since the first discharge capacity of 489 mAh g^{-1} was much less than the theoretical discharge capacities from the reduction of sulfur to Na_2S_3 or Na_2S_2, the authors hypothesized that dissolution of polysulfides into the PVDF gel polymer electrolyte was to blame. This was the first mention of the polysulfide shuttle at work in RT Na-S batteries. C.-W. Park *et al.* noted that the rapid capacity fading observed within the first 20 cycles could be due to irreversible polysulfide formation.

In 2008, J.-S. Kim *et al.* repeated the work of C.-W. Park *et al.* but tested their Na/PVDF/S cell at a current density that was twice as high [106]. The first discharge capacity was slightly lower than the cell cycled at the lower current density. The authors observed the same discharge mechanism as in the previous study, but they did note that the plateau regions in the discharge profile shrank as the number of cycles increased. They also noted that the upper plateau that they associated with long-chain polysulfide formation disappeared first within 10 cycles. During charge, CV scans at slow sweep rates found two oxidation peaks (corresponding to voltage plateaus during the charge profile) at 2.1 V and 2.5 V.

In 2011, H. Ryu *et al.* investigated the discharge mechanism in a RT Na-S cell with liquid 1M NaCF$_3$SO$_3$ in G4 electrolyte through galvanostatic cycling, differential scanning calorimetry (DSC), and XRD analysis, which represented the first investigation into the redox mechanisms of RT Na-S cells with liquid electrolytes [107]. Their cell was cycled between 2.3 and 1.2 V, and it was found that the voltage profile sloped downwards between 2.23 and 1.66 V, and then displayed one single plateau at 1.66 V. By means of DSC and XRD analysis of cathodes in cells discharged (or charged) to certain points along the discharge-charge curves, the authors could identify specific compounds that exist at the key points in the discharge-charge process. In the fully charged, original cathode, elemental sulfur was observed without the presence of sodium polysulfides. During the sloping region between 2.23 V and 1.66 V, sulfur was observed as well as the polysulfides Na$_2$S$_5$, Na$_2$S$_4$, and Na$_2$S$_3$. In the plateau region at 1.66 V, all of these same compounds were observed, but sulfur and Na$_2$S$_5$ existed in only small quantities. Upon full discharge, Na$_2$S$_3$ and Na$_2$S$_2$ were present in the cathode. When the cell is recharged, sulfur as well as Na$_2$S$_4$ and Na$_2$S$_5$ existed in the cathode, showing that the oxidation back to sulfur is not fully reversible. SEM images and EDS analysis of the cathode and anode confirmed the DSC and XRD results. Notably, the sulfur content on the sodium anode increased with discharge, providing evidence for the polysulfide shuttle effect in the cell. None of the higher order (n > 5) polysulfides were observed, and the theoretical final discharge product of Na$_2$S was not observed in the cell. The discharge and charge reactions proposed by H. Ryu *et al.* are given by Equations 2.1 and 2.2 below.

$$\text{Discharge:} \qquad 2Na + nS \rightarrow Na_2S_n\left(5 \geq n \geq 2\right) \rightarrow Na_2S_n\left(4 > n \geq 2\right) \qquad (2.1)$$

$$\text{Charge:} \qquad 2Na_2S_n\left(4 > n \geq 2\right) \rightarrow 2Na + nS + Na_2S_n\left(5 > n \geq 3\right) \qquad (2.2)$$
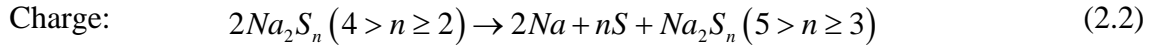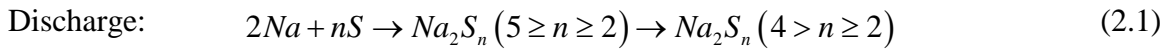
In 2013, S. Wenzel *et al.* used galvanostatic cycling and XPS to further investigate the redox mechanisms at work in the RT Na-S cell [60]. The authors claimed that using XRD and methods of thermal analysis like DSC is unreliable, which potentially discredits the findings of H. Ryu *et al.* (2011). In their experiments, RT Na-S cells with 1M NaCF$_3$SO$_3$ in DOL:G1 electrolyte and 50% sulfur mass loading were cycled at C/10 between 2.3 and 1 V. The authors observed two voltage plateaus in the discharge profile at 2.2 V and between 1.6 and 1.7 V. They attributed the

first and second voltage profiles to the formation of polysulfides from sulfur and the reduction of Na_2S_2 to Na_2S, respectively. The location and number of plateaus was very similar to the results obtained by H. Ryu e*t al*., despite the use of a different electrolyte. Only one plateau at 1.85 V was observed during charging, and the authors found that the average shape of the voltage profile did not change with repeated cycling. The XPS analysis showed that Na_2S did form in the discharge process, and it completely disappeared upon full recharge. However, the redox reactions were not complete, as polysulfides were found in the fully discharged and fully charged electrodes. XPS analysis also found polysulfides and sodium sulfide on the sodium anode as a result of the polysulfide shuttle effect. The key findings of this work were evidence for the reversible conversion of polysulfides to sodium sulfide in RT Na-S cells, the ability to reduce the detrimental capacity fading caused by the polysulfide shuttle by introducing solid beta-alumina electrolyte as a cell separator, and the negative side reactions caused by the PVDF binder. The discharge and charge reactions proposed by S. Wenzel *et al.* are given below by Equations 2.3 and 2.4.

$$\text{Discharge:} \qquad Na + S_8 \rightarrow Na_2S + Na_2S_x \left(x_{average} = 2.1 \right) \qquad (2.3)$$

$$\text{Charge:} \qquad Na_2S + Na_2S_x \rightarrow Na + S_8 + Na_2S_y \left(y_{average} = 8.5 \right) \qquad (2.4)$$
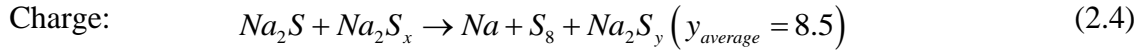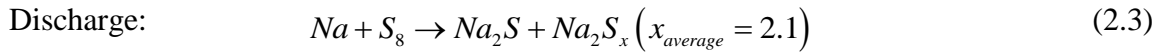
In 2014, X. Yu and A. Manthiram studied the discharge mechanism of a RT Na-S cell with 1.5M $NaClO_4$, 0.3M $NaNO_3$ (additive) in G4 electrolyte with a nanostructured carbon-based interlayer between the cathode and separator [45]. Electrochemical cycling, CV, XPS, and UV-vis spectroscopy were used to study the cell performance and redox reaction mechanism. From the discharge profile during the first charge and the supporting CV scans, the authors divided the discharge curve into four characteristic regions. Region I described the first voltage plateau at 2.2 V, where solid sulfur in the cathode was reduced to Na_2S_8 in solution. Region II described the downward sloping region between 2.20 V and 1.65 V, where Na_2S_8 was reduced to Na_2S_4. It was noted that this is the most complex region, and many different long-chain polysulfides existed in equilibrium. Region III described the second voltage plateau at 1.65 V, where Na_2S_4 in solution was converted to the insoluble Na_2S_3, Na_2S_2, and Na_2S through three simultaneous reduction reactions. Region IV represented the sloping region between 1.65 V and 1.2 V, where solid Na_2S

was formed from solid Na_2S_2. This last reaction suffered from slow kinetics. The UV-vis scan of cathode material discharged to 1.8 V showed evidence of multiple forms of long-chain polysulfide in equilibrium, and the XPS data of a cathode discharged to 2.2 V showed that sulfur was still present, but was not present in a fully discharged cathode. The discharge mechanism proposed by X. Yu and A. Manthiram is shown by Equations 2.5-2.8 below.

Region I (2.20 V) $\qquad$ $S_8 + 2Na^+ + 2e^- \rightarrow Na_2S_8$ $\qquad$ (2.5)

Region II (2.20-1.65 V) $\qquad$ $Na_2S_8 + 2Na^+ + 2e^- \rightarrow 2Na_2S_4$ $\qquad$ (2.6)

Region III (1.65 V) $\qquad$ $Na_2S_4 + \frac{2}{3}Na^+ + \frac{2}{3}e^- \rightarrow \frac{4}{3}Na_2S_3$ $\qquad$ (2.7a)

$$Na_2S_4 + 2Na^+ + 2e^- \rightarrow 2Na_2S_2 \qquad (2.7b)$$

$$Na_2S_4 + 6Na^+ + 6e^- \rightarrow 4Na_2S \qquad (2.7c)$$

Region IV (1.65-1.20 V) $\qquad$ $Na_2S_2 + 2Na^+ + 2e^- \rightarrow 2Na_2S$ $\qquad$ (2.8)
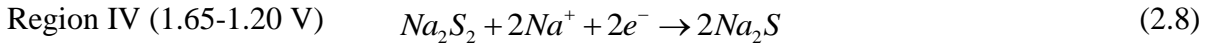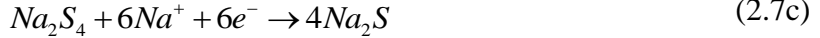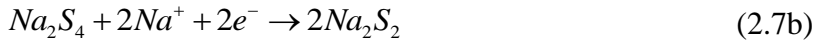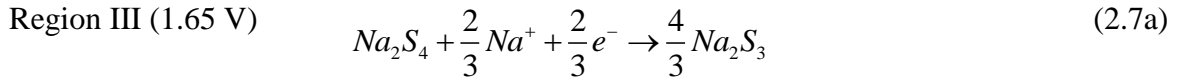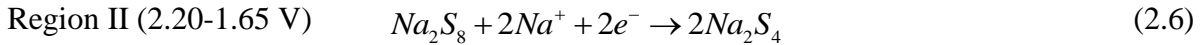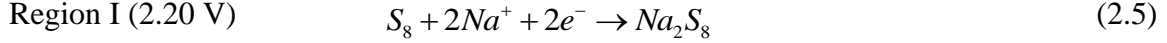
S. Wei *et al.* also discussed the reaction mechanism in their RT Na-S cell with sulfur-metal-organic framework derived microporous carbon composite cathode and 1M $NaClO_4$ in EC:PC electrolyte with SiO_2-IL-ClO_4 additive that arose from the interaction of the cathode with the carbonate-based electrolyte [48]. Based on CV, XPS, NMR, and UV-vis analysis, the authors proposed a solid-state reaction in which S_8 interred in the carbon micropores reduces directly to Na_2S_2 and then Na_2S, without the formation of soluble polysulfide species. At full discharge, nearly all of the sulfur in the cathode was reduced to Na_2S. The authors believed this reaction mechanism was due to the weak solvating ability of the carbonate electrolyte as well as the ability of microporous carbon to securely retain the sulfur.

In 2020, L. Medenbach *et al.* studied how additives and different solvents affected the performance of a RT Na-S cell constructed as a glass cell with separate chambers for the electrodes separated by a solid electrolyte tube of beta-alumina [108]. A liquid catholyte comprised of 0.25-0.5M $NaCF_3SO_3$ and 5mM Na_2S_4 in G2 was used as the cathode, and solid metal Na in 0.25-0.5M $NaCF_3SO_3$ in G2 was used as the anode. Due to the slow redox kinetics of the insoluble solid discharge products (i.e. Na_2S_2 and Na_2S), charging the cell was difficult. By changing the catholyte so that it consisted of 0.5M $NaCF_3SO_3$, 1mM Na_2S_5, and 1.67mM P_2S_5, the reversibility improved greatly. The authors postulated that this improvement was the result of the addition of P_2S_5 to the catholyte, which sped up oxidation of the solid products. Y.X. Ren *et al.* concurrently found that P_2S_5 as an electrolyte additive could improve kinetics of low-order polysulfides during discharge [103]. Despite the improvements through additive addition, the cycle life of the cell was still poor. The authors made a final adjustment by replacing G2 with tetramethylurea (TMU) as the catholyte solvent. The TMU solvent improved cycle life, and the cell with this catholyte actually showed an improvement in capacity after 10 cycles. As an electrolyte solvent for RT Na-S batteries, TMU with 0.5M $NaCF_3SO_3$ had a higher ionic conductivity at room temperature but a smaller electrochemical stability window than G2. UV-vis spectroscopic analysis during discharge and charge revealed that TMU facilitated the formation of the $S_3^{\bullet-}$ radical anion as the dominant reaction product, indicating that the redox reaction did not proceed through the typical two-electron electron pathway as in ether- and carbonate-based cells.

The catholyte cell design in which the standard sulfur-carbon solid phase cathode is replaced by a liquid phase solution of polysulfides is not a novel concept. In 2014, X. Yu and A. Manthiram reported on a RT Na-S cell with a dissolved polysulfide/carbon nanotube fabric cathode [46]. The catholyte consisted of 1.5M $NaClO_4$, 1.5M Na_2S_6, and $NaNO_3$ as an additive in G4. The catholyte cell exhibited superior capacity output than the control cell with a solid phase cathode. The authors also noticed that the capacity fade was most evident in the lower discharge plateau, during which the long-chain polysulfides are reduced to short-chain polysulfides and sodium sulfide. This indicates that the precipitation and dissolution of Na_2S is kinetically hindered due to its low electronic conductivity. By raising the cutoff voltage from 1.2 to 1.8 so that only long-chain polysulfides $(4 \leq n \leq 8)$ were formed while avoiding the formation of the kinetically slow short-chain polysulfides, the catholyte-based cell could cycle with almost no capacity fade

for 100 cycles. Since half of the theoretical capacity of the reduction of sulfur comes from the conversion of Na_2S_2 to Na_2S, the reversible capacity of the cell with a high cutoff voltage was approximately 250 mAh g^{-1}. The reversibility of the sulfur/long-chain polysulfide redox reactions was not limited to RT Na-S cells with a catholyte, as the same group found similar results in a RT Na-S cell with a S-C solid phase cathode [65]. By eliminating the short-chain polysulfides from the redox pathway, the S-C/1.5M $NaClO_4$, 0.3M $NaNO_3$ in G4/Na cell achieved almost no capacity fade over 50 cycles, with discharge capacities around 250 mAh g^{-1}. The full cell reaction of this cell cycled between 2.8 and 1.8 V is given by Equation 2.9 below.

$$nS + 2Na \rightleftharpoons Na_2S_n \left(4 \leq n \leq 8 \right) \tag{2.9}$$
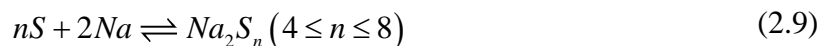
H. Yang *et al.* studied the kinetics of the redox mechanism in RT Na-S cells in an open-system, catholyte-based cell [109]. Their cell was designed so that catholyte could continually flow into and out of the cell in order to eliminate the diffusion effect in organic liquid electrolytes. The catholyte consisted of 1.5M $NaClO_4$, 0.2M $NaNO_3$ (additive), and varying concentrations of either Na_2S_8, Na_2S_6, Na_2S_4, or Na_2S_2, respectively. Analysis of chronoamperometry results showed that Na_2S_2 had a much lower redox activity than the long-chain polysulfides, which gave further evidence that the irreversible formation of short-chain polysulfides is a significant cause of capacity fade in RT Na-S cells.

In 2021, J. He *et al.* studied a highly concentrated electrolyte for RT Na-S cells consisting of G1:NaFSI:TTE (1,1,2,2-tetrafluoroethyl) in a 1:1.2:1 ratio [110]. This electrolyte enabled stable, long-term cycling by preventing polysulfide dissolution through a solid state reaction mechanism and by creating a compact and homogeneous SEI on the Na anode surface. In Na/Na symmetric cells, the G1:NaFSI:TTE electrolyte enabled lower overpotentials and longer cycle life than G4- or carbonate-based electrolytes. This was accomplished by facilitating the formation of a stable SEI rich in inorganic compounds. By carefully tuning the ratio of salt to G1 solvent, the authors could minimize the number of polysulfides that could be dissolved into the solvent. The highly concentrated electrolyte was able to form an SEI on the cathode surface due to interactions between the salt and polysulfides. As a result, the reaction proceeded primarily in the solid state. The proposed reaction mechanism is given by Equation 2.10 below.

Voltage > 1.3 V $\qquad$ $2S + 2Na \rightleftharpoons Na_2S_2$ $\qquad$ (2.10a)

Voltage < 1.3 V $\qquad$ $Na_2S_2 + 2Na \rightleftharpoons 2Na_2S$ $\qquad$ (2.10b)
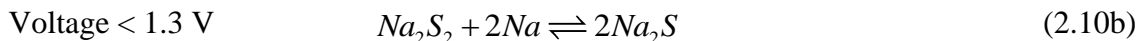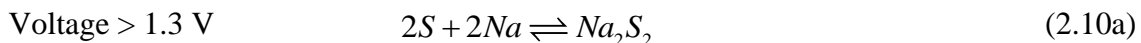
2.2.4 Electrolyte Solvent and Salt Comparison Studies

L. Carbone *et al.* studied the thermal stability, transport properties, and electrochemical performance of 1M NaCF$_3$SO$_3$ in G1 and G2 electrolytes for use in RT Na-S cells [95]. Thermal gravimetric analysis (TGA) revealed a greater thermal stability for temperatures below 100°C for the G2-based electrolyte. Pulse field gradient nuclear magnetic resonance (PFG NMR) showed greater mobility of solvent molecules than for salt ions in both the G1- and G2-based electrolytes, and the ions in the G1-based electrolyte diffused faster than those in the G2-based electrolyte due to the lower viscosity of G1. EIS and NMR revealed different ionic conductivities for the two electrolytes, but EIS showed that both electrolytes had the same ionic conductivity on the order of 10^{-3} S cm^{-1}. Galvanostatic cycling and EIS of Na/Na symmetric cells in both electrolytes revealed a higher initial overpotential in the G1-based electrolyte, but the G1 electrolyte presented lower overpotentials during cycling and lower interfacial resistance than the G2-based electrolyte. When tested in RT Na-S cells, the cell with the G2-based electrolyte showed higher initial discharge capacity and better capacity retention than the cell with the G1-based electrolyte. The authors concluded that the G2-based electrolyte was superior to the G1-based electrolyte for application in RT Na-S cells.

H. Zhang *et al*. studied solvent dependent redox mechanisms by comparing cell performance with glyme- and carbonate-based electrolytes [59]. 1M NaClO$_4$ in G4 with 0.2M NaNO$_3$ as an additive was used as the glyme-based electrolyte, while 1M NaClO$_4$ in PC:EC with 5 wt% FEC was used as the carbonate-based electrolyte. CV revealed a three step reduction in the G4-based electrolyte with peaks at 2.2 V, 1.6 V, and 1.0 V, while the oxidation occurred in two steps at 2.0 V and 2.4 V. However, CV scans of a cell with PC:EC-based electrolyte revealed only one reduction step at 2.1 V and no oxidation steps at all, indicating an irreversible redox reaction.

Galvanostatic cycling confirmed the CV results, with the G4-based cell showing a high initial discharge capacity and coulombic efficiency of 93.5%, while the PC:EC-based cell showed a much lower intial discharge capacity and no reversibility. *In-situ* XRD study of the G4-based cell at different points during discharge and charge revealed that elemental sulfur is reduced to Na_2S_2 at the end of discharge, and could be oxidized back to elemental sulfur (potentially S_6) at the end of charge. In contrast, no polysulfide products were identified in the PC:EC-based cell at the end of discharge. *Ex-situ* XPS was also performed on both cell types at various discharge and charge points. In the G4-based cell, Na_2S was detected at the end of the discharge, but the dominant discharge product appeared to be Na_2S_2. After recharge, Na_2S was still observed in the cell, showing the oxidation of this product was kinetically slow and partially irreversible. In the EC:PC based cell, only sulfur and Na_2S_8 were detected at the end of discharge. The G4-based cell exhibited a thorough and reversible step-wise reduction from sulfur to long-chain polysulfides to short-chain polysulfides, while the EC:PC cell exhibited an incomplete reduction and no reversibility due to side reactions between the polysulfides and solvent. H. Liu *et al.* also compared ether- and carbonate-based electrolytes in RT Na-S cells [111]. In sulfur cathodes with low sulfur mass loadings that inter the sulfur into carbon pores, carbonate-based electrolytes could enable solid state redox reactions. However, sodium polysulfides reacted irreversibly with the carbonate solvent in high sulfur mass loading cathodes. In contrast, RT Na-S cells with ether-based electrolytes could operate stably with high sulfur mass loading cathodes through solid-liquid redox reactions.

In 2017, L. Lutz *et al.* studied the impact of electrolyte salt anion on SEI formation in Na metal anodes [112]. Specifically, they studied the performance of $NaPF_6$, $NaClO_4$, $NaCF_3SO_3$, and NaTFSI salts in G1, acetonitrile (ACN), and dimethyl sulfoxide (DMSO) solvents. Na-NMR results revealed that in weakly solvating solvents like G1, the salt anion played a large role in Na ion solvation. Aging studies of Na/Na symmetric cells in salt/G1 electrolytes using EIS found that the PF_6^- anion was superior in creating a stable SEI over the other three anions studied. XPS analysis of the aged electrodes revealed the presence of both inorganic and organic species in the Na SEI. The inorganic NaF and NaCl components were products of interactions between the salt and the Na metal, while the organic compounds present in the SEI arose from reactions between the Na metal and G1. A thin SEI composed primarily of NaF was observed in the $NaPF_6$ electrolyte,

46

while thick layers primarily of NaF and NaCl were observed in the $NaCF_3SO_3$ and $NaClO_4$ electrolytes, respectively. On the NaTFSI electrode, it was found that the SEI had only small amounts of NaF and also incorporated fragments from the large anion. Cycling tests of the Na/Na symmetric cells in the different G1-based electrolytes revealed long-term, stable cycling in the $NaPF_6$ electrolyte, but the $NaClO_4$- and NaTFSI-based electrolytes could not cycle well. Thus, a thin, uniform SEI composed of NaF was found to be very important for cycling effectiveness. This work illustrated the anion dictated SEI formation on Na metal electrodes.

2.2.5   *Analysis of Literature Meta-Data*

Without a direct comparison, it is difficult to understand how the different electrolyte choices affect full cell performance in RT Na-S cells. To complicate things, cell performance is a complex function of many different variables. Cathode architecture including sulfur mass loading, operating conditions including cycling rate and temperature, and choice of separator can affect cell performance. In the electrolyte alone, salt composition, salt concentration, solvent composition, and additives all strongly influence cell performance. In fact, there are no set of established standards for cell performance in RT Na-S batteries since they are still in the research and development phase. Cycling statistics at C/10 relative to the capacity of the sulfur electrode (1672 mAh g^{-1}) are often given, but even this is not a good comparison metric since the sulfur loading used in experimental cathodes varies across the literature. Furthermore, the definition of long-term capacity is not well defined, with some publications reporting reversible capacity after cycle numbers on the order of 1000, and some reporting capacity after a few hundred [74] [87]. In order to evaluate cell performance observed in the literature for different types of electrolytes, the dependent variables initial specific discharge capacity and discharge capacity fade between the first and second cycles were selected. Initial specific discharge capacity is a good measure of the maximum sulfur utilization in a cell before the performance inhibiting factors of RT Na-S cells begin to dominate. Not all publications report cycling data for hundreds or thousands of cycles, but all report at least two cycles. Furthermore, the discharge capacity fade between the first and second cycles is almost always the largest cycle-to-cycle fade, and it is a good measure of how reversible the initial performance is. Thus, first to second cycle discharge capacity fade is the second dependent cell performance variable selected. For the independent variables, sulfur mass fraction in the cathode as well as cycling current density were selected since they represent cathode

architecture and operating conditions. Electrolyte type was not used as an independent variable, but instead was used to sort the data and observe any trends among electrolytes at each independent value. For this analysis, 25 cells from 24 publications were used, and each of the two dependent variables is plotted against each independent variable. The effect of current density, sulfur content, and electrolyte type on initial specific discharge capacity and first-second cycle discharge capacity fade in the literature is shown in Figure 2.3.
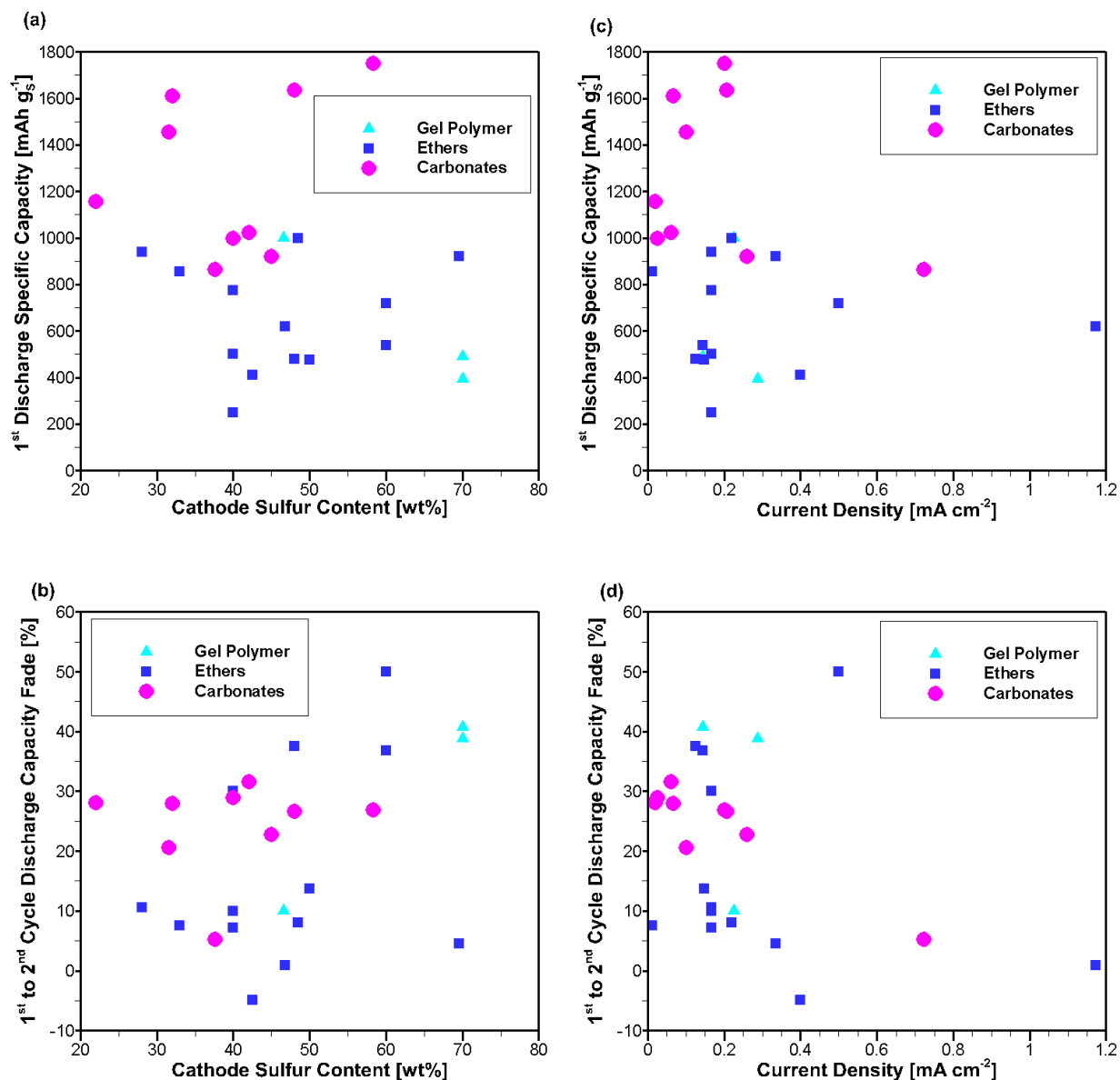
Figure 2.3. Aggregated data from the literature that shows the dependency of initial discharge specific capacity on **(a)** sulfur content and **(c)** current density as well as the dependency of capacity fade between the 1st and 2nd cycles on **(b)** sulfur content and **(d)** current density. The data is organized by electrolyte type (ether-based, carbonate-based, or gel polymer electrolytes) to show how the choice of electrolyte affects full cell performance. Data derived from [57], [113], [106], [107], [60], [75], [64], [114], [115], [77], [48], [102], [116], [74], [95], [87], [86], [104], [100], [89], [59], [117], [66], and [110]. In references [77], [74], and [95], the cycling rate is given as a C-rate, and no active material areal loading was given to convert current density to mA cm^{-2}. In these cases, a reasonable assumption was made that the areal loading of sulfur in the cathode was 1.0 mg cm^{-2}. In order to determine first-second discharge capacity fade, second cycle discharge specific capacity usually had to be read off of graphs, and is thus an estimation.

In Figure 2.3, electrolyte type is defined by the solvent. In the selected publications, the authors used ether-based electrolytes, carbonate-based electrolytes, and gel polymer electrolytes, which are represented by blue squares, magenta circles, and cyan triangles, respectively. Two trends are immediately obvious from the aggregated data. First, carbonate-based electrolytes appear to have higher initial discharge specific capacities than ether-based electrolytes across all sulfur content and cycling rate points. Second, ether-based electrolytes generally had lower capacity fades between the first and second cycles than the carbonate-based electrolytes, which is very obvious in Figure 2.3(d). Specifically, the average initial discharge capacities from 13 ether-based cells and 9 carbonate-based cells in the literature were 652.8 mAh g^{-1} and 1268.6 mAh g^{-1}, respectively. The average first-to-second discharge specific capacity fades from these same 13 ether-based cells and 9 carbonate-based cells were 16.3% and 24.3%, respectively. One explanation for the large initial discharge capacities followed by rapid fading observed in carbonate-based electrolytes is that the soluble polysulfides could react irreversibly with the solvent molecules in unwanted side reactions, a phenomenon observed in Li-S cells [39] [59]. From this analysis, ether-based cells had good reversibility during the first two cycles compared to carbonate-based electrolytes. In order to further refine the data presented in Figure 2.3 for the specific types of ether-based electrolytes, carbonate- and gel-polymer based cells were excluded, and the 13 ether-based cells were organized by specific glyme solvent. This analysis is shown below in Figure 2.4.
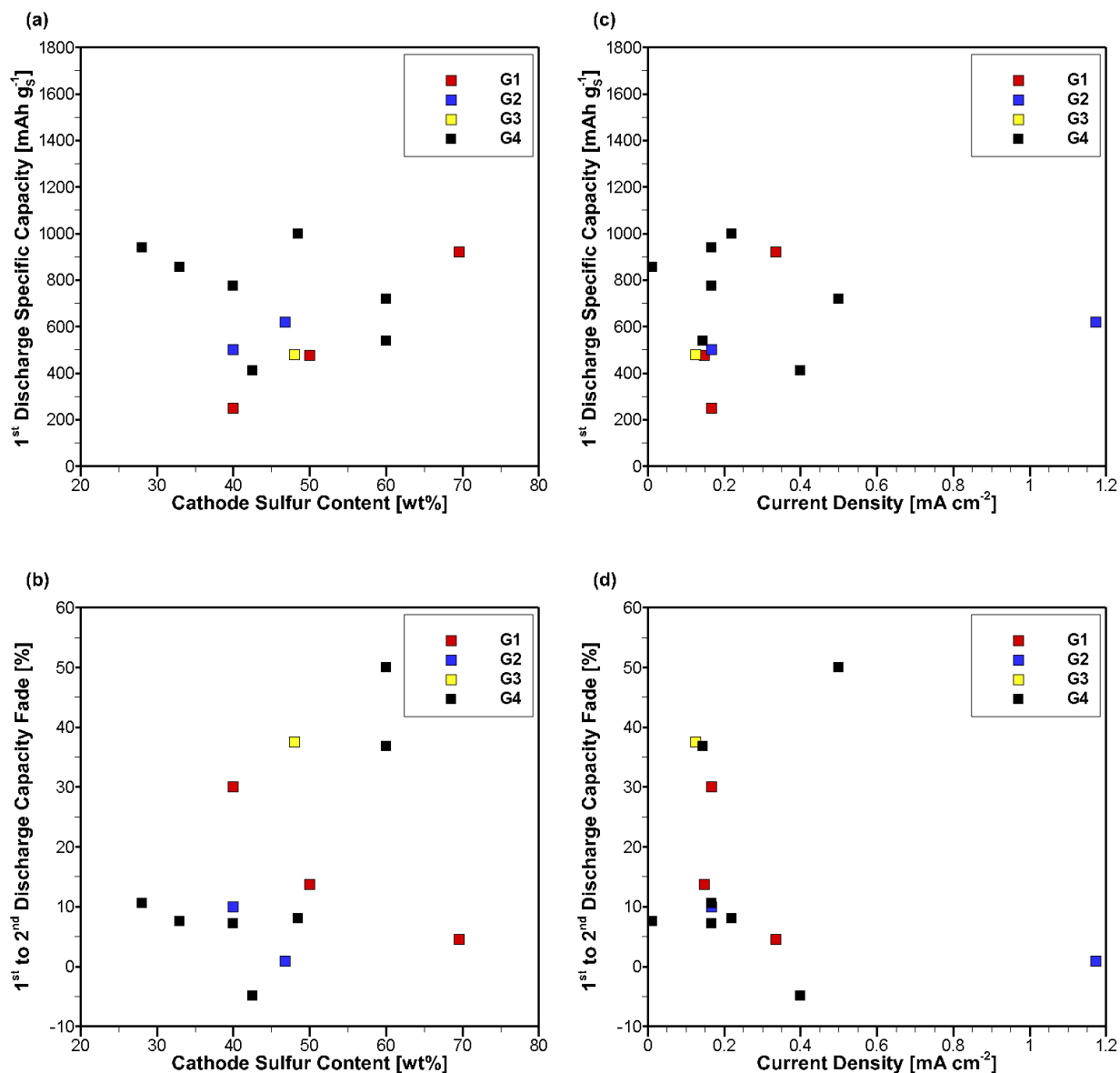
Figure 2.4. Aggregated cell performance data from 13 ether-based RT Na-S batteries from 12 references in the literature. The data shows the dependency of initial discharge specific capacity on **(a)** sulfur mass fraction and **(c)** current density as well as the dependency of initial capacity fade on **(b)** sulfur mass fraction and **(d)** current density. The data is organized by glyme solvent to show how glyme solvent selection influences performance. Data derived from references [107], [60], [114], [77], [102], [116], [74], [95], [100], [89], [59], and [110].

Figure 2.4 shows that across the range of cathode sulfur content and current density values, G4-based cells showed higher initial discharge specific capacity and lower initial capacity fading than the other types of ether-based cells. The cycling data for many cells in the literature was reported at C/10, or 0.167 mA cm^{-2} for a cell with a cathode areal loading of sulfur of 1.0 mg cm^{-}

51

[2]. Figure 2.4(c) shows the observed trend very clearly, because among all of the cells cycled at rates between 0.1 and 0.2 mA cm^{-2} (approximately C/10) the G4-based cells delivered superior initial discharge capacity. It also appears from Figure 2.4 that G2-based cells delivered slightly better initial discharge specific capacity and lower initial capacity fading than G1- or G3-based cells. J. He *et al.* [110] studied a cell with a very concentrated G1:NaFSI:TTE (1:1.2:1 ratio) electrolyte, and this cell is represented by the red square with an initial discharge specific capacity, initial capacity fade, sulfur content, and current density of 922, 4.6, 70, and 0.334, respectively. This cell broke the general trend and was among one of the best performing cells in Figure 2.4, likely owing to its concentrated electrolyte formulation. However, the majority of the cells in Figure 2.4 were G4-based. In contrast, G1-, G2-, and G3-based cells have less representation in the literature. Despite inferior performance, the unequal sample size shows that the other glymes require further research as electrolyte solvents in RT Na-S batteries.

2.2.6   *Summary of Literature Results on Electrolytes for RT Na-S Batteries*

Results from the literature indicate that informed selection and design of every electrolyte component (salt, solvent, and additive) are critical to optimize RT Na-S cell performance. In addition to affecting the ionic transport properties of the electrolyte, the salt plays an important role in dictating the composition of the SEI, which protects the anode and dictates stability of plating/stripping. Inorganic compounds, especially NaF and NaBr, are favored over organic compounds that are incorporated into the SEI as a result of solvent decomposition. Salt concentration may also play a role in stabilizing the Na anode and mitigating the polysulfide shuttle. In Chapter 2.2.5, it was shown that on average, carbonate-based electrolytes have higher initial discharge specific capacities as well as higher initial capacity fades than ether-based electrolytes. The solvent also plays a key role in dictating the redox pathway of the cell. In ether-based cells, discharge proceeds through two voltage plateaus near 2.2 V and 1.7 V. In some cell configurations, discharge occurs entirely through solid state reactions, with no dissolution or precipitation reactions. Solvents also alter redox pathways. In some solvents, like TMU, the $S_3^{\bullet-}$ radical is the dominant discharge product, while commonly used solvents like ethers and carbonates facilitate the formation of S_x^{2-} species as the dominant discharge products. Electrolyte additives have been shown to play a vital role in optimal cell performance. FEC, Na_2S_x, and $NaNO_3$ are used to create stable SEI layers on Na metal anodes, and FEC has also been used to create SEI on sulfur cathodes

that can prevent polysulfides from dissolving into the solvent. P_2S_5 and InI_3 have been shown to speed up the redox kinetics of insoluble short chain polysulfide conversion. Owing to the recent origin of RT Na-S research, there is not a consensus on the optimal system electrolyte, and the results on the merits of ethers and carbonates can be conflicting. Thus, more research on RT Na-S electrolytes is needed if RT Na-S batteries are to become a viable technology.

2.3   Objective

Based on the literature review, solvent properties affect polysulfide solvation and electrolyte evolution during cell operation; therefore, full cells with three different glyme-based electrolyte solvents (G1, G2, and G4) should show different performance due to differing degrees of polysulfide shuttle. Due to its high viscosity, G4-based full cells should show higher initial discharge capacities and slower capacity fading than G1- or G2-based full cells from slow diffusion of dissolved polysulfide species. Since these electrolytes differ only in solvent molecule chain length, and SEI composition has been shown to be dictated by salt, additive, and solvent composition, sodium plating and stripping performance at the anode should be equal for the three electrolytes. The objective of this work is to study how different glyme ether solvents (G1, G2, and G4) affect sodium stripping and plating at the anode as well as the conversion reactions at the cathode. Furthering the understanding of the electrochemical and chemical reactions and transport processes that occur in each electrolyte can help develop an optimized electrolyte for commercial RT Na-S batteries.

Inhomogeneous dendritic sodium plating can have grave consequences for a RT Na-S cell by contributing to capacity fading and cell failure. Thus, it is important to understand Na anode phenomena separately from the degradation mechanisms at work in the S cathode. To do this, Na/Na symmetric cells can be constructed with two sodium metal disks serving as the working electrode and counter/reference electrode, respectively. In Chapter 3, Na/Na symmetric cells with a 1M $NaPF_6$ in G1, G2, or G4 electrolyte are cycled galvanostatically at areal current densities of 0.5, 1.0, and 3.0 mA cm^{-2}. EIS was also used after cycling for a set number of cycles to analyze the SEI growth on the anode. It was found that stripping/plating performance is highly dependent on cycling rate. At low and moderate cycling rates, cells in the G4-based electrolyte showed moderately high overpotentials that remained constant over 100 cycles. At high cycling rates, the

G4-based cells immediately reached the upper safety voltage cutoff upon current application. At low current rates, the G1-based cells showed a high initial overpotential during the first cycle that stabilized to low overpotentials over 100 cycles. The G1-based cells showed some evidence of dendritic plating at low current density. At moderate and high cycling rates, the G1-based cells show unstable stripping and plating. The G2-based cells cycle with some instability at moderate and high rates at high cycle numbers, but overall show the most stable cycling with the lowest overpotentials across the range of current densities. Chapter 3.1 details the experimental procedures used to prepare the electrolytes, fabricate Na/Na symmetric coin cells, and perform the electrochemical tests. Chapter 3.2 provides results for the plating/stripping and EIS tests as well as an accompanying discussion.

In Chapter 4, S cathode performance in each electrolyte is analyzed in conjunction with Na anode performance in full RT Na-S cells. Galvanostatic cycling of RT Na-S coin cells with 1M $NaPF_6$ in G1, G2, or G4 electrolyte gives valuable insight into the effect of electrolyte on discharge capacity, capacity fading, and coulombic efficiency. RT Na-S cells with the G1-based electrolyte show superior initial discharge capacity on average; however, they show poor reversibility due to excessive polysulfide shuttle. In contrast, G4-based cells show poor initial discharge capacity compared to G1- and G2-based cells, but they are more reversible on average. The degree of polysulfide shuttle effect present in each cell type is determined by the charging behavior of the cell. The "infinite charging" behavior observed at different frequencies in each cell type is attributed to the polysulfide shuttle effect. Finally, the unique optical properties of each polysulfide species in solution are used to determine the polysulfide solubility and $S_3^{\bullet-}$ radical stability through *in-situ* optical microscopy [78]. The methods, results, and discussion of RT Na-S optical microscopy contained in Chapters 4.1.4 and 4.2.3 of this work were originally published in Rachel Carter, Addison NewRingeisen, **Daniel Reed**, Robert W. Atkinson III, Partha P. Mukherjee, and Corey T. Love, "Optical Microscopy Reveals the Ambient Sodium-Sulfur Discharge Mechanism," *ACS Sustainable Chemistry and Engineering*, 9(1), 92-100, 2021 (reference [78]). Chapter 4.1 details the methods of electrolyte preparation, cell fabrication, and electrochemical testing used in these experiments. Chapter 4.2 provides results from coin cell and optical cell experiments.

3. SODIUM PLATING AND STRIPPING IN GLYME ETHER ELECTROLYTES

3.1 Experimental Procedures

All electrolyte preparation and coin cell fabrication was conducted in an argon-fed glovebox (MBraun), which is shown below in Figure 3.1.
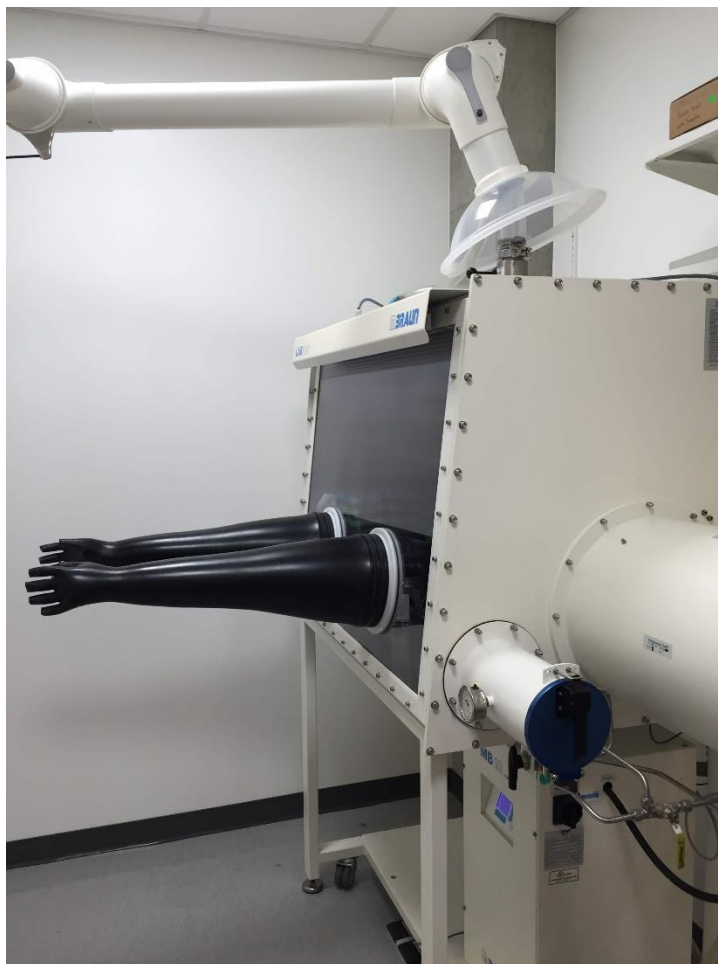
Figure 3.1. MBraun glovebox used to create inert atmosphere for ether-based electrolyte preparation and Na/Na symmetric cell fabrication.

The target O_2 and H_2O limits on the MBraun glovebox are both < 0.5 ppm, but the concentrations of both O_2 and H_2O occasionally rose beyond these limits while this work was being conducted. For example, on July 9th, 2020 and on November 13th, 2020, the glovebox O_2

concentration exceeded 10 ppm. Coin cell fabrication was avoided during these concentration spikes.

3.1.1 Electrolyte Preparation

1,2-dimethoxyethane (monoglyme/DME/G1), diethylene glycol dimethyl ether (diglyme/DEGDME/G2), tetraethylene glycol dimethyl ether (tetraglyme/TEGDME/G4), and sodium hexafluorophosphate (NaPF$_6$) were obtained from MilliporeSigma. The solvents had purities of at least 99%, and the salt had a purity of 98%. Prior to use, the solvents and salt were placed in the glovebox. To begin, 4Å molecular sieves were placed in a vacuum oven at 100°C for at least 24 hours, and an appropriate mass of NaPF$_6$ was added to a glass vial and heated on a hot plate at 50°C in the glove box for 24 hours. Next, dried sieves were evenly distributed among three glass vials, and each of G1, G2, and G4 were added to the respective vials. The dried sieves soaked in the solvents for at least 48 hours. 10 mL of each solvent was then pipetted into one of the glass vials containing dried salt. Since the molecular weight of NaPF$_6$ is 167.95 g mol^{-1}, a total of 1.6795 g of NaPF$_6$ was added to each vial before heating to create a 1M electrolyte with a volume of 10 mL. A magnetic stir bar was added to each electrolyte vial, and the electrolytes were stirred overnight before use. For the Na/Na symmetric cell tests at 0.5 mA cm^{-2} as well as the EIS tests, the solvents were not dried with sieves and the salt was not heated on the hot plate before use. However, using un-dried salts and solvents in the electrolytes of the cells cycled at low current densities did not appear to negatively impact cell performance.

3.1.2 Electrochemical Characterization

2032 coin cells were fabricated with one 5/8" diameter Na disk as the working electrode and another as the reference and counter electrode. In order to make the Na metal electrodes, cubes of Na metal stored in mineral oil (MilliporeSigma) were dried of oil using Kimtech Kimwipes. Next, the eight faces of the Na cube were cut off using a box cutter to expose fresh sodium. The dry, fresh Na cube was then placed in a small plastic sealable bag and rolled flat. A 5/8" diameter steel punch was used to create electrode disks. One electrode was pressed into the coin cell case, and the other was pressed onto a stainless steel spacer disk with a thickness of 0.5 mm. A 3/4" diameter ENTEK separator was placed atop the electrode in the coin cell case, and 80 µL of one

of the three electrolytes was pipetted onto the separator. The gasket was placed on top of the separator, and the spacer was placed electrode side down onto the separator. Finally, a wave spring was placed on top of the spacer followed by the coin cell cap, and the whole coin cell is crimped to seal it.

Stripping/plating tests were conducted using battery testers from either Arbin or Neware. Areal current densities of 0.5, 1.0, and 3.0 mA cm^{-2} were used for each electrolyte. Since the electrode diameter is 5/8", these current densities correspond to currents of 0.990 mA, 1.979 mA, and 5.938 mA, respectively. These current densities correspond to C-rates of 0.3C, 0.6C, and 1.8C, respectively in full RT Na-S cells, assuming that the sulfur loading in the cathode is 1 mg cm^{-2} and that 1C = 1672 mA g^{-1}. For all tests, the electrodes were stripped or plated to an areal capacity of 1 mAh cm^{-2}. This means that for the 0.5, 1.0, and 3.0 mA cm^{-2} current densities, the step cutoff time was 2 h, 1 h, and 20 min, respectively. After an initial 10 minute rest period, cells were charged at their selected current density up to 1 mAh cm^{-2}, and then discharged at the same current density to the same areal capacity after another 10 minute rest. This process was repeated for 100 cycles.

EIS measurements were conducted on a BioLogic potentiostat. The initial and final scanning frequencies were set as 1 MHz and 1 mHz, respectively. However, the first three data points showed large amounts of noise for every scan, and were omitted from the final results. Additionally, the scans were stopped around 15 mHz when the useful data had been recorded. After a rest period of 12 hours at the open circuit voltage, an initial EIS scan was performed on the cells. The cells were then cycled for 5 full plating/stripping cycles on a Neware battery tester at a current density of 0.5 mA cm^{-2} to an areal capacity of 1 mAh cm^{-2}, similar to the procedure described above. After a rest period of at least 2 hours, post-cycling EIS measurements were performed on the cells. This procedure was repeated two more times, with EIS measurements after the 10th and 15th cycles. Before cycles 6-10, the initial rest periods of the G2- and G4-based cells were changed to 20 minutes and 30 minutes, respectively, to account for the availability of only one channel on the BioLogic potentiostat. The G1-based cell initial rest was maintained at 10 minutes. After cycles 11-15, the cells were rested for an extended period of around 5 days.

3.2 Results and Discussion

Galvanostatic cycling of Na/Na symmetric cells was performed in different glyme ether electrolytes and at different current densities in order to investigate the sodium plating and stripping behavior in G1, G2, and G4. The standard cell potential of a Na/Na symmetric cell is 0 V, since Na metal is used as both the cathode and the anode. Any positive or negative voltage observed during cell charging and discharging, respectively, is an overpotential driven by practical cell phenomena like ionic transport resistance through the liquid electrolyte or SEI. Thus, the different overpotential values observed during the electrochemical operation of G1-, G2-, and G4-based cells at a given current density are good indicators of how the different solvents affect cell performance.

3.2.1 Cycling at Low Rates and Electrochemical Impedance Spectroscopy Analysis

The Na plating and stripping results for Na/Na symmetric cells in G1-, G2-, and G4-based electrolytes cycled at the low current density of 0.5 mA cm^{-2} are given below in Figure 3.2. Figure 3.2(a) shows the voltage profiles of the cells for the full 100 cycles, and Figure 3.2(b) provides an enhanced view of the first 5 cycles of the same tests.
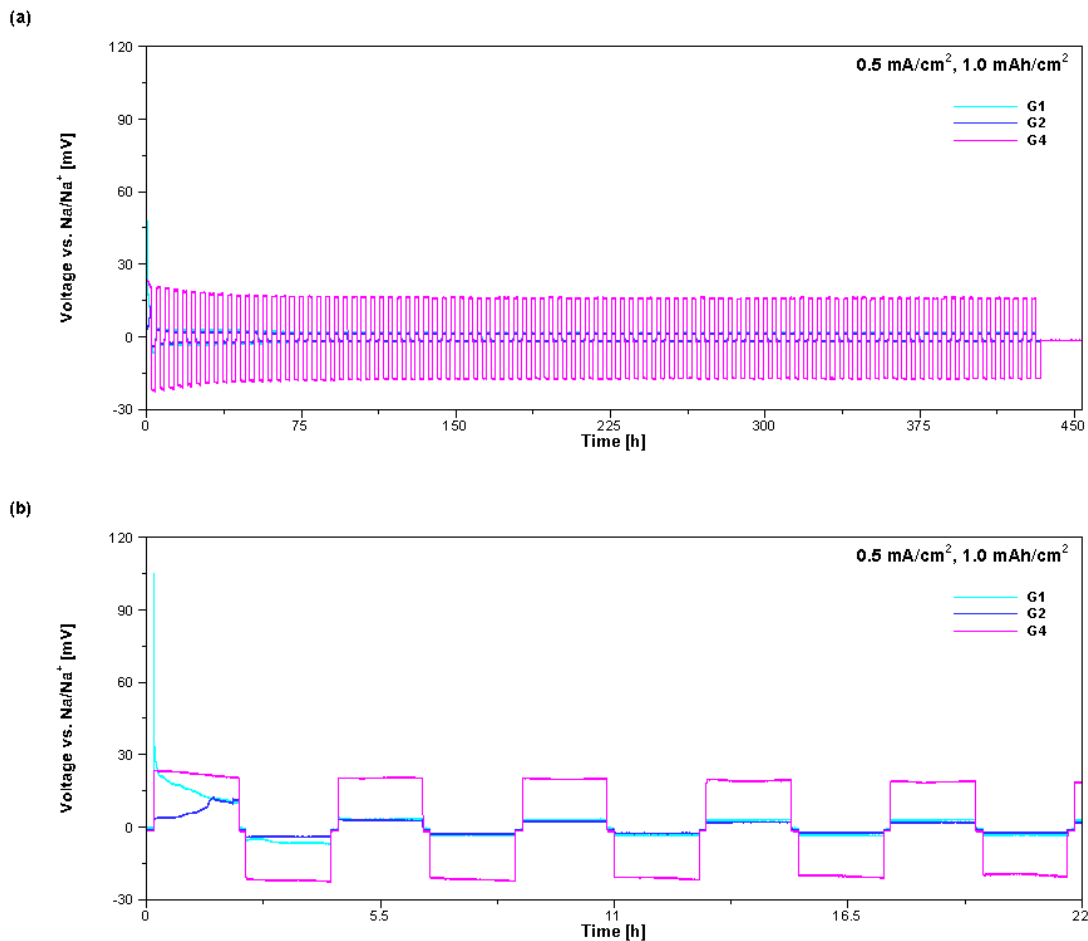
Figure 3.2. Na/Na symmetric cells in 1M NaPF$_6$ in G1, G2, and G4 electrolytes cycled at a current density of 0.5 mA cm^{-2} to an areal capacity of 1.0 mAh cm^{-2} (step time of 2 hours) for **(a)** 100 cycles and **(b)** the first 5 cycles.

Figure 3.2 shows a clear distinction between the overpotentials produced by the different electrolytes, as well as the effect of cycle number on overpotential for a given electrolyte. Figure 3.2 also shows that all three electrolytes enable stable cycling without shorting or failure for the full 100 cycles. As seen clearly in Figure 3.2(b), the G1-based cell experiences a high initial overpotential of 105 mV during the first plating/stripping cycle that quickly drops. At the start of the second cycle, the cell reaches a maximum overpotential of 3.1 mV. By the start of the 100th cycle, the maximum overpotential becomes 1.4 mV. The large initial overpotential observed during the first cycle for the G1-based cell is likely due to a thick SEI layer that forms spontaneously when the Na electrodes contact the G1 solvent and NaPF$_6$ salt. After the initial plating/stripping half cycle, the resistance of the SEI layer drops dramatically and enables stable

cycling at low, slowly decreasing overpotentials between cycles 2 and 100. The G2-based cells shows different behavior at 0.5 mA cm^{-2}, especially in the first cycle. In the first plating/stripping cycle, the overpotential of the G2-based cell gradually increases to a maximum value and then remains relatively constant until the areal capacity is attained. After the initial cycle, this cell cycles stably at low overpotentials for 100 cycles. In the first cycle, the G2-based cell attains a maximum overpotential of 12.2 mV. During cycles 2 and 100, the maximum overpotentials are 3.1 mV and 1.5 mV, respectively. The overpotentials observed in the G4-based cells are the highest among the three electrolytes between cycles 2 and 100, but stable cycling is observed throughout. In the first cycle, the maximum overpotential attained in the G4-based cell is 23 mV. The maximum overpotentials during the 2nd and 100th cycles are 20 mV and 16 mV, respectively. EIS measurements of these cells at different points during cycling can provide greater insight into the cell performance observed in Figure 3.2. The open circuit voltages of Na/Na symmetric cells with 1M NaPF$_6$ in either G1, G2, or G4 electrolyte over a 12 hour span as well as the EIS scans of these cells after the rest period are shown below in Figure 3.3.
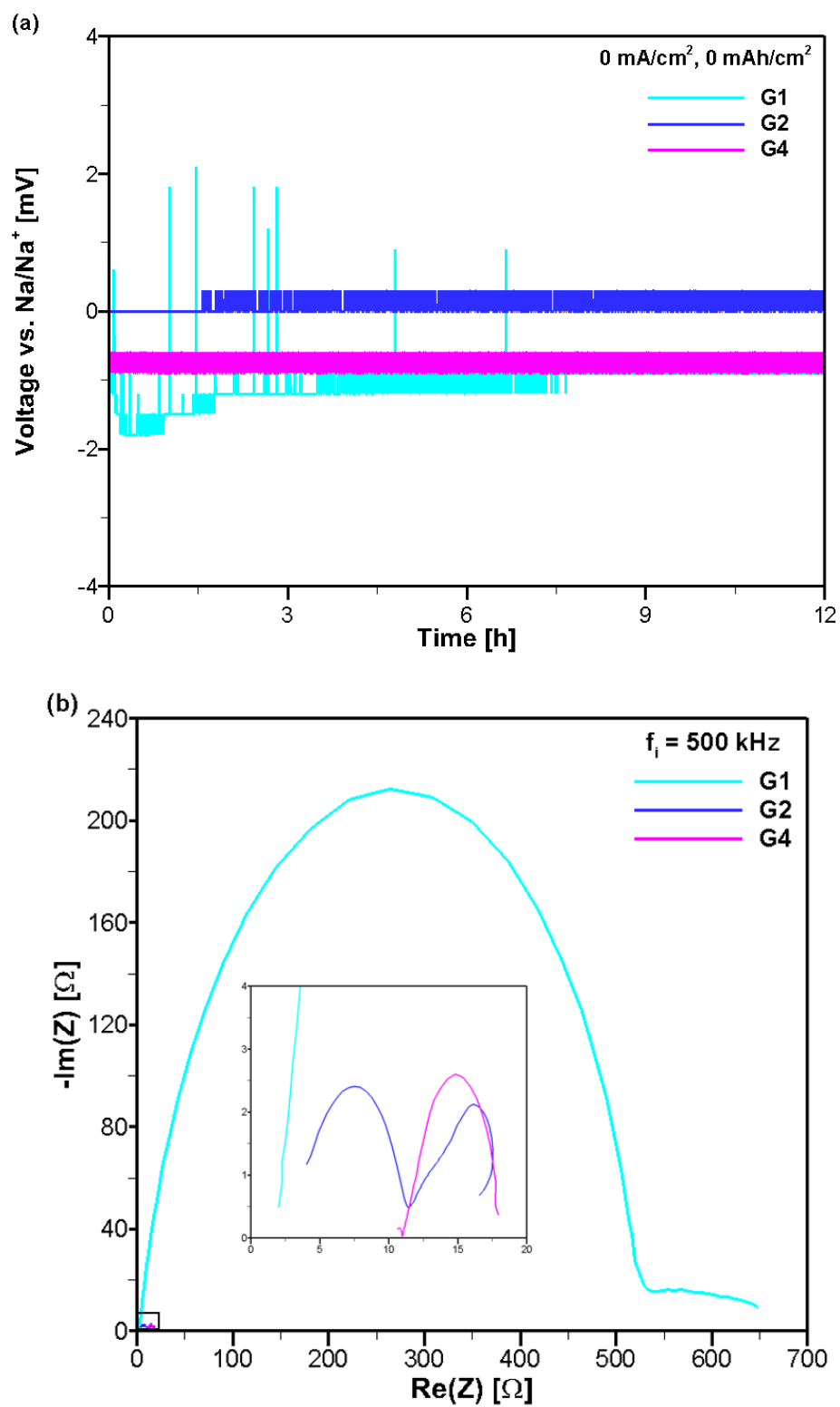
Figure 3.3. (a) Na/Na symmetric cells in 1M NaPF₆ in G1, G2, and G4 electrolytes rested at the open circuit voltage for 12 hours and **(b)** EIS scans of these cells after the rest period.

Figure 3.3(a) shows the open circuit voltages of the three cells. The G1-based cell shows some instability during the 12 hour rest period, but the open circuit voltage eventually reaches a constant value of greater than -1 mV at around the 8 hour mark. Figure 3.3(b) shows the EIS measurements of the three cells after the 12 hour rest period. In the EIS measurements, the frequency decreases from left to right along each curve. Each EIS curve consists of an intercept on the x-axis (which may have to be extrapolated) and two semi-circles. The physical interpretation of the x-axis intercept is the electrolyte resistance of the cell, while the high frequency (left-most) semi-circle represents passivation layer (SEI) resistance and the low frequency (right-most) semi-circle represents charge transfer resistance, respectively [59]. The most striking feature of Figure 3.3(b) is the size of the high frequency semi-circle of the G1 cell curve relative to those of the G2 and G4 curves, which are so comparatively small that they are shown in the figure inset. This indicates that after being exposed to the G1-based electrolyte for 12 hours with no applied current, the SEI formed on the Na electrode surfaces are very thick and resistive compared to those formed in the G2- and G4-based cells. Moreover, the SEI resistance of the G2-based cell appears larger than that of the G4-based cell before cycling. The electrolyte resistances of the three cells also appear to differ. When extrapolated to the real axis, the G4-based cell has the largest electrolyte resistance, and the G1-based cell has the lowest. This is due to the differing ionic conductivities of the electrolytes; ionic conductivity is highest for the G1 electrolyte and lowest for the G4 electrolyte [88]. Cycling changes these EIS results dramatically. Figure 3.4 shows the voltage profiles of the same three cells cycled 5 times at 0.5 mA cm^{-2} as well as the EIS measurements taken after the 5 cycles.

(a) 0.5 mA/cm², 1.0 mAh/cm²

G1
G2
G4

(b) f_i = 500 kHz

G1
G2
G4
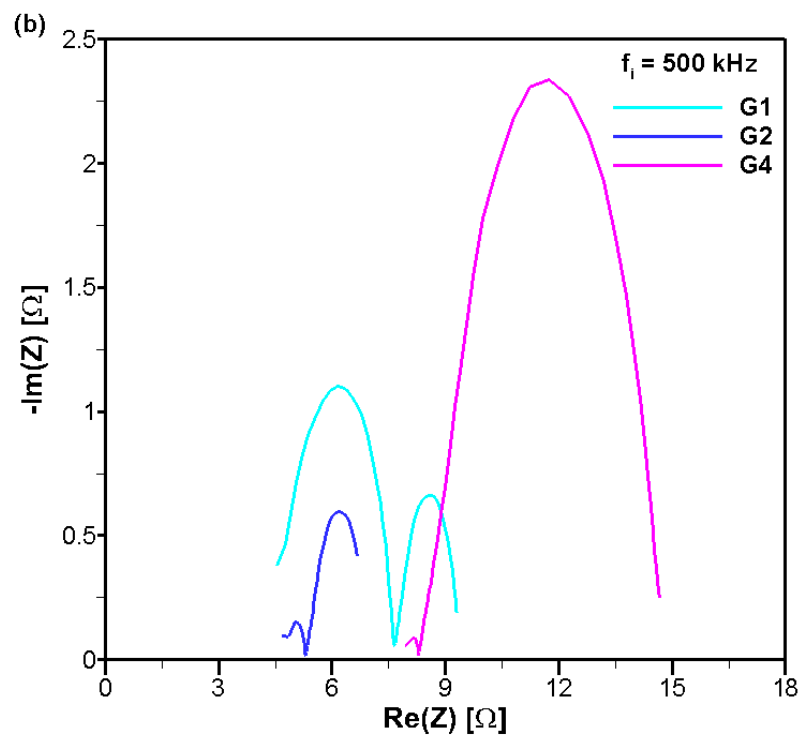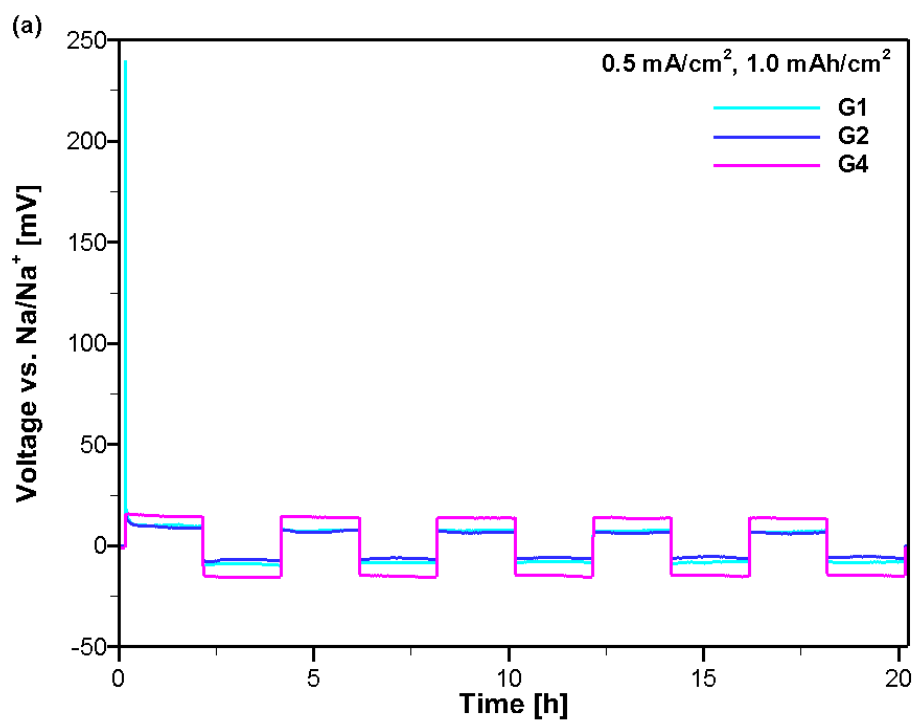
Figure 3.4. (a) Cycles 1-5 of G1-, G2-, and G4-based Na/Na symmetric cells and **(b)** EIS scans after the 5th cycle.

The voltage profiles in Figure 3.4(a) show nearly the same qualitative trend as those in Figure 3.2(b). The G1-based cell shows a large overpotential of nearly 250 mV in the first half cycle which then drop to low, steady levels on subsequent cycling. In Figure 3.4(a), the G2-based cell shows an exponential decay pattern during the first cycle that is not seen in Figure 3.2(b), and the overpotentials remain low and steady throughout the full 5 cycles. With the exception of the first half cycle of the G1-based cell, the G4-based cell shows higher overpotentials than both the G1- and G2-based cells, just as in Figure 3.2. Figure 3.4(b) demonstrates that cycling even for just 5 cycles changes the internal resistances of the cells. The most striking observation is the dramatic decrease in both the passivation layer and charge transfer resistances of the G1-based cell. Along with the stripping/plating results of the G1-based cell, these EIS results indicate that the initial thick and resistive SEI layer on the electrodes is replaced by a thinner, less resistive SEI layer that forms on freshly deposited Na metal with a higher surface area than the original electrode surface. Thus, the SEI formed through initial electrochemical operation in the G1-based cell is superior to the one that forms upon contact with the electrolyte in spontaneous chemical processes. This change is visible to a lesser degree in the G2-based cell, as its passivation layer resistance also decreased after the first 5 cycles. In contrast, the EIS curves of the G4-based cell from before cycling and after 5 cycles show almost no changes. Additionally, the electrolyte resistances for all three cells are approximately the same. Figure 3.5 displays the voltage profiles for cycles 6-10 of these same three cells as well as the EIS measurements after cycle 10.
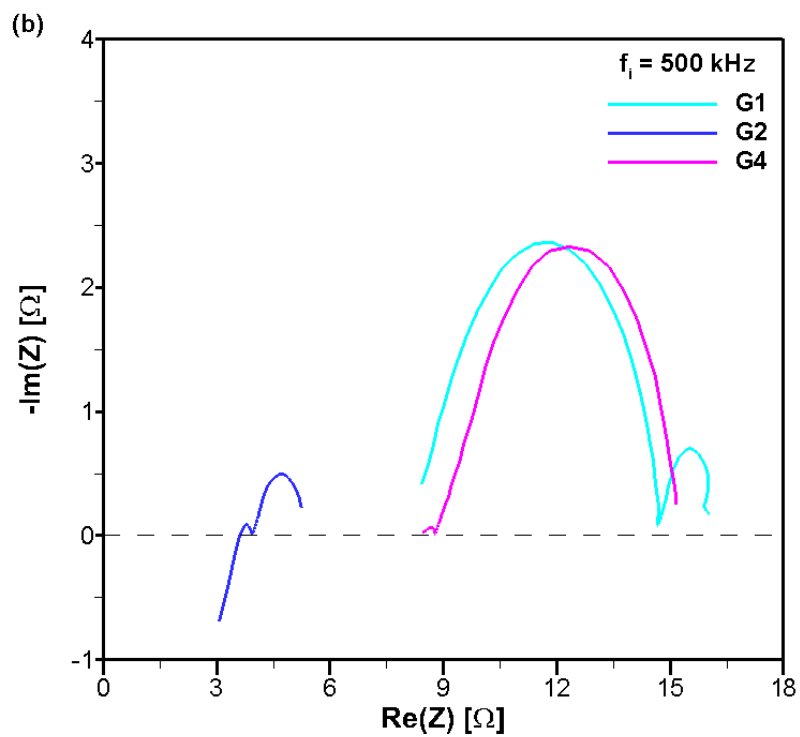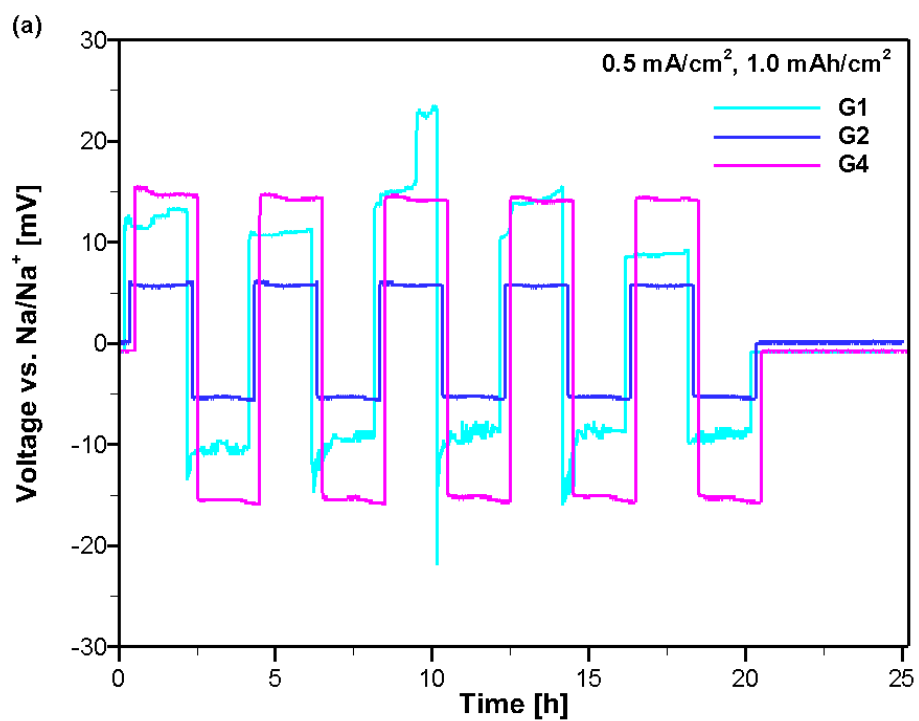
Figure 3.5. (a) Cycles 6-10 of G1-, G2-, and G4-based Na/Na symmetric cells and **(b)** EIS scans after the 10th cycle.

In Figure 3.5(a), the G2- and G4-based cells continue to cycle in a stable manner as in the first 5 cycles. However, the G1-based cell begins to exhibit an unstable voltage profile, especially in the 8th cycle. This is corroborated by the EIS results in Figure 3.5(b). The EIS curves of the G2- and G4-based cells change very little between the 5th and 10th cycle. However, the real axis intercept and the radius of the high frequency semi-circle have increased for the G1-based cell. This trend reveals that there are two interconnected processes at work in the G1-based cell. The increase in the real axis intercept indicates that the electrolyte resistance has increased, while the increase in the high frequency semi-circle indicates SEI growth. It can be inferred that the stable SEI layer in the G1-based cell formed in the first 5 cycles began to crack possibly due to inhomogeneous and dendritic plating, exposing fresh Na to the electrolyte. The electrolyte then reacts irreversibly with the exposed Na, which both consumes some of the electrolyte and builds a thicker SEI layer. This cell degradation mode has not appeared in any of the G2- or G4-based cells. Figure 3.6 shows the voltage profiles during cycles 11-15 for these three cells as well as the corresponding EIS measurements after the 15th cycle.

Figure 3.6. (a) Cycles 11-15 of G1-, G2-, and G4-based Na/Na symmetric cells and **(b)** EIS scans after the 15th cycle.
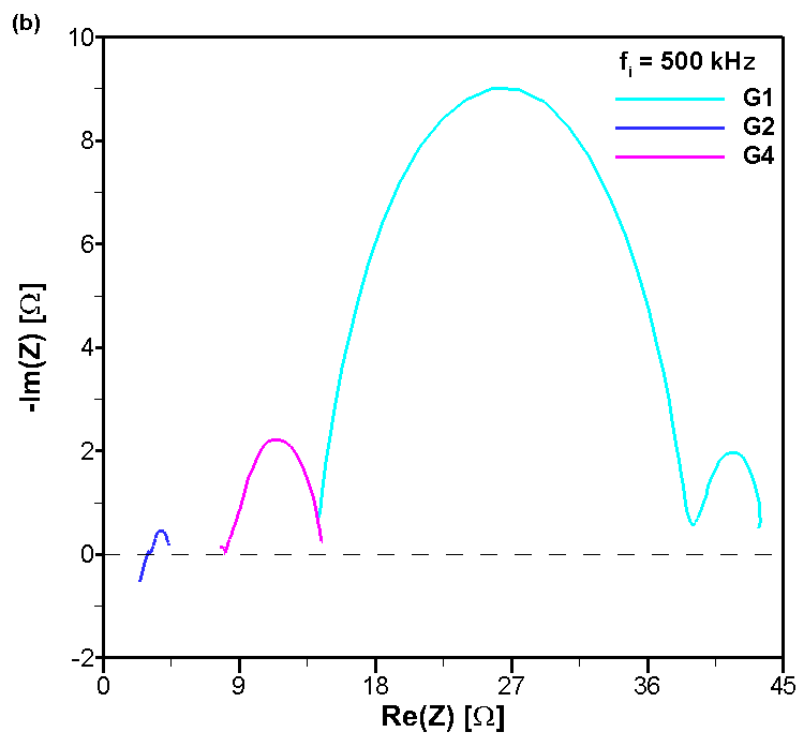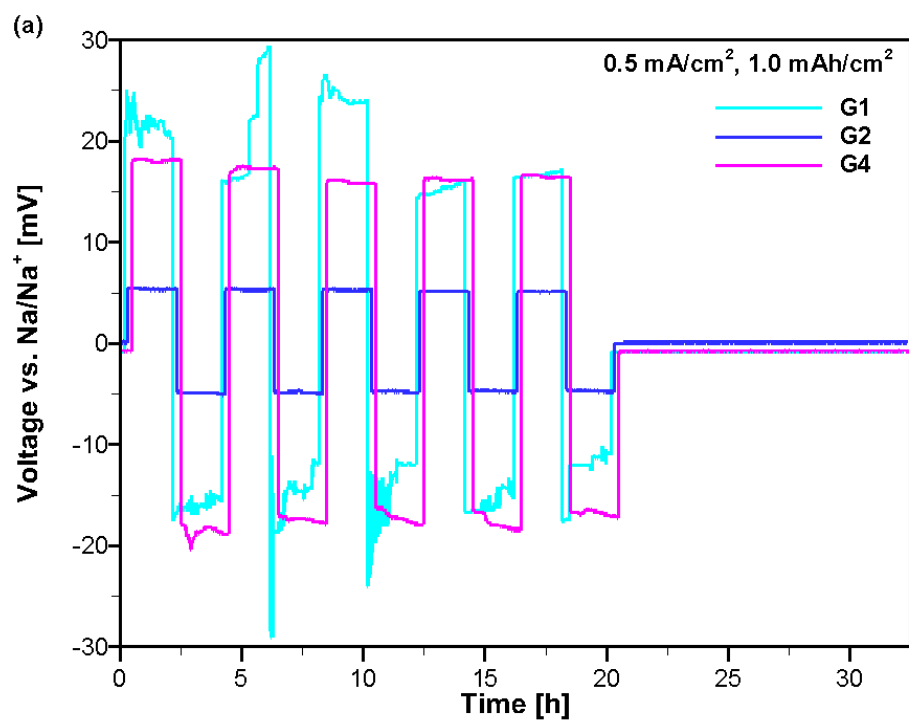
Figure 3.6(a) shows that the unstable cycling in the G1-based cell has persisted after the 10th cycle, while the G2- and G4-based cells continue to cycle in a stable manner. EIS measurements in Figure 3.6(b) of the three cells confirms that the degradation in the G1-based cell has continued further. The EIS curves of the G2- and G4-based cells taken after the 15th cycle again changed very little compared to their respective scans after the 10th cycle. In contrast, both the electrolyte resistance and the passivation layer resistance of the G1-based cell increased compared to the 10th cycle scans. This indicates that dendritic plating has continued in the cell, which leads to more SEI growth and electrolyte consumption. Although there was an extended rest period between the end of the 15th cycle and the EIS scans, it is unlikely that chemical SEI growth contributed significantly to the resistance increases in the G1-based cell. There was no extended rest between the previous EIS scan and cycles 11-15, so the dominant contributor to resistance growth in the G1-based cell is dendritic plating. While no evidence of dendritic plating or stripping was seen in the G1-based cell in Figure 3.2, these results suggest that unstable stripping and plating is more likely in G1-based cells than in G2- or G4-based cells.

3.2.2 Moderate and High Rate Cycling

In the results presented above, all of the cycling was carried out at a low current density of 0.5 mA cm^{-2}. As stated in Chapter 3.2, this is equivalent to a C-rate of 0.3C in a full RT Na-S cell assuming that the areal mass loading of sulfur in the cathode is 1 mg cm^{-2} and that 1C is equivalent to 1672 mA g^{-1}. However, RT Na-S cells will be exposed to higher cycling rates in practical applications. Therefore, it is also important to understand Na plating and stripping dynamics in the three different electrolytes at moderate and high current densities. Figure 3.7 provides results for plating/stripping tests in Na/Na symmetric cells with 1M NaPF$_6$ in G1, G2, and G4 electrolytes at a moderate current density of 1 mA cm^{-2}. A current density of 1 mA cm^{-2} is equivalent to a C-rate of 0.6C in a full RT Na-S cell, assuming that the mass loading of sulfur in the cathode is 1 mg cm^{-2} and that 1C is equivalent to 1672 mA g^{-1}.
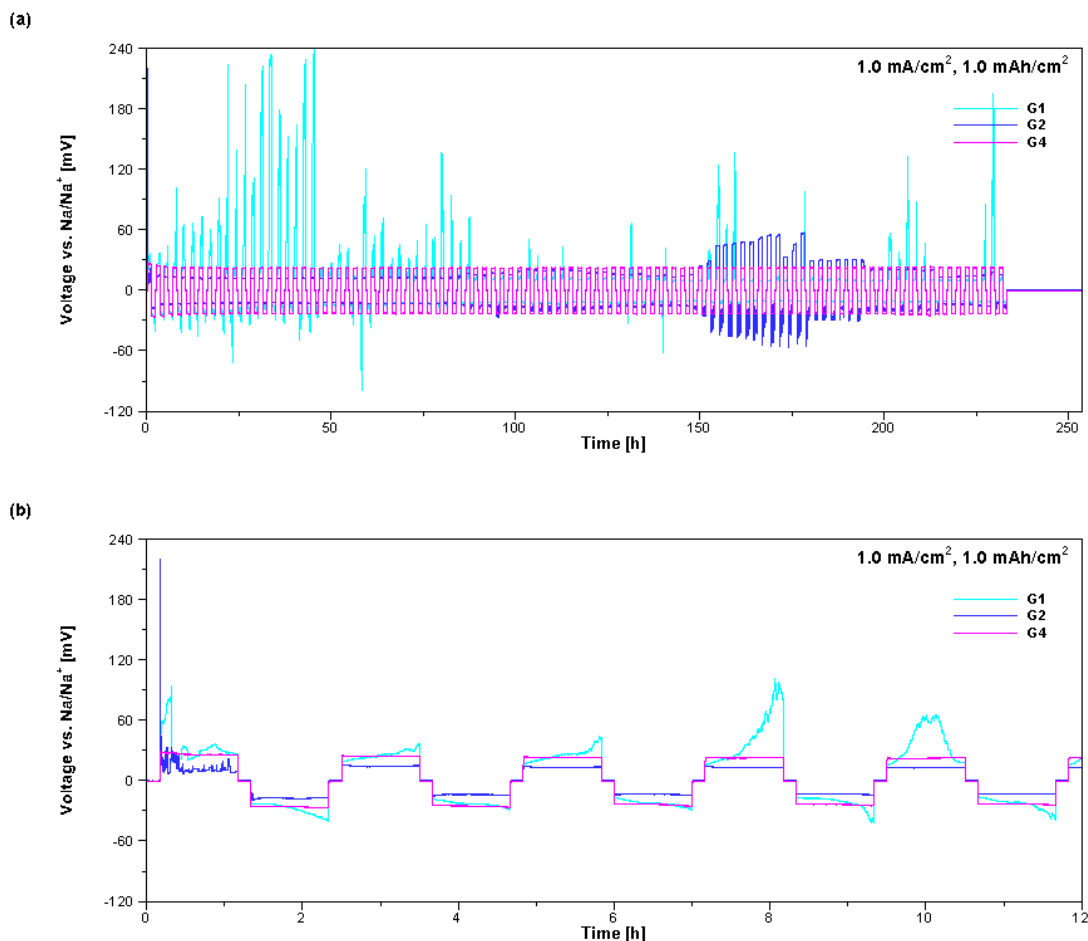
Figure 3.7. Na/Na symmetric cells in 1M NaPF$_6$ in G1, G2, and G4 electrolytes cycled at a current density of 1.0 mA cm^{-2} to an areal capacity of 1.0 mAh cm^{-2} (step time of 1 hour) for **(a)** 100 cycles and **(b)** the first 5 cycles.

Figure 3.7(a) gives the voltage profiles for the G1-, G2-, and G4-based cells for the full 100 cycles of testing, while Figure 3.7(b) provides an enhanced view of the voltage profiles within the first 5 cycles. All of the cells were able to cycle for the full 100 cycles without shorting or failure. However, the G1-based cell exhibited an unstable voltage profile for the duration of the 100 cycle test. The unstable voltage profiles are characterized by very large overpotentials (reaching nearly 240 mV in the first half of the test) with noisy patterns that have little consistency between cycles. This is likely due to inhomogeneous stripping and plating in the G1-based cell. Figure 3.7(b) illustrates the noisy, inconsistent voltage profile of the G1-based cell in closer detail. Interestingly, the large overpotentials in the G1-based cell occur primarily during cell "charge". This could be due to a higher degree of dendritic growth on the Na electrode serving as the "anode".

69

During cycling at low current density, the G2-based cell exhibited low overpotentials over the duration of the 100 cycle test. At moderate current density, the G2-based cell now experiences a large overpotential of 221 mV during the first half cycle. The overpotentials dropped substantially upon further cycling, and the cell cycled in a stable manner at low overpotentials for the remainder of the 100 cycles. During the second cycle, the G2-based cell attains a maximum overpotential of 16 mV. During the 100th cycle, the maximum overpotential is maintained at 16 mV. The drop in overpotentials between the first half cycle and second half cycle is attributed to the thin SEI layer formed on freshly deposited, higher surface area Na metal during the initial plating phase. In contrast with the G1-based cell, the overpotentials of the G2-based cell cycled at 1 mA cm^{-2} are symmetrical about 0 V. Just after 150 hours of cycling, the overpotentials of the G2-based cycle increase, but decrease to previous levels after around 20 cycles. Just as in the 0.5 mA cm^{-2} case, the G4-based cell cycled at 1 mA cm^{-2} did not exhibit an exceptionally large overpotential during the first half cycle. Instead, this cell cycled at overpotentials slightly larger than those of the G2-based cell for the duration of the test, just as in the 0.5 mA cm^{-2} case. Specifically, the G4-based cell attained a maximum overpotential of 29 mV during the first cycle, 25 mV during the second cycle, and 23 mV during the 100th cycle. In the EIS measurements of the G4-based cell in Figures 3.3-3.6, the G4-based cell appeared to have a smaller passivation layer resistance but larger electrolyte and charge transfer resistances than the G2-based cell. Therefore, the higher overpotentials observed in the G4-based cell could be due to the lower ionic conductivity and higher viscosity of the G4-based electrolyte. Na/Na symmetric cells with 1M $NaPF_6$ in G1, G2, and G4 electrolytes were also tested at a high current density of 3 mA cm^{-2}. This current density is equivalent to a C-rate of 1.8C in a full RT Na-S cell if the assumptions listed above are maintained. These results are shown in Figures 3.8 and 3.9.
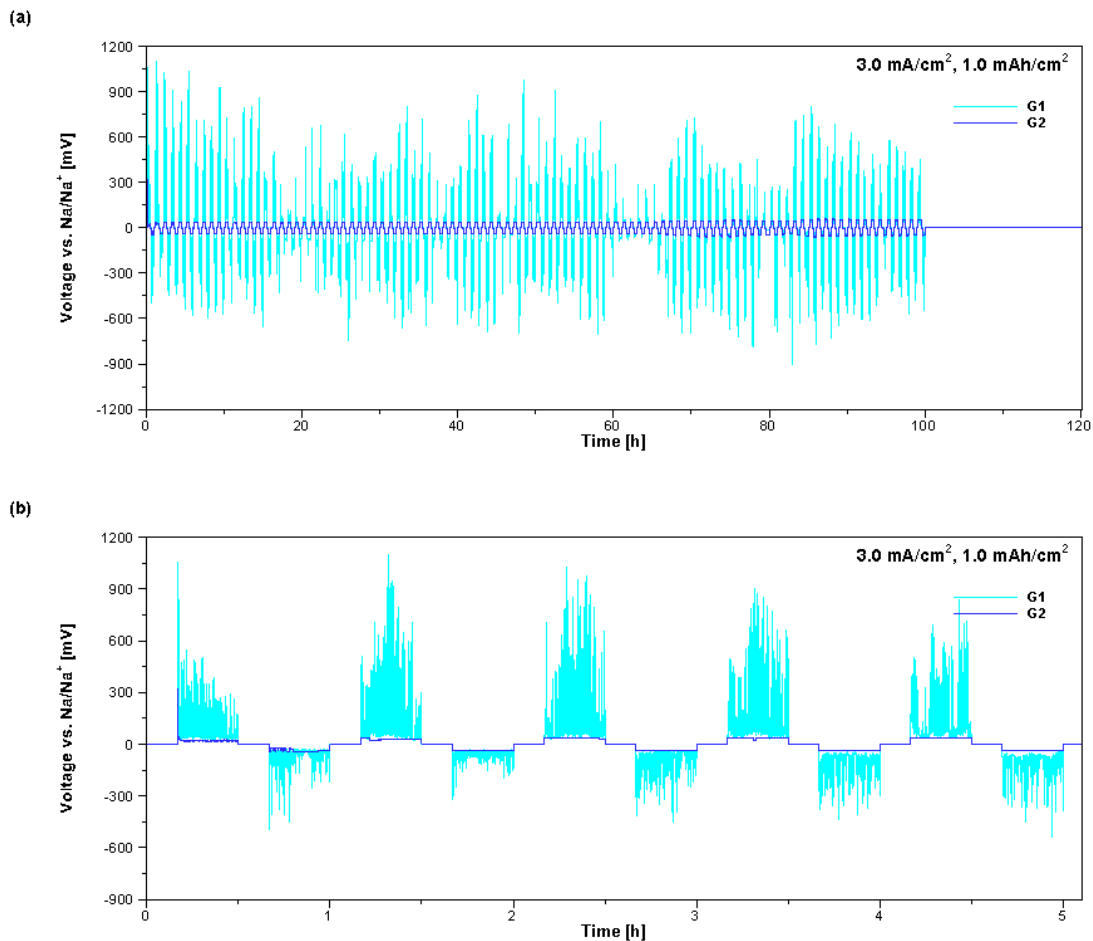
Figure 3.8. Na/Na symmetric cells in 1M NaPF$_6$ in G1 and G2 electrolytes cycled at a current density of 3.0 mA cm^{-2} to an areal capacity of 1.0 mAh cm^{-2} (step time of 20 minutes) for **(a)** 100 cycles and **(b)** the first 5 cycles.

At 3 mA cm^{-2}, only the G1- and G2-based cells could be cycled for the full 100 cycles. The G4-based cell fails immediately, and those results are shown in Figure 3.9. As shown in Figure 3.8, the voltage profile of the G1-based cell cycled at 3 mA cm^{-2} exhibits very large overpotentials coupled with noise and inconsistency. This can be seen in detail in Figure 3.8(b). Unlike in the 1 mA cm^{-2} cycling case, these overpotential magnitudes are roughly symmetric about 0 V. These results indicate that there is significant dendritic plating in the G1-based cell. In contrast, the G2-based cell exhibits a stable voltage profile with relatively low overpotentials for the duration of the 100 cycles, with the exception of the first half cycle. Here, the G2-based cell experiences a large maximum overpotential of 322 mV. The maximum overpotentials of the second and 100th cycles are 39 mV and 52 mV, respectively. This gradual overpotential growth between cycles 2

71

and 100 that can be seen in Figure 3.8(b) indicate that there might be some dendritic Na deposition and SEI growth in the G2-based cell cycled at high current densities. As dictated by Ohm's law, an increase in overpotentials for a cell with a given electrolyte is expected as the current densities increases. The impact of high current densities on the G4-based cell is shown below in Figure 3.9.
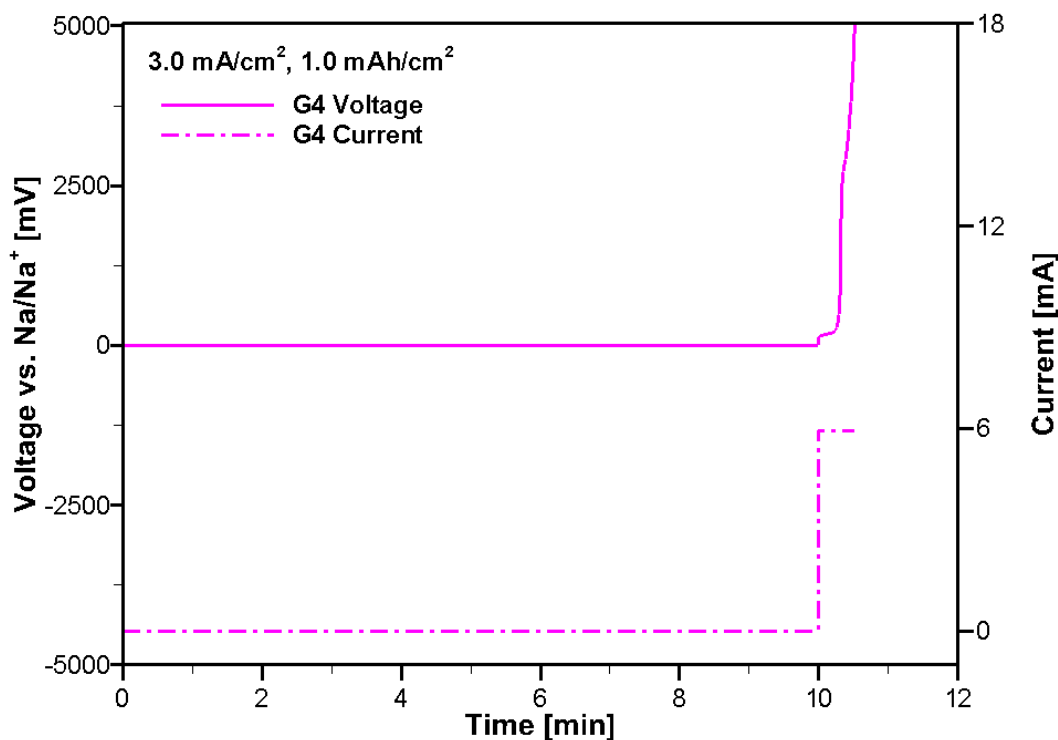
Figure 3.9. Na/Na symmetric cell in 1M NaPF$_6$ in G4 electrolyte cycled at a current density of 3.0 mA cm^{-2} to an areal capacity of 1.0 mAh cm^{-2} (step time of 20 minutes). The voltage immediately reaches the upper safety voltage cutoff of 5 V, stopping the test.

In less than a minute after applying a 3 mA cm^{-2} current density (5.938 mA for this electrode size) to the G4-based cell, the cell voltage rapidly increases to 5 V, terminating the test. In previous tests at low and moderate current density, the G4-based cells showed higher overpotentials than the G2-based cells, except during the first half cycle. This was attributed to higher electrolyte resistance in the G4-based cells caused by the higher viscosity and lower ionic conductivity of the G4 electrolyte. When cycled at high current densities, ionic transport along concentration and voltage gradients becomes kinetically hindered in the electrolyte, and results in

a rapid rise in voltage. Therefore, G4-based electrolytes are not a suitable choice for high rate applications.

4. CELL PERFORMANCE AND REDOX MECHANISMS OF FULL ROOM-TEMPERATURE SODIUM-SULFUR CELLS IN GLYME ETHER ELECTROLYTES

4.1 Experimental Procedures

As with the Na/Na symmetric cell fabrication, all electrolyte preparation and RT Na-S coin or optical cell fabrication took place in an argon glovebox. In this case, water and oxygen levels were both kept below 0.5 ppm.

4.1.1 Electrolyte Preparation

The electrolyte preparation method used for electrolytes in full RT Na-S cells is similar to that detailed in Chapter 3.2.1. Here, 4Å molecular sieves dispersed among three glass vials as well as an appropriate amount of $NaPF_6$ for 1M electrolytes in each of three glass vials were heated at 100°C under vacuum for 25 hours in an MTI vacuum oven. For 10 mL electrolyte solutions, 1.679 g of $NaPF_6$ were placed in each vial. Next, the six vials were taken to the glovebox, where one of the G1, G2, and G4 solvents were added to each vial filled with sieves. The three solvents were dried with the sieves for at least 48 hours. Next, 10 mL of each dried solvent was added to a different salt-containing glass vial and stirred overnight using magnetic stir bars and a magnetic stir plate. This process produced 10 mL of each of 1M $NaPF_6$ in G1, 1M $NaPF_6$ in G2, and 1M $NaPF_6$ in G4 electrolytes.

4.1.2 Cathode Preparation

The cathode active material used in RT Na-S full coin cells was a S/multi-walled carbon nanotube (MWCNT) composite comprised of 60 wt% S and 40 wt% MWCNTs. This active material was prepared by melt infiltration of S (Sigma-Aldrich, purified) into the MWCNTs (8-15 nm) at 155°C under vacuum in a sealed ampule for 12 hours [78]. An electrode slurry was prepared by combining and mixing the $S_{60}MWCNT_{40}$ active material with carbon black (CB) (TIMCAL C-NERGY SUPER C65) conductive additive and sodium carboxymethylcellulose (NaCMC) (Sigma-Aldrich, average molecular weight) binder in a 70:20:10 mass ratio. Thus, the total sulfur mass content of the cathode is 42%. The NaCMC binder was dissolved in distilled H_2O at a

concentration of 10 mg mL^{-1}. The slurry was prepared by first manually grinding the active material and carbon black together in a mortar and pestle and then mechanically mixing and grinding the active material and carbon black together with glass balls in an automatic mixer (FlackTek SpeedMixer). Next, the appropriate amount of the NaCMC/H$_2$O binder solution was added to the mixed and ground powder, and the full slurry was again ground and mixed manually in a mortar and pestle and then mechanically in the FlackTek mixer. The slurry was spread onto an aluminum current collector with a target areal capacity loading of 2 mAh cm^{-2}. The electrode material was then placed in the MTI vacuum oven and dried at 60°C under vacuum for 24 hours. Dried electrode surfaces were characterized using a Hitachi S-4800 SEM. SEM images of the dried electrode sheet are given below in Figure 4.1.
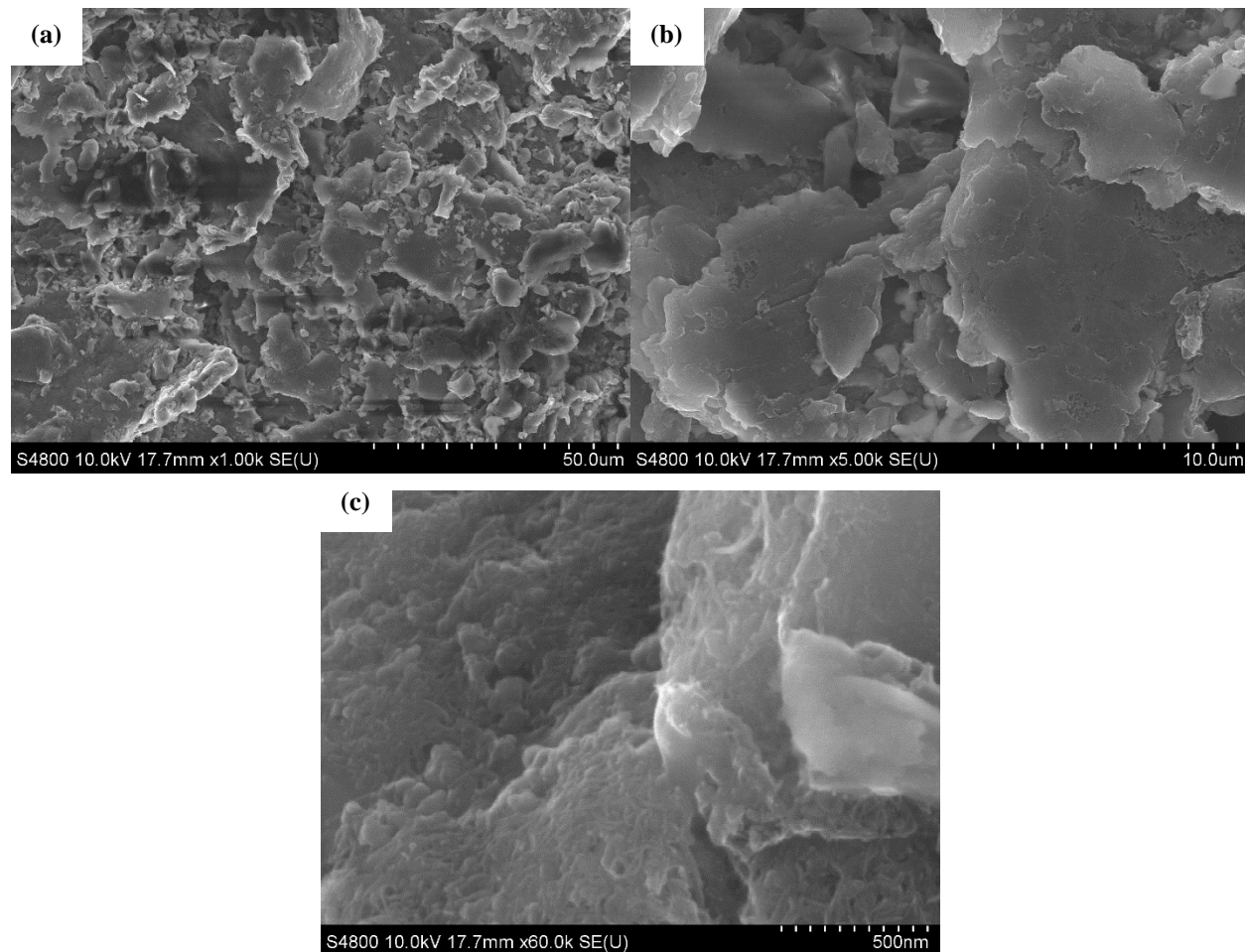
Figure 4.1. SEM images of dried S$_{60}$MWCNT$_{40}$:CB:NaCMC cathode material at **(a)** 1x, **(b)** 5x, and **(c)** 60x magnification.

Figure 4.1 shows that the microstructure of the S cathode is not smooth and is composed of many agglomerated particles. The microstructure is also porous with high surface area, which increases the electrode-electrolyte interface area.

4.1.3   Electrochemical Characterization

Cell performance was evaluated in 2032 coin cells. Na anodes were prepared in a similar manner as in Chapter 3.2.2, with slight modifications. First, Na cubes (Sigma-Aldrich stored in mineral oil) were rinsed in the specific electrolyte solvent to remove any excess oil and dried with Kimtech Kimwipes. Next, the eight exposed faces of the Na cube were cut off using a sharp boxcutter, and the fresh Na cube was placed in a small plastic bag and rolled out into a flat sheet using a steel cylindrical punch. The punch was then used to create 5/8" diameter Na anode discs, which were pressed into the coin cell case. Finally, the anodes were gently brushed with a toothbrush to further expose fresh Na. The cell separators were 3/4" diameter GE Whatman GF-C discs. Prior to use, separators were dried at 40°C under vacuum in a MTI vacuum oven for over 12 hours. The separator discs were placed on top of the Na anode in the coin cell case, and 80 μL of one of the electrolytes was pipetted onto the separator. Next, a gasket was placed on top of the separator to seal the cell. 5/8" cathode discs were punched from the sheets prepared according to the method in Chapter 4.2.2. The cathode discs had S mass loadings of 1.3 to 2.5 mg cm^{-2}. Next, a 0.5 mm thick stainless steel spacer disc was added, followed by a wave spring and coin cell cap. Cells were crimped to fully seal them. Galvanostatic cycling was carried out using a Neware battery tester, with upper and lower cutoff voltages of 2.6 and 0.8 V, respectively. One G2-based cell was discharged to 0.5 V, but results below the 0.8 V cutoff were not used for average initial specific discharge capacity calculations. Cycling was done at a rate of C/10, where 1C = 1.675 A g^{-1}. Cells were initially subjected to a 1 minute rest period, followed by a constant current (CC) discharge. After the discharge, cells were subjected to another 1 minute rest followed by a CC charge. This process was repeated for each cell until failure.

4.1.4   Optical Microscopy

Procedures for the construction and *in-situ* testing of RT Na-S optical cells were first published in Rachel Carter, Addison NewRingeisen, **Daniel Reed**, Robert W. Atkinson III, Partha

P. Mukherjee, and Corey T. Love, "Optical Microscopy Reveals the Ambient Sodium-Sulfur Discharge Mechanism," *ACS Sustainable Chemistry and Engineering*, 9(1), 92-100, 2021 (reference [78]). Cathode preparation was similar to the method described above, except that the material mass ratios were 80:10:10 $S_{60}MWCNT_{40}$:CB:NaCMC, and the cathodes were cut into thin 0.5 cm x 10 cm strips. Optical cell anodes consisted of a 0.5 cm x 0.5 cm coating of Na (Sigma-Aldrich) pressed into the midline of a 0.5 cm x 10 cm strip of copper foil (99.999% pure, 25 μm thick). A reference electrode was also used for these tests, and it consisted of 0.5 cm x 5 cm strip of copper foil with Na pressed to the end. The cathode and anode strips were fed through a 0.25 cm x 0.5 cm gap in the center of a plastic plate, and pulled taut opposite one another. Front and rear plates each with a 1" diameter quartz viewing window over the electrode gap were placed in front of and behind the center plate. The front and rear plates are separated from the center plate using 006 Viton O-rings, and secured using nylon bolts. The reference electrode was inserted underneath an O-ring into the viewing area, and all electrodes are sufficiently separated as to not short the cell. Finally, around 1 mL of electrolyte was injected into the viewing window using a needle syringe. The cells were galvanostatically discharged at C/2 rate while a Lumenera Infinity camera with a Navitar Zoom 6000 lens took images of the electrode gap in the viewing window. The magnification used was 3.38x and the resolution limit was 7.67 μm.

A Java computer program processed each image to analyze the colors and thus the different polysulfide species present in the electrolyte at the time the image was taken. Each image corresponds to a moment in time in the discharge. First, the program isolated the electrolyte from the electrodes in the image by determining where the RGB values of adjacent pixels changes by more than 75%. The electrolyte region was then treated as an array of 2-D pixels, and each pixel had a red, green, or blue color value between 0 and 255. The RGB values of each pixel was used to determine the average color in the electrolyte. The program also determined the ratios of red, green, and blue to the average electrolyte color. The program added the average color of each image together sequentially to create a diagram of how the average color changed over time. Reprinted (adapted) with permission from Rachel Carter, Addison NewRingeisen, **Daniel Reed**, Robert W. Atkinson III, Partha P. Mukherjee, and Corey T. Love, "Optical Microscopy Reveals the Ambient Sodium-Sulfur Discharge Mechanism," *ACS Sustainable Chemistry and Engineering*, 9(1), 92-100, 2021. Copyright 2021 American Chemical Society.

4.2   Results and Discussion

Galvanostatic cycling of coin cells with G1, G2, or G4 electrolytes and optical microscopy of optical cells during galvanostatic discharge provided valuable insights into the effects of glyme solvent on cell performance. Cell performance is assessed through initial discharge capacity, discharge capacity fade, coulombic efficiency, and the location and length of plateaus in the discharge/charge curves in RT Na-S coin cells with G1, G2, and G4 electrolytes. In optical cells, performance is assessed through the time to full discharge as well as the color and color components of the electrolyte at each imaging point.

4.2.1   Cell Performance in G1-, G2-, and G4-Based Cells

Figure 4.2 gives the discharge and charge voltage profiles with respect to specific capacity for each cycle of a RT Na-S cell with 1M $NaPF_6$ in G1 electrolyte. In Figure 4.2, cycles 1-5 and cycle 8 are shown. The specific discharge capacity decreased from 469 mAh g^{-1} in the 1st cycle to just 37 mAh g^{-1} in the 8th cycle, so cycling was terminated after cycle 8. In Figure 4.2(a), the specific capacity of each cycle can be seen, and the full extent of the charge in cycle 1 is illustrated in Figure 4.2(b).
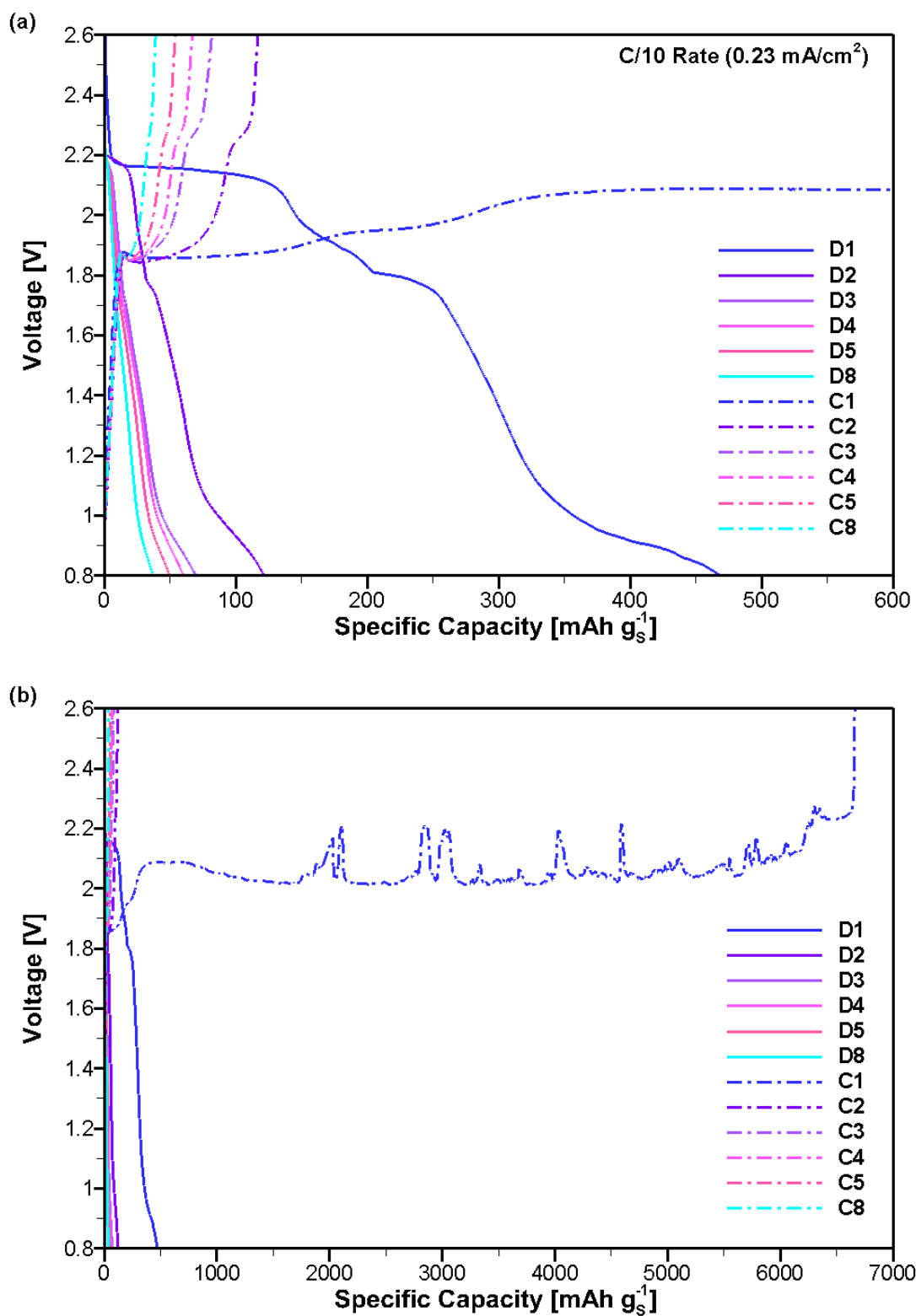
Figure 4.2. Charge/discharge curves for a G1-based RT Na-S cell cycled at C/10 rate. Solid lines represent discharge curves, and dashed lines represent charge curves. The discharge and charge capacities are shown clearly in **(a)**, but the full extent of the 1st charge curve is shown in **(b)**.

The G1-based RT Na-S cell of Figure 4.2 exhibits an extremely large, near infinite first charge, as well as a rapid capacity fade after the first cycle. The large first charge leads to a coulombic efficiency of over 1400% in the first cycle, which can be seen in Figure 4.5(b). After the first cycle, the coulombic efficiency stabilizes to values near 100%. The initial specific discharge capacity of 469 mAh g^{-1} corresponds to an average polysulfide reduction state between Na_2S_4 and Na_2S_3. The first discharge profile of the G1-based cell exhibits three distinct voltage profiles. The first occurs between 2.2 and 2.1 V, the second occurs around 1.8 V, and the third occurs around 0.9 V. These plateaus correspond to different intermediate steps from the reduction of S_8 to Na_2S in the cathode. During the high voltage plateau at 2.2-2.1 V and during the downward sloping region between 2.1 V and 1.8 V, the cell undergoes solid-liquid and liquid-liquid reactions as solid S_8 is converted to Na_2S_8 and then to Na_2S_4 through a series of reduction reactions [45] [59]. In these regions, long-chain polysulfides can chemically disproportionate or dissociate to form the $S_3^{\bullet-}$ radical, which will decrease sulfur utilization [58] [78]. During the plateau at 1.8 V, the downward sloping region between 1.8 and 1.1 V, and the plateau at 0.9 V, the cell undergoes liquid-solid and solid-solid reactions as soluble long-chain polysulfides are converted to the final discharge product of Na_2S [45] [59]. Most of the capacity achieved during the first discharge is accrued during the voltage plateaus. During subsequent cycles, the locations of the plateaus do not change, but the capacity derived from each changes dramatically. The theoretical specific capacity for the conversion of S_8 to S_8^{2-} is 209 mAh g^{-1}, and this reaction takes place in the high voltage plateau at 2.2-2.1 V [45]. According to Figure 4.2(a), the G1-based cell achieves nearly 150 mAh g^{-1} during the high voltage plateau, which shows that sulfur utilization is high during this step. In contrast, the second and third voltage plateaus produce less capacity, and show poor sulfur utilization since the theoretical capacity of solid-solid low-order polysulfide conversion is much higher than that of the solid-liquid and liquid-liquid reduction reactions. During the second discharge, the capacity achieved during each voltage plateau decreases significantly compared to the first discharge. During the third discharge, the capacity achieved during each voltage plateau decreases again, and the capacities of the first and second voltage plateaus are now nearly negligible. Between cycles 3 and 8, the capacities of the intermediate reactions occurring at voltages above 1.8 V decrease at a much lower rate than those occurring at voltages at or below 1.8 V. This is expected because irreversible formation of insulating low-order sodium polysulfides during charging has been shown to be a degradation mechanism in RT Na-S batteries [65]. The

charge profiles of the G1-based RT Na-S cell also show a series of voltage plateaus that indicate different oxidation reactions taking place at the cathode. However, both the number of plateaus, their locations, and their length change with cycling. The first charge voltage plateau occurs between 1.8 and 1.9 V. This first plateau does not change positions and is present in all charge half cycles. The second charge voltage plateau is very subtle and occurs between 1.9 and 2.0 V. This plateau disappears from subsequent charge profiles after the first cycle. The third charge voltage plateau occurs between 2.0 and 2.1 V, which can be clearly seen in Figure 4.2(b). However, the location of this plateau changes between cycles. During the second and third cycles, the high voltage charge plateau is now located between 2.2 and 2.3 V. After the third cycle, this plateau shrinks to almost imperceptible levels. The capacity derived from this high voltage charge plateau also decreases with cycling in cycles 1-3. As demonstrated in Figure 4.2(b), the G1-based cell nearly fails to recharge due to infinite charging behavior during the first cycle.

Figure 4.3 provides the discharge and charge curves for each cycle for a RT Na-S cell with 1M $NaPF_6$ in G2 electrolyte. The G2-based cell produced an initial specific discharge capacity of 401 mAh g^{-1}, which is shown clearly in Figure 4.3(a). This corresponds to an average polysulfide reduction state between Na_2S_5 and Na_2S_4. Notably, all of the G2-based cells tested in this study did not recharge fully, as they all exhibited an infinite charging behavior during the first cycle. The extent of the infinite charge at a nearly constant voltage is shown in Figure 4.3(b).
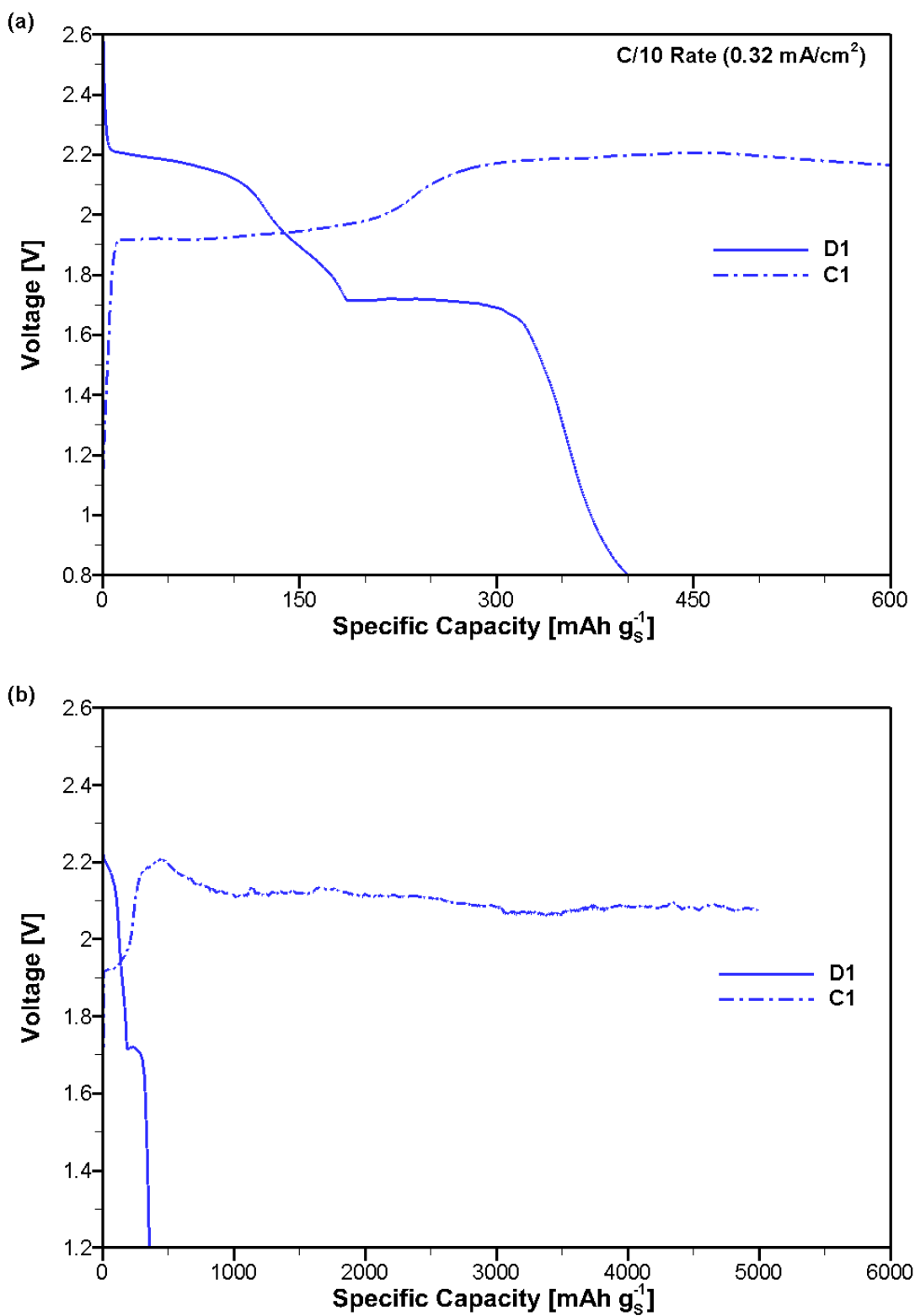
Figure 4.3. Discharge and charge curves for a G2-based RT Na-S cell cycled at C/10 rate. Only one cycle is shown, because the G2-based cells were not rechargeable. The discharge capacity is shown clearly in **(a)**, and the extent of the charge capacity is shown in **(b)**.

The discharge and charge profiles of the G2-based cell also contain different plateau and sloping regions where certain intermediate reactions take place. The discharge profile contains two plateaus; the high voltage plateau occurs at 2.2 V, while the low voltage plateau occurs at 1.7 V. There does not appear to be a voltage plateau below 1.0 V, as there was for the G1-based cell. Here, the solid-liquid and liquid-liquid reactions occur at voltages above 1.7 V, while the liquid-solid and solid-solid reactions occur at or below 1.7 V [45] [59]. The sulfur utilization in the high voltage plateau for the G2-based cell appears just slightly lower than that for the G1-based cell, but the low voltage plateau for the G2-based cell provides a higher sulfur utilization than the corresponding voltage plateau for the G1-based cell. The charge profile of the G2-based cell exhibits two voltage plateaus. The lower voltage plateau lies between 1.9 and 2.0 V, but the voltage of the high voltage charge plateau changes during the first charge. In Figure 4.3(a), it appears that it lies at 2.2 V. However, it is closer to 2.1 V by the time the test has terminated in the expanded view in Figure 4.3(b). Thus, the voltage slowly decreases with time during the infinite charge. As in the first cycle near-infinite charge of the G1-based cell, the infinite charge of the G2-based cell begins at the highest charge voltage plateau.

The discharge and charge profiles for cycles 1-5 and cycle 11 of a RT Na-S cell with 1M NaPF$_6$ in G4 electrolyte is shown below in Figure 4.4. Unlike the G1- and G2-based cells, there is no infinite charging observed in the first five cycles of the G4-based cell. However, infinite charging does begin during the 11th cycle, at which point the test was terminated. Although infinite charging in the G4-based cell is late-onset, it is notable that the coulombic efficiency of each cycle is still much larger than 100%, as each charge capacity is larger than its corresponding discharge capacity. The initial specific discharge capacity of the G4-based cell is 280 mAh g^{-1}, which can be seen in Figure 4.4(a). This corresponds to an average polysulfide reduction state of Na$_2$S$_6$.

(a)

C/10 Rate (0.22 mA/cm^2)
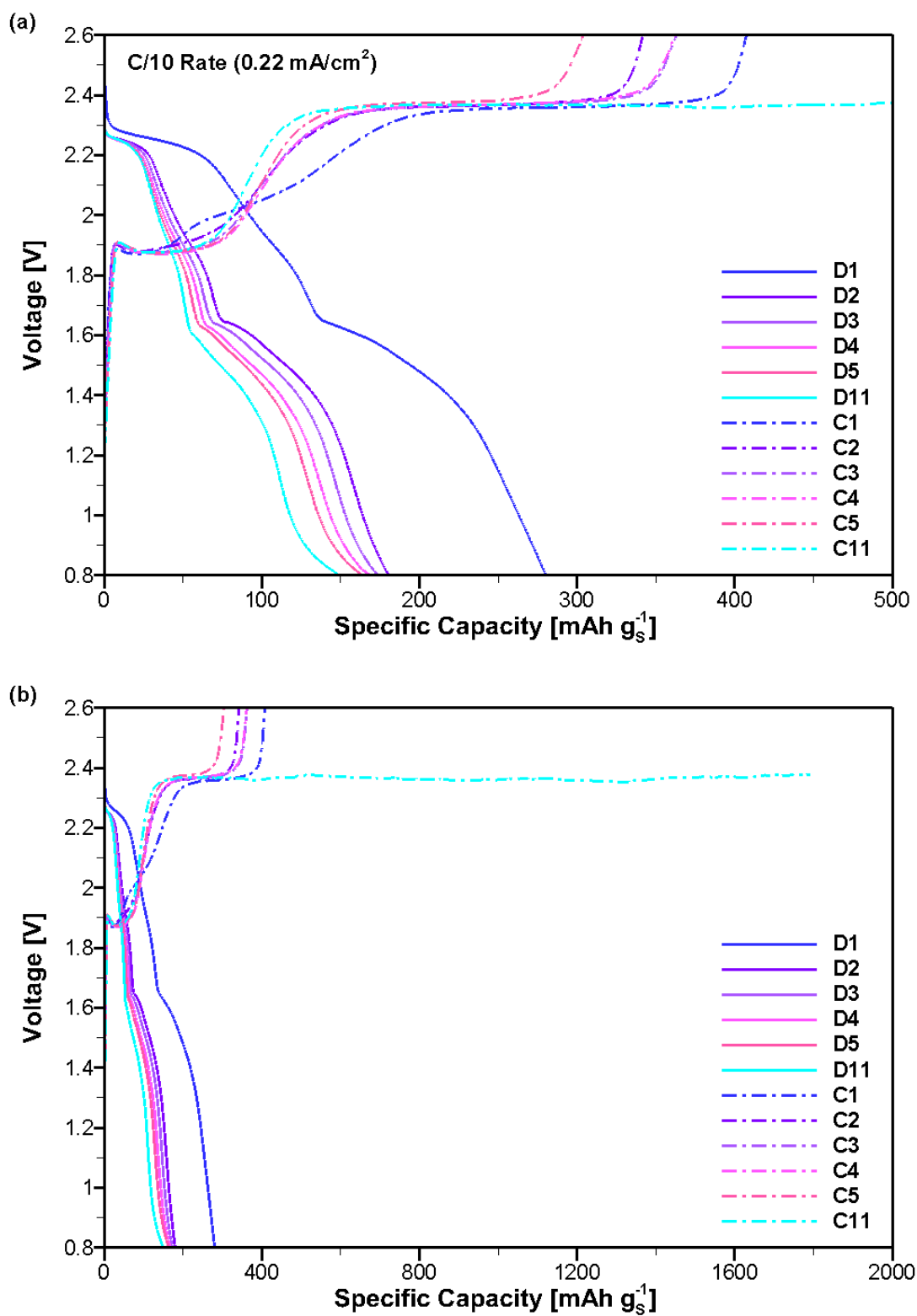
Figure 4.4. Discharge and charge curves for a G4-based RT Na-S cell cycled at C/10 rate. Discharge capacities are shown clearly in **(a)**, and the extent of the 11th charge is shown in **(b)**.

The discharge and charge plateaus of the G4-based cell are slightly different than those of the G1-based cell or the G2-based cell. The G4-based cell has two distinct voltage plateaus during each discharge profile. These plateaus do not change location during cycling, but they do change in both absolute and relative size. The high voltage discharge plateau occurs between 2.3 and 2.2 V, while the low voltage plateau occurs between 1.7 and 1.6 V. The capacity fade between the first and second discharge cycles affects both plateau regions equally; however, from the second discharge onwards there is very little capacity loss in the high voltage plateau between 2.3 and 2.2 V. In contrast, the capacity of the low voltage plateau between 1.7 and 1.6 V fades noticeably faster. This indicates that the solid-liquid and higher-order liquid-liquid conversion reactions are very reversible in G4-based electrolyte, while the liquid-solid and solid-solid conversion reactions are more irreversible [65]. These capacity retention results stand in sharp contrast with the G1-based cell, which suffered from a large capacity fade between the second and third cycles as well as between the first and second cycles. The charge profiles consist of two clearly defined voltage plateaus that do not change location during cycling. The low voltage charge plateau occurs just under 1.9 V, while the high voltage charge plateau occurs between 2.3 and 2.4 V. The slope of the charge profile of the first cycle changes between 2.0 and 2.1 V, but this feature disappears after the first cycle.

Based on Figures 4.2 and 4.4, the cycling performance of G1- and G4-based cells differs substantially. These differences are captured in Figure 4.5, which gives specific discharge capacity as well as coulombic efficiency as a function of cycle number for the G1- and G4-based cells shown in Figures 4.2 and 4.4, respectively. Although Figure 4.4 gives the discharge and charge profiles of the 11th cycle for the G4-based cell, the discharge capacity and coulombic efficiency of the 10th cycle for that cell are given in Figure 4.5 because of the infinite charging behavior that occurred in the 11th cycle.

(a)

(b)
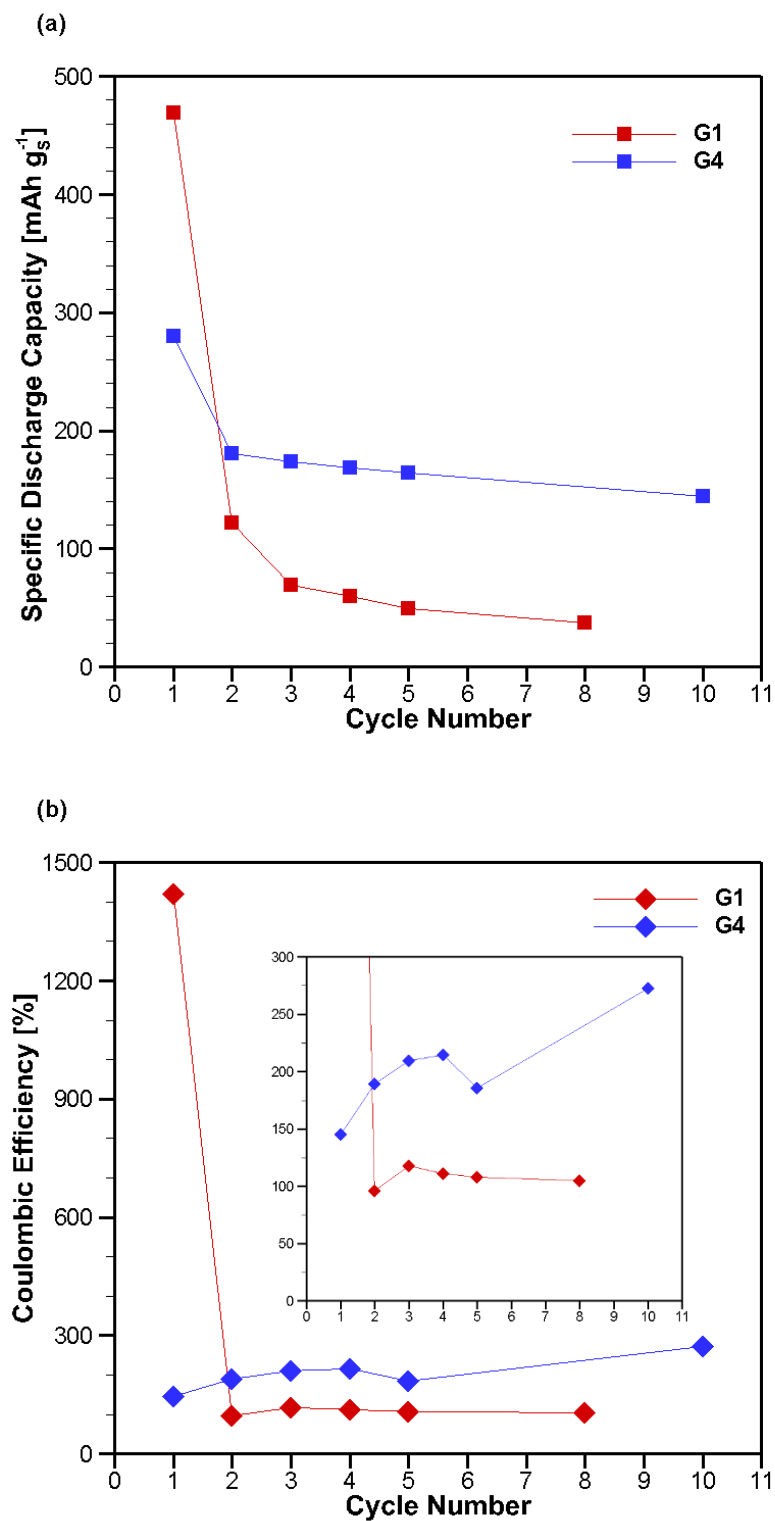
Figure 4.5. (a) Specific discharge capacity and **(b)** coulombic efficiency by cycle for the G1- and G4-based RT Na-S cells shown in Figures 4.2 and 4.4.

Figure 4.5(a) shows that although the G1-based cell achieves a much higher initial specific discharge capacity than the G4-based cell, its capacity retention is far inferior. The discharge capacity fade between the first and second cycles is a massive 74% for the G1-based cell, but it is only 36% for the G4-based cell. Any advantage in initial discharge capacity held by the G1-based cell is wiped away by the second cycle, as the G4-based cell has a large discharge capacity in the second cycle due to its comparatively lower initial capacity fade. The G4-based cell continues to lose capacity at a slower rate than the G1-based cell, and still retains a discharge capacity of 144 mAh g^{-1} after 10 cycles. In contrast, the G1-based cell retains just 37 mAh g^{-1} after 8 cycles. These values correspond to an average capacity fade of 54 mAh g^{-1} cycle^{-1} for the G1-based cell and 14 mAh g^{-1} cycle^{-1} for the G4-based cell. In Figure 4.5(b), coulombic efficiency is calculated according to Equation 4.1, which is shown below.

$$\eta = 100\left(\frac{q_c}{q_d}\right)$$

(4.1)

In Equation 4.1, η, q_c, and q_d refer to coulombic efficiency, charge capacity, and discharge capacity, respectively. The coulombic efficiency of the G1-based cell is initially extraordinarily high due to the infinite charge behavior in the first cycle, but it stabilizes to around 100% during subsequent cycles. However, the coulombic efficiencies of the G4-based cells stay consistently high, from nearly 150% in the first cycle to around 275% by the 10th cycle.

The results from one individual cell type do not necessarily represent the expected performance of that given cell type. Figure 4.6 provides first discharge specific capacity and first to second cycle discharge capacity fade for each electrolyte type as an average of multiple cells for each electrolyte type. Standard error bars are also shown for each data point.
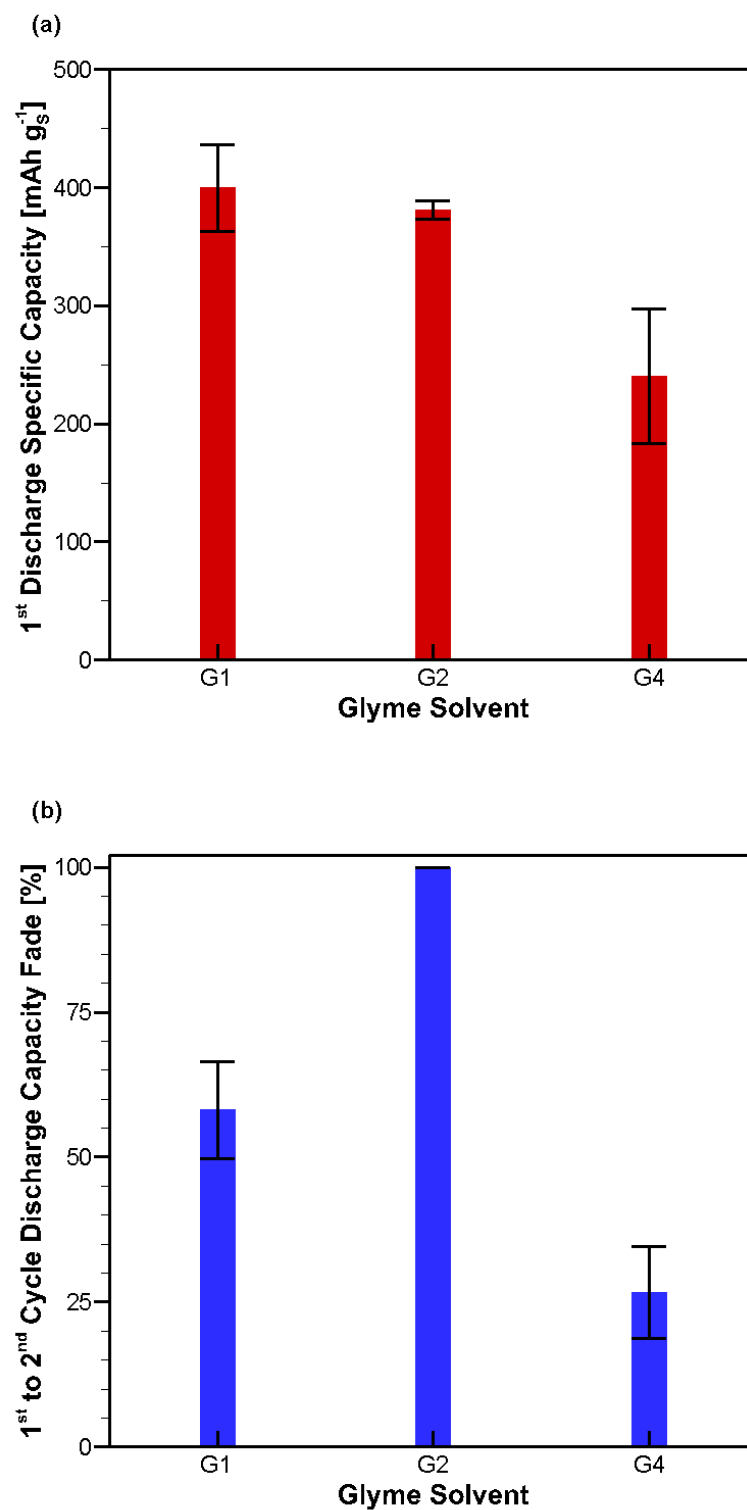
Figure 4.6. Average **(a)** initial discharge specific capacity and **(b)** 1st to 2nd cycle discharge capacity fade across electrolyte types (G1, G2, and G4). The sample size was n = 3 for each electrolyte type.

Each electrolyte category consists of a group of three different cells. As shown in Figure 4.6(a), the trends observed for the individual G1-, G2-, and G4-based cells hold true across the sample size. The average initial discharge specific capacity is highest for the G1-based cells at 400 ± 37 mAh g^{-1}, slightly lower for the G2-based cells at 381 ± 8 mAh g^{-1}, and lowest for the G4-based cells at 240 ± 57 mAh g^{-1}. The G2-based cells had the largest average first to second cycle discharge capacity fade at $100\pm0\%$ since all of the cells in the G2 group experienced infinite charging during the first cycle. The G1-based cells also had high average first to second cycle discharge capacity fade at $58\pm8\%$. The G4-based cells experienced the lowest average first to second discharge capacity fade at $26.7\pm8\%$. The G1-based cells tested in this studied produced the highest initial discharge capacities among the three cell groups, but the reversibility of these cells was very poor. Although the G4-based cells delivered inferior initial capacity, their reversibility was significantly better than the other cell types tested.

4.2.2   *Infinite Charging and Polysulfide Shuttle*

While cycling RT Na-S coin cells, three distinct charging behaviors were observed. Examples of each of the three charging behaviors are given below in Figure 4.7. The first type of charging behavior is characterized by a charge capacity less than or equal to the discharge capacity of that cycle such that the coulombic efficiency of the cell is less than or equal to 1 (red curve in Figure 4.7). This behavior occurred in the G1-based RT Na-S cells. This is the expected behavior, as the number of sodium ions plated on the anode during charging should be equal or less than the number of sodium ions stripped during discharge. The second charging behavior is characterized by an elongated high voltage plateau that increases the charge capacity so that it is larger than the discharge capacity of that cycle (black curve in Figure 4.7). However, the cell voltage will eventually reach the upper cutoff voltage and complete the charging process, usually with a coulombic efficiency less than 3. This type of behavior occurred in both the G1- and the G4-based RT Na-S cells. The third type of charging behavior is the most insidious of them all: the infinite charge (orange curve in Figure 4.7). This behavior is characterized by the cell voltage remaining constant at the high voltage plateau for a seemingly endless period of time. The cell continues to accumulate charge capacity, and the voltage of the cell may decline at a very slow rate. Infinite charging occurred in all three of the cell types.
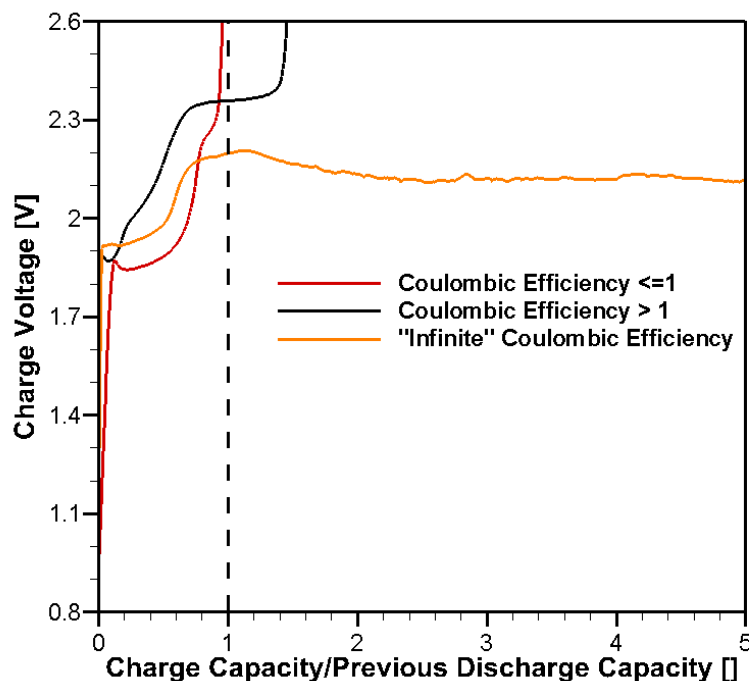
Figure 4.7. Different charging behaviors observed in RT Na-S coin cells. Coulombic efficiency is defined by the charge capacity at each data point divided by the final discharge capacity achieved in the previous half cycle. During some cycles, coulombic efficiency is at or below 100%, which is expected cell behavior. During other cycles, coulombic efficiency is greater than 100%, but the voltage eventually reaches the upper cutoff voltage of 2.6. The third type of charging behavior is an "infinite" charge in which the voltage plateaus around 2.1-2.2 V and never reaches the upper cutoff voltage.

Results from Chapter 3 indicate that dendritic plating on the anode does not cause infinite charging, because very little evidence of dendritic plating was observed in Na/Na symmetric coin cells cycled at 0.5 mA cm^{-2} and the RT Na-S coin cells were cycled at lower rates than any of the Na/Na symmetric cells. Additionally, infinite charging cannot be explained by difficulty in oxidizing low-order, insulating polysulfide species, because the electrical resistance from these species would cause the voltage to increase to the upper cutoff voltage quickly. Rather, infinite charging can be most readily explained by excessive polysulfide shuttle effect in the affected cells. As lower-order polysulfides are converted to higher-order, more soluble polysulfides during the higher voltage portion of the charge, these newly oxidized species can migrate through the electrolyte to the anode where they are reduced. The reduced polysulfides can either corrode the anode or migrate back to the cathode to be oxidized again. If the rate of oxidation is equal to the rate at which polysulfides migrate away from the cathode, then infinite charging occurs. This

90

process is heavily dependent on the transport properties of the electrolyte, which is why it affects each cell type in different ways. According to Mikhaylik and Akridge, polysulfide shuttling during the charge of Li-S cells is also dependent on the amount of usable sulfur in the cell, the high voltage plateau capacity, the charging current, and a shuttle constant that is a function of electrolyte salt concentration and temperature, among other properties [68]. They observed infinite charging in simulated and experimental Li-S cells when the charging current was low relative to the product of the high-order polysulfide concentration and shuttle constant. This relationship explains why infinite charging occurs at different cycle numbers across the RT Na-S cell types. In the G1-based RT Na-S cell of Figure 4.2, the cell experiences a near-infinite charge during the first cycle because the charging current is very close to the minimum infinite charging current dictated by the sulfur concentration and electrolyte properties. As the charge proceeds, more polysulfides migrate to the anode and corrode it, which reduces the concentration of long-chain polysulfides that appear during the high voltage charge plateau. This lowers the infinite charging current so that the cell charging current is higher, and the upper cutoff voltage is reached. Because available sulfur is reduced during this process, there is a massive discharge capacity drop between the first and second cycles. Also, the loss of sulfur that contributes to high voltage plateau capacity prevents the infinite charge behavior from occurring again. The minimum infinite charging current of the G2-based RT Na-S cells is larger than the cell charging current, so the G2-based RT Na-S cells are affected by infinite charging during the first cycle. Thus, they are strongly affected by the polysulfide shuttle at these operating conditions. The G4-based cells do not experience infinite charging during the first few cycles, but the cell in Figure 4.4 begins a period of infinite charging during the 11th cycle. However, the G4-based cells have larger charge capacities than discharge capacities during each cycle. This happens because the G4-based cell experiences a moderate polysulfide shuttle during the first ten cycles. The minimum infinite charge current of the G4-based RT Na-S cells is just slightly lower than the cell charging current. However, as cycling continues the rate of polysulfide migration increases, and eventually becomes equivalent to the oxidation rate during the 11th cycle. Infinite charging behavior is an indicator for the extent of polysulfide shuttle in RT Na-S cells. Based on the onset and extent of infinite charge in the RT Na-S cells in this study, G2-based cells suffer from extensive polysulfide shuttle. G1- and G4-based cells are affected to a lesser extent.

4.2.3   Redox Mechanisms Probed Using Optical Microscopy

Results from optical microscopy experiments using RT Na-S optical cells were first published in Rachel Carter, Addison NewRingeisen, **Daniel Reed**, Robert W. Atkinson III, Partha P. Mukherjee, and Corey T. Love, "Optical Microscopy Reveals the Ambient Sodium-Sulfur Discharge Mechanism," *ACS Sustainable Chemistry and Engineering*, 9(1), 92-100, 2021 (reference [78]). In order to show how the image analysis program can compare optical cell performances, image sequences from the initial discharges of G1, G2, and G4 RT Na-S optical cells were analyzed, which allowed intermediate polysulfides to be assigned to distinct cell voltages. In this way, the conversion reactions can be compared, and these results are shown below in Figure 4.

Figure 4.8. Electrochemical and optical analyses of discharge in G1 (left column), G2 (center column), and G4 (right column). (A, E, I) Voltage during C/2 galvanostatic discharge. (B, F, J) RGB pixel analysis including pixel ratio and image brightness aligned with discharge voltage. (C, G, K) Resulting average electrolyte color bar. Distinct changes in electrolyte color are indicated with gray vertical lines and notated with the polysulfide responsible for these changes. (D, H, L) Photographs of the optical cell window at completion of the electrochemical discharge. Reprinted (adapted) with permission from Rachel Carter, Addison NewRingeisen, **Daniel Reed**, Robert W. Atkinson III, Partha P. Mukherjee, and Corey T. Love, "Optical Microscopy Reveals the Ambient Sodium-Sulfur Discharge Mechanism," *ACS Sustainable Chemistry and Engineering*, 9(1), 92-100, 2021. Copyright 2021 American Chemical Society.
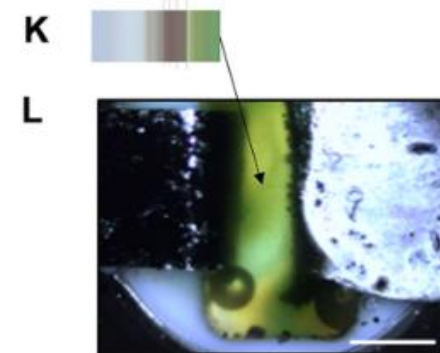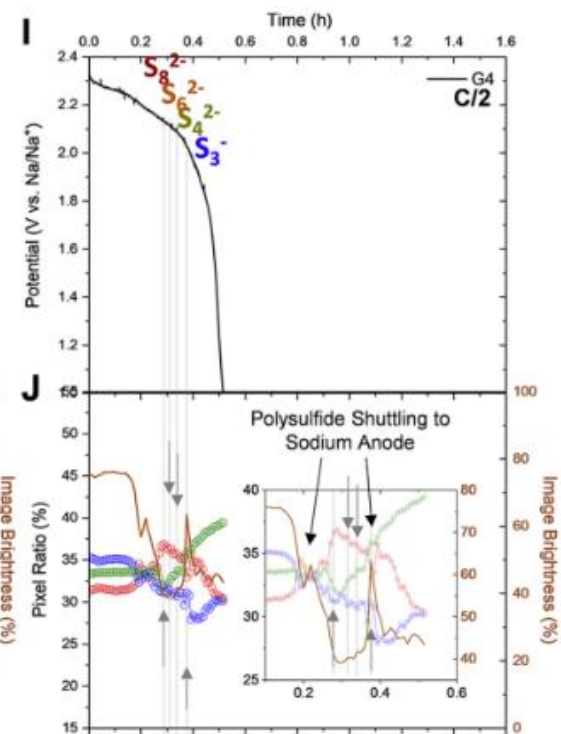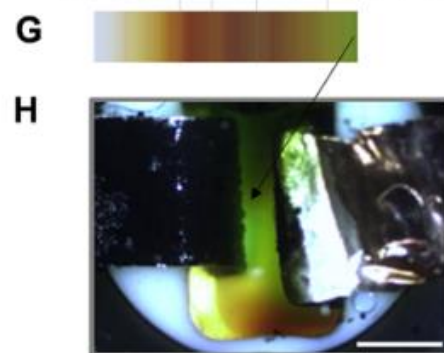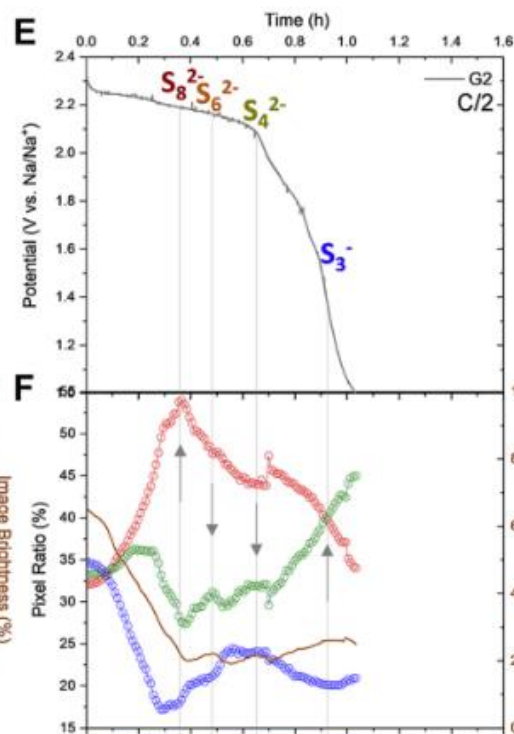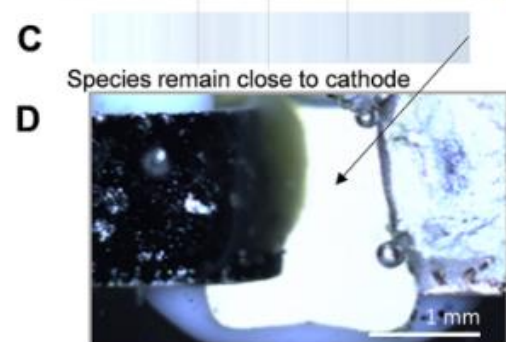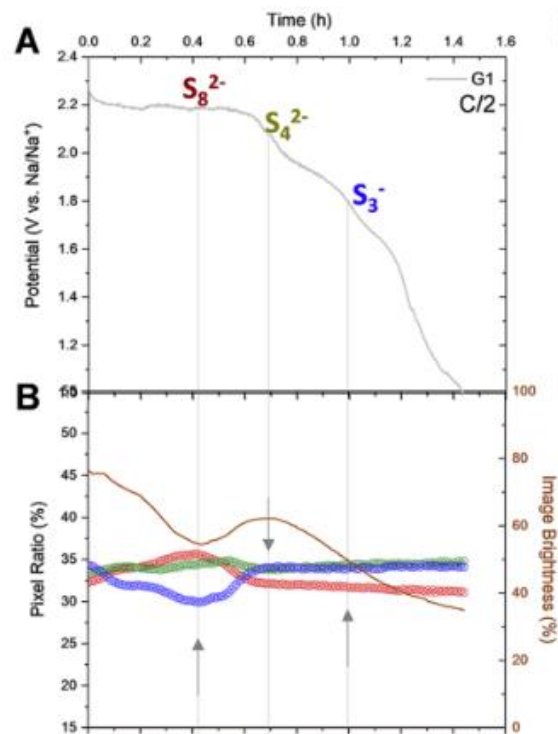
The results from the G1-based optical cell are shown in the first column of Figure 4.8, and Figure 4.8A shows that the G1 voltage was constant for the first 0.4 h of discharge. This corresponds with the formation of the S_8^{2-} polysulfide. Figure 4.8B shows that the relative R content of the electrolyte pixels increases and brightness decreases during this period, which is consistent with the formation of S_8^{2-}. Between 0.4 and 0.7 h of discharge, the yellow S_4^{2-} polysulfide forms in the electrolyte, which is evidenced by the decrease in relative R content of the electrolyte pixels and an increase in brightness. The relative peak in brightness corresponds to the end of the high voltage plateau. Between the end of the high voltage plateau and the lower voltage cutoff of 1 V, liquid-solid redox reactions convert soluble polysulfides to insoluble, solid polysulfides. Because of the slow reaction kinetics associated with the formation of the solid reaction product Na_2S [61], the $S_3^{•-}$ sulfur radical is detected during this period. The increase of relative B and G content of the electrolyte pixels above that of R as well as the decrease in image brightness indicates that the sulfur radical concentration in the electrolyte continues to increase until the end of the discharge. The two plateaus seen in the discharge during this period are associated with the formation of Na_2S_2 and Na_2S, respectively. Optical image analysis by itself cannot confirm this conclusion, since these solid products do not produce color in the electrolyte. Throughout the duration of the G1-based optical cell discharge, the net image brightness decreased only around 40%, and the pixel ratio only changed around 5%. Figure 4.8C shows that the average color throughout the entire discharge remains mostly transparent, and Figure 4.8D shows that the soluble polysulfides remain close to the cathode. By compiling all of the images from the discharge together, it is clear that the polysulfides remained close to the cathode throughout the discharge. Despite showing evidence of sulfur radical formation, the G1-based cell achieved a discharge capacity that was around 72% of the theoretical value due to its ability to keep the soluble products close to the cathode. This indicates that electrochemical reactions are dominant over chemical ones in the G1 solvent.

The G2-based optical cell reached the lower voltage cutoff during discharge faster than the G1-based cell, which indicates that the G2-based cell produced less discharge capacity than the G1-based cell. Despite this, the high voltage plateau ends at around the same time (0.6 h) for the G2-based cell as it does for the G1-based cell. Figure 4.8E shows that the voltage of the G2-based cell drops precipitously after the high voltage plateau, which is due to a higher degree of chemical

disproportionation reactions in G2. Because of this, the S_6^{2-} polysulfide is detected during the high voltage plateau, which will form the $S_3^{\bullet-}$ sulfur radical when reaction kinetics slow at the end of the high voltage plateau. As a result, the discharge capacity produced by the G2-based cell is only around 52% of the theoretical value. Figures 4.8F and 4.8G show that the G2-based cell electrolyte experienced more coloration and less brightness during discharge than that of the G1-based cell. The green color in the electrolyte in Figure 4.8H at the end of discharge indicates that the degree of sulfur radicalization is high between the electrodes, but the darker color at the bottom of the cell indicates that long-chain polysulfides like S_8^{2-} or S_6^{2-} sank to the bottom of the cell. The sinking of long-chain polysulfides away from the electrodes contributes to the capacity defect, but is also a result of the optical cell orientation and geometry during the experiment. However, it does show that the polysulfide shuttle effect occurs in G2 electrolytes.

Figure 4.8I shows that the G4-based optical discharges rapidly and thus attains the lowest discharge capacity of the three glyme electrolytes tested. Figure 4.8J demonstrates that the reaction mechanism in G4 is similar to that in G2. At the peak in S_8^{2-} concentration at 0.3 h, the formation of S_4^{2-} begins. The former is evidenced by a local maximum of relative R content of electrolyte pixels and minimum of image brightness in the electrolyte, and the latter is evidenced by decreasing relative R content of electrolyte pixels and brightness. The inset of Figure 4.8J shows that the G4-based cell experiences trends similar to those of the G2-based cell in B content of electrolyte pixels, G content of electrolyte pixels, and image brightness in the regions after the S_8^{2-} peak. However, the trends in the G4-based cell occur in a shorter period of time. These results demonstrate that polysulfide chemical reordering processes occur readily in the G4 electrolyte. After the peak in S_8^{2-} concentration, relative R content of electrolyte pixels decreases while the relative contents of B and G increase, which indicates the formation of the $S_3^{\bullet-}$ radical in the electrolyte. Figure 4.8K shows the progression of average color during the discharge, and the two increases in image brightness at 0.22 and 0.38 h correspond to light regions in Figure 4.8K. A video composed of a sequence of the images taken during the discharge shows that the formation of soluble polysulfides during discharge induces turbulence in the electrolyte. Turbulent mixing is evident at the end of the reaction, shown in Figure 4.8L. Turbulent mixing disperses the active material and is responsible for the low capacity of the discharge as well as the peaks in electrolyte transparency and brightness. Reprinted (adapted) with permission from

96

Rachel Carter, Addison NewRingeisen, **Daniel Reed**, Robert W. Atkinson III, Partha P. Mukherjee, and Corey T. Love, "Optical Microscopy Reveals the Ambient Sodium-Sulfur Discharge Mechanism," *ACS Sustainable Chemistry and Engineering*, 9(1), 92-100, 2021. Copyright 2021 American Chemical Society.

5. CONCLUSION

5.1   Summary

This work sought to understand how cell performance at the Na anode and S cathode is affected by different electrolyte solvents in RT Na-S cells. Specifically, three commonly used glyme ether solvents were used: G1, G2, and G4. A review of the available RT Na-S literature revealed that electrolyte choice strongly affects SEI formation and stability, polysulfide shuttle, and redox mechanism. Based on a sample of 25 cells from the literature, it was found that on average, carbonate-based cells provide a larger initial specific discharge capacity than ether-based cells (652 mAh g^{-1} vs. 1268.6 mAh g^{-1}, respectively). However, ether-based cells showed a lower average first to second cycle discharge capacity fade than carbonate-based cells (16.3% vs. 24.3%, respectively), a crucial metric of reversibility. In order to test how G1, G2, and G4 affect Na stripping and plating, Na/Na symmetric coin cells were constructed to isolate the anode-electrolyte interactions from the cathode-electrolyte interactions. The Na/Na symmetric cells were cycled at low (0.5 mA cm^{-2}), moderate (1.0 mA cm^{-2}), and high (3.0 mA cm^{-2}) current densities. Additionally, EIS measurements were conducted every five cycles at 0.5 mA cm^{-2} to gauge how the cell SEI changed with cycling. All else being equal, glyme solvent choice has a strong effect on Na plating and stripping characteristics in Na/Na symmetric cells. Additionally, cell performance was revealed to be strongly rate dependent for a given electrolyte. G1-based symmetric cells showed excessively high overpotentials during the first half cycle at low current density, and showed increasingly unstable and dendritic plating and stripping at moderate and high current density. G4-based symmetric cells cycled stably at slightly higher overpotentials than G2-based cells, but they could not be cycled at high current density. Due to its ability to enable mostly stable cycling at relatively low overpotentials at low, moderate, and high current density, the G2 solvent proved to be the superior choice among the three glyme ether solvents studies. In order to investigate how glyme solvent choice affected S cathode dynamics, RT Na-S full coin cells were constructed and cycled at C/10 rates. In addition, sequential photographs taken of RT Na-S optical cells during discharge were optically analyzed using a computer program to determine which polysulfides were present in the electrolyte at different points of the discharge for each electrolyte. G1-based coin cells exhibited the highest average initial specific discharge capacity of the three electrolytes at

400 ± 37 mAh g^{-1}, ahead of the G2-based cells at 381 ± 8 mAh g^{-1} and the G4-based cells at 240 ± 57 mAh g^{-1}. However, G4-based cells displayed the best reversibility, with an average first to second cycle discharge capacity fade of $27\pm8\%$, ahead of the G1-based cells at $58\pm8\%$ and the G2-based cells at $100\pm0\%$. All of the cell types experienced infinite charging to different degrees and at different cycle numbers. Infinite charging was shown to be an indicator for polysulfide shuttle during the charge. Optical cell results showed that discharge capacity during the first cycle increased as glyme molecule size decreased, which was in line with the results obtained from RT Na-S coin cells. Additionally, the $S_3^{\bullet-}$ radical formed readily in G2 and G4 electrolytes, while the G1-based cell experienced radical formation to a lesser extent. The G1 electrolyte kept dissolved polysulfide species close to the electrode surfaces.

Overall, G2-based electrolytes provided the best performance on the Na anode side of the cell. However, the superior solvent choice for S cathode performance was not as clear. G1-based cells provided the highest initial specific discharge capacity, but they suffered from poor reversibility. On the other hand, G4-based cells provided the worst initial specific discharge capacity, but they were the most reversible of the cell types tested. Since each solvent showed a set of advantages and disadvantages, a blend of the three solvents could improve all-around cell performance. The hypothesis postulated in Chapter 2.3 was disproven, as the high viscosity of G4 did not result in a high initial specific discharge capacity. G4-based cells did prove to be the most reversible, but optical cell analysis showed a dispersion of polysulfides throughout the electrolyte during discharge.

5.2 Future Work

More work needs to be done to fully optimize the electrolyte for RT Na-S cells. Blends of the glyme solvents in different proportions should be studied to examine if this would improve performance. This should also be a priority due to the temperature constraints imposed by freezing and boiling points of G1, G2, and G4. As shown in Figure 2.2, the boiling temperature of G1 is around 80°C, and the freezing temperature of G4 is around -25°C. The low boiling temperature of G1 is a safety concern, and the high freezing temperature of G4 could prevent its use in cold climates. Thus, a blend could be beneficial to offset these concerns. Future work is also needed to study electrolyte additives and salt concentration, which were not investigated here. Results in the

literature have shown the beneficial effects of certain additives on SEI stability and reaction kinetics, and higher salt concentration has been correlated with improved performance. It is likely that an optimal electrolyte for RT Na-S cells will require an electrolyte additive as well as a salt concentration higher than 1M. Finally, computation studies on the effect of electrolyte solvent choice on cell performance are sorely needed, as they are absent from the literature. This type of work will allow researchers to study the effect of certain parameters on cell performance that may be difficult to test experimentally. RT Na-S research is still in its infancy, but with more work an optimal electrolyte can be elucidated.

REFERENCES

[1]   NASA, "Facts: The Causes of Climate Change," NASA, 27 May 2021. [Online]. Available: https://climate.nasa.gov/causes/. [Accessed 1 June 2021].

[2]   Intergovernmental Panel on Climate Change, "Summary for Policymakers. In: Climate Change 2014: Mitigation of Climate Change. Contribution of Working Group III to the Fifth Assessment Report of the Intergovernmental Panel on Climate Change," Cambridge University Press, Cambridge, UK and New York, NY, USA, 2014.

[3]   U.S. Energy Information Administration, "INTERNATIONAL - Primary energy," [Online]. Available: https://www.eia.gov/international/data/world/total-energy/total-energy-consumption. [Accessed 28 November 2021].

[4]   U.S. Energy Information Administration, "U.S. energy facts explained," 14 May 2021. [Online]. Available: https://www.eia.gov/energyexplained/us-energy-facts/. [Accessed 28 November 2021].

[5]   United States Environmental Protection Agency, "Carbon Pollution from Transportation," 8 June 2021. [Online]. Available: https://www.epa.gov/transportation-air-pollution-and-climate-change/carbon-pollution-transportation. [Accessed 13 December 2021].

[6]   D. Larcher and J.-M. Tarascon, "Towards greener and more sustainable batteries for electrical energy storage," *Nature Chemistry,* vol. 7, pp. 19-29, 2015.

[7]   M. Armand and J.-M. Tarascon, "Building better batteries," *Nature,* vol. 451, pp. 652-657, 2008.

[8]   E. Emilsson and L. Dahllöf, "Lithium-Ion Vehicle Battery Production," IVL Swedish Environmental Research Institute, Stockholm, Sweden, 2019.

[9]   M. Romare and L. Dahllöf, "The Life Cycle Energy Consumption and Greenhouse Gas Emissions from Lithium-Ion Batteries," IVL Swedish Environmental Research Institute, Stockholm, Sweden, 2017.

[10] M. Winter and R. J. Brodd, "What Are Batteries, Fuel Cells, and Supercapacitors?," *Chemical Reviews,* vol. 104, no. 10, pp. 4245-4269, 2004.

[11] A. Yoshino, "The Birth of the Lithium-Ion Battery," *Angewandte Chemie International Edition,* vol. 51, no. 24, pp. 5798-5800, 2012.

[12] C. D. Rahn and C.-Y. Wang, Battery Systems Engineering, West Sussex, UK: John Wiley & Songs, Ltd, 2013.

[13] T. Placke, R. Kloepsch, S. Dühnen and M. Winter, "Lithium ion, lithium metal, and alternative rechargeable battery technologies: the odyssey for high energy density," *Journal of Solid State Electrochemistry,* vol. 21, pp. 1939-1964, 2017.

[14] A. Rosenman, E. Markevich, G. Salitra, D. Aurbach, A. Garsuch and F. F. Chesneau, "Review on Li-Sulfur Battery Systems: an Integral Perspective," *Advanced Energy Materials,* vol. 5, p. 1500212, 2015.

[15] K. Mizushima, P. Jones, P. Wiseman and J. Goodenough, "LixCoO2 (0<x<-1): A new cathode material for batteries of high energy density," *Materials Research Bulletin,* vol. 15, no. 6, pp. 783-789, 1980.

[16] E. Peled, "The Electrochemical Behavior of Alkali and Alkaline Earth Metals in Nonaqueous Battery Systems-The Solid Electrolyte Interphase Model," *Journal of the Electrochemical Society,* vol. 126, no. 12, pp. 2047-2051, 1979.

[17] A. Manthiram, Y. Fu, S.-H. Chung, C. Zu and Y.-S. Su, "Rechargeable Lithium-Sulfur Batteries," *Chemical Reviews,* vol. 114, no. 23, pp. 11751-11787, 2014.

[18] L. Li, S. Basu, Y. Wang, Z. Chen, P. Hundekar, B. Wang, J. Shi, Y. Shi, S. Narayanan and N. Koratkar, "Self-heating-induced healing of lithium dendrites," *Science,* vol. 359, pp. 1513-1516, 2018.

[19] J. Qian, W. A. Henderson, W. Xu, P. Bhattacharya, M. Engelhard, O. Borodin and J.-G. Zhang, "High rate and stable cycling of lithium metal anode," *Nature Communications,* vol. 6, no. 6362, 2015.

[20] J. B. Goodenough and K.-S. Park, "The Li-Ion Rechargeable Battery: A Perspective," *Journal of the American Chemical Society,* vol. 135, pp. 1167-1176, 2013.

[21] M. R. Palacín, "Understanding ageing in Li-ion batteries: a chemical issue," *Chemical Society Reviews,* vol. 47, pp. 4924-4933, 2018.

[22] Apple Inc., "iPhone Battery and Performance," 24 September 2021. [Online]. Available: https://support.apple.com/en-us/HT208387. [Accessed 13 December 2021].

[23] Nissan North America, Inc., "Nissan Leaf 2022," 2021. [Online]. Available: https://www.nissanusa.com/content/dam/Nissan/us/vehicle-brochures/2022/2022-nissan-nissan-leaf-brochure-en.pdf. [Accessed 13 December 2021].

[24] M. Wayland, "Tesla will change the type of battery cells it uses in its standard-range cars," CNBC, 20 October 2021. [Online]. Available: https://www.cnbc.com/2021/10/20/tesla-switching-to-lfp-batteries-in-all-standard-range-cars.html. [Accessed 13 December 2021].

[25] E. J. Cairns and P. Albertus, "Batteries for Electric and Hybrid-Electric Vehicles," *Annual Review of Chemical and Biomolecular Engineering,* vol. 1, pp. 299-320, 2010.

[26] Federal Consortium For Advanced Batteries, "Executive Summary - National Blueprint For Lithium Batteries 2021-2030," United States Department of Energy, 2021.

[27] Hornsdale Power Reserve, "South Australia's Big Battery," Neoen, 2021. [Online]. Available: https://hornsdalepowerreserve.com.au/. [Accessed 15 December 2021].

[28] A. J. Crawford, Q. Huang, M. C. Kintner-Meyer, J.-G. Zhang, D. M. Reed, V. L. Sprenkle, V. V. Viswanathan and D. Choi, "Lifecycle comparison of selected Li-ion battery chemistries under grid and electric vehicle duty cycle combinations," *Journal of Power Sources,* vol. 380, pp. 185-193, 2018.

[29] K. Zaghib, A. Mauger, H. Groult, J. B. Goodenough and C. M. Julien, "Advanced Electrodes for High Power Li-ion Batteries," *Materials,* vol. 6, no. 3, pp. 1028-1049, 2013.

[30] C. F. Lopez, J. A. Jeevarajan and P. P. Mukherjee, "Characterization of Lithium-Ion Battery Thermal Abuse Behavior Using Experimental and Computational Analysis," *Journal of The Electrochemical Society,* vol. 162, no. 10, pp. A2163-A2173, 2015.

[31] C. F. Lopez, J. A. Jeevarajan and P. P. Mukherjee, "Experimental Analysis of Thermal Runaway and Propagation in Lithium-Ion Battery Modules," *Journal of The Electrochemical Society,* vol. 162, no. 9, pp. A1905-A1915, 2015.

[32] Z. Li, J. Huang, B. Y. Liaw, V. Metzler and J. Zhang, "A review of lithium deposition in lithium-ion and lithium metal secondary batteries," *Journal of Power Sources,* vol. 254, pp. 168-182, 2014.

[33] N. Yabuuchi, K. Kubota, M. Dahbi and S. Komaba, "Research Development on Sodium-Ion Batteries," *Chemical Reviews,* vol. 114, no. 23, pp. 11636-11682, 2014.

[34] Y. Wang, D. Zhou, V. Palomares, D. Shanmukaraj, B. Sun, X. Tang, C. Wang, M. Armand, T. Rojo and G. Wang, "Revitalising sodium-sulfur batteries for non-high-temperature operation: a crucial review," *Energy & Environmental Science,* vol. 13, pp. 3848-3879, 2020.

[35] C. B. L. Nkulu, L. Casas, V. Haufroid, T. D. Putter, N. D. Saenen, T. Kayembe-Kitenge, P. M. Obadia, D. K. W. Mukoma, J.-M. L. Ilunga, T. S. Nawrot, O. L. Numbi, E. Smolders and B. Nemery, "Sustainability of artisanal mining of cobalt in DR Congo," *Nature Sustainability,* vol. 1, pp. 495-504, 2018.

[36] G. Nikiforidis, M. van de Sanden and M. N. Tsampas, "High and intermediate temperature sodium-sulfur batteries for energy storage: development, challenges and perspectives," *RSC Advances,* vol. 9, pp. 5649-5673, 2019.

[37] M. Greenwood, M. Wentker and J. Leker, "A bottom-up performance and cost assessment of lithium-ion battery pouch cells utilizing nickel-rich cathode active materials and silicon-graphite composite anodes," *Journal of Power Sources Advances,* vol. 9, p. 100055, 2021.

[38] Battery University, "BU-205: Types of Lithium-ion," Cadex, 22 October 2021. [Online]. Available: https://batteryuniversity.com/article/bu-205-types-of-lithium-ion. [Accessed 19 January 2022].

[39] P. Adelhelm, P. Hartmann, C. L. Bender, M. Busche, C. Eufinger and J. Janek, "From lithium to sodium: cell chemistry of room temperature sodium-air and sodium-sulfur batteries," *Beilstein Journal of Nanotechnology,* vol. 6, pp. 1016-1055, 2015.

[40] E. J. Cheng, N. J. Taylor, J. Wolfenstine and J. Sakamoto, "Elastic properties of lithium cobalt oxide (LiCoO2)," *Journal of Asian Ceramic Societies,* vol. 5, no. 2, pp. 113-117, 2017.

[41] Millipore Sigma, "Lithium sulfide," [Online]. Available: https://www.sigmaaldrich.com/US/en/product/aldrich/213241. [Accessed 7 January 2022].

[42] Millipore Sigma, "Sodium sulfide," [Online]. Available: https://www.sigmaaldrich.com/US/en/product/aldrich/407410. [Accessed 7 January 2022].

[43] Entegris, Inc., "Properties and Characteristics of Graphite," 2013.

[44] C. Doetsch, B. Droste-Franke, G. Mulder, Y. Scholz and M. Perrin, "Electric Energy Storage - Future Energy Storage Demand," IEA ECES26, 2015.

[45] X. Yu and A. Manthiram, "Capacity Enhancement and Discharge Mechanisms of Room-Temperature Sodium-Sulfur Batteries," *ChemElectroChem Communications,* vol. 1, pp. 1275-1280, 2014.

[46] X. Yu and A. Manthiram, "Room-Temperature Sodium-Sulfur Batteries with Liquid Phase Sodium Polysulfide Catholytes and Binder-Free Multiwall Carbon Nanotube Fabric Electrodes," *The Journal of Physical Chemistry C,* vol. 118, pp. 22952-22959, 2014.

[47] L. Fan and X. Li, "Recent advances in effective protection of sodium metal anode," *Nano Energy,* vol. 53, pp. 630-642, 2018.

[48] S. Wei, S. Xu, A. Agrawral, S. Choudhury, Y. Lu, Z. Tu, L. Ma and L. A. Archer, "A stable room-temperature sodium-sulfur battery," *Nature Communications,* vol. 7, no. 11722, pp. 1-10, 2016.

[49] S. C. B. Soni, S. Vineeth and V. Kumar, "Unveiling the physiochemical aspects of the matrix in improving sulfur-loading for room-temperature sodium-sulfur batteries," *Materials Advances,* vol. 2, pp. 4165-4189, 2021.

[50] J. T. Kummer and N. Weber, "Battery Having a Molten Alkali Metal Anode and a Molten Sulfur Cathode". United States Patent 3,413,150, 26 November 1968.

[51] J. T. Krummer and N. Weber, "A Sodium-Sulfur Secondary Battery," *SAE Transactions,* vol. 76, no. 2, pp. 1003-1007, 1968.

[52] J. A. DeGruson, "Sodium Sulfur Batteries for Space Applications," in *1991 NASA Aerospace Battery Workshop*, 1991.

[53] R. Chang and R. Minck, "Sodium-sulfur battery flight experiment definition study," *Journal of Power Sources,* vol. 29, no. 3-4, pp. 555-563, 1990.

[54] T. Oshima, M. Kajita and A. Okuno, "Development of Sodium-Sulfur Batteries," *International Journal of Applied Ceramic Technology,* vol. 1, no. 3, pp. 269-276, 2004.

[55] K. B. Hueso, M. Armand and T. Rojo, "High temperature sodium batteries: status, challenges and future trends," *Energy & Environmental Science,* vol. 6, pp. 734-749, 2013.

[56] B. L. Ellis and L. F. Nazar, "Sodium and sodium-ion energy storage batteries," *Current Opinion in Solid State and Materials Science,* vol. 16, no. 4, pp. 168-177, 2012.

[57] C.-W. Park, J.-H. Ahn, H.-S. Ryu, K.-W. Kim and H.-J. Ahn, "Room-Temperature Solid-State Sodium/Sulfur Battery," *Electrochemical and Solid-State Letters,* vol. 9, no. 3, pp. A123-A125, 2006.

[58] Q. Zou and Y.-C. Lu, "Solvent-Dictated Lithium Sulfur Redox Reactions: An Operando UV-vis Spectroscopic Study," *The Journal of Physical Chemistry Letters,* vol. 7, pp. 1518-1525, 2016.

[59] H. Zhang, T. Diemant, B. Qin, H. Li, R. J. Behm and S. Passerini, "Solvent-Dictated Sodium Sulfur Redox Reactions: Investigation of Carbonate and Ether Electrolytes," *Energies,* vol. 13, p. 836, 2020.

[60] S. Wenzel, H. Metelmann, C. Raiß, A. K. Dürr, J. Janek and P. Adelhelm, "Thermodynamics and cell chemistry of room temperature sodium/sulfur cells with liquid and liquid/solid electrolyte," *Journal of Power Sources,* vol. 243, pp. 758-765, 2013.

[61] A. Manthiram and X. Yu, "Ambient Temperature Sodium-Sulfur Batteries," *Small Structures,* vol. 11, no. 18, pp. 2108-2114, 2015.

[62] "Technical data for Sulfur," [Online]. Available: https://periodictable.com/Elements/016/data.html. [Accessed 16 February 2022].

[63] "Technical data for Carbon," [Online]. Available: https://periodictable.com/Elements/006/data.html. [Accessed 16 February 2022].

[64] S. Xin, Y.-X. Yin, Y.-G. Guo and L.-J. Wan, "A High-Energy Room-Temperature Sodium-Sulfur Battery," *Advanced Materials,* vol. 26, no. 8, pp. 1261-1265, 2014.

[65] X. Yu and A. Manthiram, "Highly Reversible Room-Temperature Sulfur/Long-Chain Sodium Polysulfide Batteries," *The Journal of Physical Chemistry Letters,* vol. 5, no. 11, pp. 1943-1947, 2014.

[66] A. Y. S. Eng, D.-T. Nguyen, V. Kumar, G. S. Subramanian, M.-F. Ng and Z. W. Seh, "Tailoring binder-cathode interactions for long-life room-temperature sodium-sulfur batteries," *Journal of Materials Chemistry A,* vol. 8, no. 43, pp. 22983-22997, 2020.

[67] A. N. Mistry and P. P. Mukherjee, ""Shuttle" in Polysulfide Shuttle: Friend or Foe?," *The Journal of Physical Chemistry C,* vol. 122, no. 42, pp. 23845-23851, 2018.

[68] Y. V. Mikhaylik and J. R. Akridge, "Polysulfide Shuttle Study in the Li/S Battery System," *Journal of the Electrochemical Society,* vol. 151, no. 11, pp. A1969-A1976, 2004.

[69] C. Bao, B. Wang, P. Liu, H. Wu, Y. Zhou, D. Wang, H. Liu and S. Dou, "Solid Electrolyte Interphases on Sodium Metal Anodes," *Advanced Functional Materials,* vol. 30, no. 52, p. 2004891, 2020.

[70] J. Hu, H. Wang, S. Wang, Y. Lei, L. Qin, X. Li, D. Zhai, B. Li and F. Kang, "Electrochemical deposition mechanism of sodium and potassium," *Energy Storage Materials,* vol. 36, pp. 91-98, 2021.

[71] A. Abouimrane, D. Dambournet, K. W. Chapman, P. J. Chupas, W. Weng and K. Amine, "A New Class of Lithium and Sodium Rechargeable Batteries Based on Selenium and Selenium-Sulfur as a Positive Electrode," *Journal of the American Chemical Society,* vol. 134, no. 10, pp. 4505-4508, 2012.

[72] A. Douglas, R. Carter, L. Oakes, K. Share, A. P. Cohn and C. L. Pint, "Ultrafine Iron Pyrite (FeS2) Nanocrystals Improve Sodium-Sulfur and Lithium-Sulfur Conversion Reactions for Efficient Batteries," *ACS Nano,* vol. 9, no. 11, pp. 11156-11165, 2015.

[73] H.-S. Ryu, J.-S. Kim, J.-S. Park, J.-W. Park, K.-W. Kim, J.-H. Ahn, T.-H. Nam, G. Wang and H.-J. Ahn, "Electrochemical Properties and Discharge Mechanism of Na/TiS2 Cells with Liquid Electrolyte at Room Temperature," *Journal of the Electrochemical Society,* vol. 160, no. 2, pp. A338-A343, 2012.

[74] R. Carter, L. Oakes, A. Douglas, N. Muralidharan, A. P. Cohn and C. L. Pint, "A Sugar-Derived Room-Temperature Sodium Sulfur Battery with Long Term Cycling Stability," *Nano Letters,* vol. 17, no. 3, pp. 1863-1869, 2017.

[75] T. H. Hwang, D. S. Jung, J.-S. Kim, B. G. Kim and J. W. Choi, "One-Dimensional Carbon-Sulfur Composite Fibers for Na-S Rechargeable Batteries Operating at Room Temperature," *Nano Letters,* vol. 13, no. 9, pp. 4532-4538, 2013.

[76] B.-W. Zhang, T. Sheng, Y.-D. Liu, Y.-X. Wang, L. Zhang, W.-H. Lai, L. Wang, J. Yang, Q.-F. Gu, S.-L. Chou, H.-K. Liu and S.-X. Dou, "Atomic cobalt as an efficient electrocatalyst in sulfur cathodes for superior room-temperature sodium-sulfur batteries," *Nature Communications,* vol. 9, no. 4082, pp. 1-11, 2018.

[77] Z. W. Seh, J. Sun, Y. Sun and Y. Cui, "A Highly Reversible Room-Temperature Sodium Metal Anode," *ACS Central Science,* vol. 1, pp. 449-455, 2015.

[78] R. Carter, A. NewRingeisen, D. Reed, R. W. Atkinson III, P. P. Mukherjee and C. T. Love, "Optical Microscopy Reveals the Ambient Sodium-Sulfur Discharge Mechanism," *ACS Sustainable Chemistry & Engineering,* vol. 9, no. 1, pp. 92-100, 2021.

[79] Q. Zou and Y.-C. Lu, "Liquid electrolyte design for metal-sulfur batteries: Mechanistic understanding and perspective," *EcoMat,* vol. 3, no. 4, p. e12115, 2021.

[80] M. S. Syali, D. Kumar, K. Mishra and D. Kanchan, "Recent advances in electrolytes for room-temperature sodium-sulfur batteries: A review," *Energy Storage Materials,* vol. 31, pp. 352-372, 2020.

[81] H. Che, S. Chen, Y. Xie, H. Wang, K. Amine, X.-Z. Liao and Z.-F. Ma, "Electrolyte design strategies and research progress for room-temperature sodium-ion batteries," *Energy & Environmental Science,* vol. 10, pp. 1075-1101, 2017.

[82] M. M. Gross and A. Manthiram, "Development of low-cost sodium-aqueous polysulfide hybrid batteries," *Energy Storage Materials,* vol. 19, pp. 346-351, 2019.

[83] X. Yu and A. Manthiram, "Sodium-Sulfur Batteries with a Polymer-Coated NASICON-type Sodium-Ion Solid Electrolyte," *Matter,* vol. 1, no. 2, pp. 439-451, 2019.

[84] F. Tsuji, N. Tanibata, A. Sakuda, A. Hayashi and M. Tatsumisago, "Preparation of Sodium Ion Conductive Na10GeP2S12 Glass-ceramic Electrolytes," *Chemistry Letters,* vol. 47, no. 1, pp. 13-15, 2018.

[85] Y. Uchida, G. Hasegawa, K. Shima, M. Inada, N. Enomoto, H. Akamatsu and K. Hayashi, "Insights into Sodium Ion Transfer at the Na/NASICON Interface Improved by Uniaxial Compression," *ACS Applied Energy Materials,* vol. 2, no. 4, pp. 2913-2920, 2019.

[86] D. Zhou, Y. Chen, B. Li, H. Fan, F. Cheng, D. Shanmukaraj, T. Rojo, M. Armand and G. Wang, "A Stable Quasi-Solid-State Sodium-Sulfur Battery," *Angewandte Chemie International Edition,* vol. 57, no. 32, pp. 10168-10172, 2018.

[87] X. Xu, D. Zhou, X. Qin, K. Lin, F. Kang, B. Li, D. Shanmukaraj, T. Rojo, M. Armand and G. Wang, "A room-temperature sodium-sulfur battery with high capacity and stable cycling performance," *Nature Communications,* vol. 9, no. 3870, pp. 1-12, 2018.

[88] D. Morales, R. E. Ruther, J. Nanda and S. Greenbaum, "Ion transport and association study of glyme-based electrolytes with lithium and sodium salts," *Electrochimica Acta,* vol. 304, pp. 239-245, 2019.

[89] D. Di Lecce, L. Minnetti, D. Polidoro, V. Marangon and J. Hassoun, "Triglyme-based electrolyte for sodium-ion and sodium-sulfur batteries," *Ionics,* vol. 25, pp. 3129-3141, 2019.

[90] S. Tang and H. Zhao, "Glymes as versatile solvents for chemical reactions and processes: from the laboratory to industry," *RSC Advances,* vol. 4, pp. 11251-11287, 2014.

[91] Millipore Sigma, "1,2-Dimethoxyethane," [Online]. Available: https://www.sigmaaldrich.com/US/en/product/sial/259527. [Accessed 19 November 2021].

[92] Millipore Sigma, "Diethylene glycol dimethyl ether," [Online]. Available: https://www.sigmaaldrich.com/US/en/product/sial/281662. [Accessed 19 November 2021].

[93] Millipore Sigma, "Tetraethylene glycol dimethyl ether," [Online]. Available: https://www.sigmaaldrich.com/US/en/product/aldrich/172405. [Accessed 19 November 2021].

[94] Moses, "spider_plot," GitHub, 2022. [Online]. Available: https://github.com/NewGuy012/spider_plot/releases/tag/17.3. [Accessed 21 July 2020].

[95] L. Carbone, S. Munoz, M. Gobet, M. Devany, S. Greenbaum and J. Hassoun, "Characteristics of glyme electrolytes for sodium battery: nuclear magnetic resonance and electrochemical study," *Electrochimica Acta,* vol. 231, pp. 223-229, 2017.

[96] J. Song, G. Jeong, A.-J. Lee, J. H. Park, H. Kim and Y.-J. Kim, "Dendrite-Free Polygonal Sodium Deposition with Excellent Interfacial Stability in a NaAlCl4-2SO2 Inorganic Electrolyte," *ACS Applied Materials & Interfaces,* vol. 7, no. 49, pp. 27206-27214, 2015.

[97] S. Choudhury, S. Wei, Y. Ozhabes, D. Gunceler, M. J. Zachman, Z. Tu, J. H. Shin, P. Nath, A. Agrawal, L. F. Kourkoutis, T. A. Arias and L. A. Archer, "Designing solid-liquid interphases for sodium batteries," *Nature Communications,* vol. 8, no. 898, pp. 1-10, 2017.

[98] G. Wang, X. Xiong, D. Xie, X. Fu, Z. Lin, C. Yang, K. Zhang and M. Liu, "A Scalable Approach for Dendrite-Free Alkali Metal Anodes via Room-Temperature Facile Surface Fluorination," *ACS Applied Materials & Interfaces,* vol. 11, no. 5, pp. 4962-4968, 2019.

111

[99] V. Kumar, Y. Wang, A. Yong Sheng Eng, M.-F. Ng and Z. W. Seh, "A Biphasic Interphase Design Enabling High Performance in Room Temperature Sodium-Sulfur Batteries," *Cell Reports Physical Science,* vol. 1, no. 5, p. 100044, 2020.

[100] H. Wang, C. Wang, E. Matios and W. Li, "Facile Stabilization of the Sodium Metal Anode with Additives: Unexpected Key Role of Sodium Polysulfide and Adverse Effect of Sodium Nitrate," *Angewandte Chemie Internation Edition,* vol. 130, pp. 7860-7863, 2018.

[101] J. Wu, J. Liu, Z. Lu, K. Lin, Y.-Q. Lyu, B. Li, F. Ciucci and J.-K. Kim, "Non-flammable electrolyte for dendrite-free sodium-sulfur battery," *Energy Storage Materials,* vol. 23, pp. 8-16, 2019.

[102] M. Kohl, F. Borrmann, H. Althues and S. Kaskel, "Hard Carbon Anodes and Novel Electrolytes for Long-Cycle-Life Room Temperature Sodium-Sulfur Full Cell Batteries," *Advanced Energy Materials,* vol. 6, no. 6, p. 1502185, 2016.

[103] Y. X. Ren, H. R. Jiang, T. S. Zhao, L. Zeng and C. Xiong, "Remedies of capacity fading in room-temperature sodium-sulfur batteries," *Journal of Power Sources,* vol. 396, pp. 304-313, 2018.

[104] H.-g. Lee, J. T. Lee and K. Eom, "Improving the Stability of an RT-NaS Battery via In Situ Electrochemical Formation of Protective SEI on a Sulfur-Carbon Composite Cathode," *Advanced Sustainable Systems,* vol. 2, no. 11, p. 1800076, 2018.

[105] X.-m. Zhao, Q. Zhu, S.-d. Xu, L. Chen, Z.-j. Zuo, X.-m. Wang, S.-b. Liu and D. Zhang, "Fluoroethylene carbonate as an additive in a carbonates-based electrolyte for enhancing the specific capacity of room-temperature sodium-sulfur cell," *Journal of Electroanalytical Chemistry,* vol. 832, pp. 392-398, 2019.

[106] J.-S. Kim, H.-J. Ahn, I.-P. Kim, K.-W. Kim, J.-H. Ahn, C.-W. Park and H.-S. Ryu, "The short-term cycling properties of Na/PVdF/S battery at ambient temperature," *Journal of Solid State Electrochemistry,* vol. 12, pp. 861-865, 2008.

[107] H. Ryu, T. Kim, K. Kim, J.-H. Ahn, T. Nam, G. Wang and H.-J. Ahn, "Discharge reaction mechanism of room-temperature sodium-sulfur battery with tetra ethylene glycol dimethyl ether liquid electrolyte," *Journal of Power Sources,* vol. 196, no. 11, pp. 5186-5190, 2011.

[108] L. Medenbach, P. Hartmann, J. Janek, T. Stettner, A. Balducci, C. Dirksen, M. Schulz, M. Stelter and P. Adelhelm, "A Sodium Polysulfide Battery with Liquid/Solid Electrolyte: Improving Sulfur Utilization Using P2S5 as Additive and Tetramethylurea as Catholyte Solvent," *Energy Technology,* vol. 8, no. 3, p. 1901200, 2020.

[109] H. Yang, X. Ma, Y. Li, X. Zhou, L. Chen, Z. Zhang, D. Duan, X. Hao and S. Liu, "Electrochemical redox kinetic behavior of S8 and Na2Sn (n = 2, 4, 6, 8) on vulcan XC-72R carbon in a flowing-electrolyte system," *Journal of Power Sources,* vol. 478, p. 229074, 2020.

[110] J. He, A. Bhargav, W. Shin and A. Manthiram, "Stable Dendrite-Free Sodium-Sulfur Batteries Enabled by a Localized High-Concentration Electrolyte," *Journal of the American Chemical Society,* vol. 143, no. 48, pp. 20241-20248, 2021.

[111] H. Liu, W.-H. Lai, Q. Yang, Y. Lei, C. Wu, N. Wang, Y.-X. Wang, S.-L. Chou, H. K. Liu and S. X. Dou, "Understanding Sulfur Redox Mechanisms in Different Electrolytes for Room-Temperature Na-S Batteries," *Nano-Micro Letters,* vol. 13, no. 121, pp. 1-14, 2021.

[112] L. Lutz, D. Alves Dalla Corte, M. Tang, E. Salager, M. Deschamps, A. Grimaud, L. Johnson, P. G. Bruce and J.-M. Tarascon, "Role of Electrolyte Anions in the Na-O2 Battery: Implications for NaO2 Solvation and the Stability of the Sodium Solid Electrolyte Interphase in Glyme Ethers," *Chemistry of Materials,* vol. 29, no. 14, pp. 6066-6075, 2017.

[113] J. Wang, J. Yang, Y. Nuli and R. Holze, "Room temperature Na/S batteries with sulfur composite cathode materials," *Electrochemistry Communications,* vol. 9, no. 1, pp. 31-34, 2007.

[114] I. Bauer, M. Kohl, H. Althues and S. Kaskel, "Shuttle suppression in room temperature sodium-sulfur batteries using ion selective polymer membranes," *Chemistry Communications,* vol. 50, pp. 3208-3210, 2014.

[115] S. Zheng, P. Han, Z. Han, P. Li, H. Zhang and J. Yang, "Nano-Copper-Assisted Immobilization of Sulfur in High-Surface-Area Mesoporous Carbon Cathodes for Room Temperature Na-S Batteries," *Advanced Energy Materials,* vol. 4, no. 12, p. 1400226, 2014.

[116] I. Kim, J.-Y. Park, C. H. Kim, J.-W. Park, J.-P. Ahn, J.-H. Ahn, K.-W. Kim and H.-J. Ahn, "A room temperature Na/S battery using a β" alumina solid electrolyte separator, tetraethylene glycol dimethyl ether electrolyte, and a S/C composite cathode," *Journal of Power Sources,* vol. 301, pp. 332-337, 2016.

[117] B.-W. Zhang, T. Sheng, Y.-X. Wang, S. Chou, K. Davey, S.-X. Dou and S.-Z. Qiao, "Long-Life Room-Temperature Sodium-Sulfur Batteries by Virtue of Transition-Metal-Nanocluster-Sulfur Interactions," *Angewandte Chemie International Edition,* vol. 131, no. 5, pp. 1498-1502, 2019.

PUBLICATION